PhD-FSTC-2018-44
The Faculty of Sciences, Technology and Communication

DISSERTATION

Defence held on 25/05/2018 in Luxembourg

to obtain the degree of

DOCTEUR DE L'UNIVERSITÉ DU LUXEMBOURG

EN PHYSIQUE

by

Denis Mettus
Born on 5 May 1991 in Moscow (Russia)

MAGNETIC SMALL-ANGLE NEUTRON SCATTERING ON BULK METALLIC GLASSES

Dissertation defence committee

Dr. Andreas Michels, dissertation supervisor
Associate Professor, Université du Luxembourg

Dr. Alex Redinger, Chairman
Professor, Université du Luxembourg

Dr. Roland Scantuary, Vice Chairman
Professor, Université du Luxembourg

Dr. Rolf Pelster
Professor, Universität des Saarlandes, Germany

Dr. Sebastian Mühlbauer
Technische Universität München, FRMII, Germany

Abstract

"Someone once stated that “neutrons never lie!”. Trust what they’re telling you."
Boualem Hammouda,
"Probing Nanoscale Structures – The SANS Toolbox"

The present PhD thesis is devoted to the exploration of the use of magnetic small-angle neutron scattering (SANS) technique for analyzing the magnetic microstructure of bulk magnetic materials. The main emphasis is on the three aspects: (i) study of the effect of mechanical deformation on the magnetic microstructure of bulk metallic glasses (BMGs); (ii) theoretical investigation of the predictions of a recent magnetic SANS theory into real space; (iii) study of the impact of the Dzyaloshinski-Moriya (DM) interaction on the magnetic microstructure and magnetic SANS cross section of bulk ferromagnets.

Magnetic-field-dependent SANS has been utilized to study the magnetic microstructure of BMGs. The magnetic scattering from soft magnetic $Fe_{70}Mo_5Ni_5P_{12.5}B_{2.5}C_5$ and hard magnetic $(Nd_{60}Fe_{30}Al_{10})_{92}Ni_8$ alloys in the as-prepared, aged, and mechanically deformed state is compared. While the soft magnetic BMGs exhibit a large field-dependent SANS response with perturbations originating predominantly from spatially varying magnetic anisotropy fields, the SANS cross sections of the hard magnetic BMGs are only weakly dependent on the field, and their angular anisotropy indicates the presence of scattering contributions due to spatially dependent saturation magnetization. Moreover, we observe an unusual increase in the magnetization of the rare-earth-based alloy after deformation. Analysis of the SANS cross sections in terms of the correlation function of the spin misalignment reveals the existence of field-dependent anisotropic long-wavelength magnetization fluctuations on a scale of a few tens of nanometers.

On the basis of the continuum theory of micromagnetics, the correlation function of the spin-misalignment SANS cross section of bulk ferromagnets is computed. The corresponding one- and two-dimensional real-space correlations are analyzed as a function of applied magnetic field, the ratio of magnetic anisotropy field strength to the jump in the saturation magnetization at internal interfaces, the single-particle form factor, and the particle volume fraction. Finally, the theoretical results for the correlation function are compared with experimental data on nanocrystalline cobalt and nickel.

For magnetic materials containing many lattice imperfections, the relativistic DM interaction may result in nonuniform spin textures due to the lack of inversion symmetry at interfaces. Within the framework of the continuum theory of micromagnetics, we explore the impact of the DM interaction on the elastic magnetic SANS cross section. It is shown that the DM interaction gives rise to a polarization-dependent asymmetric term in the spin-flip SANS cross section. To demonstrate the effect, polarized SANS was measured on a nanocrystalline Tb sample and on a cold-rolled polycrystalline Co sample. Both samples show a highly anisotropic difference of half-polarized cross sections, which may indicate the presence of DM interaction in these bulk samples.

Table of contents

List of figures

Chapter 1

Introduction

This PhD thesis explores the use of magnetic small-angle neutron scattering (SANS) technique for analyzing the magnetic microstructure of bulk magnetic materials. The main emphasis is on the following: (i) effect of mechanical deformation on the magnetic microstructure of bulk metallic glasses; (ii) theoretical investigation of the predictions of a recent magnetic SANS theory into real space; (iii) study of the impact of the Dzyaloshinski-Moriya (DM) interaction on the magnetic microstructure and magnetic SANS cross section of bulk ferromagnets.

(i) Bulk metallic glasses (BMG) are amorphous solids that are well known for their excellent mechanical properties which render them attractive for many technological applications, such as consumer electronic industries, sporting goods industries etc. Some BMG can have tensile strength up to 3000 MPa with good corrosion resistance, reasonable toughness, low internal friction and good processability [1–5]. Although these materials are heavily investigated both experimentally and theoretically, yielding and failure of BMG under external strain is still not fully understood. In particular, the discrete nature of the flow defect and/or event in amorphous solids, which enables inelastic deformation [6] before runaway shear bands form leading to catastrophic failure, is still a critical issue.

Recently, Dasgupta, Hentschel, and Procaccia [7, 8] have carried out numerical simulations and analytical theory in order to figure out that upon applying external simple shear localized plastic instabilities occur before the onset of macroscopic yielding. The nature of these plastic events has been identified as isolated Eshelby quadrupoles which organize the nonaffine displacement field around a localized shear transformation. Indeed, the quadrupolar character of the displacement field has been experimentally verified by means of shear-deformation experiments on a monodisperse hard-sphere colloidal glass using confocal microscopy [9].

In order to set the context for the later discussion of the magnetic neutron scattering data of the *amorphous* BMG samples, we refer to the early work of Kronmüller, Seeger, and Wilkens [10, 11] who pioneered the use of the small-angle neutron scattering (SANS) technique for studying spin disorder due to the strain fields of dislocations in *crystalline* materials: in mechanically-deformed metals, the magnetization is highly inhomogeneous in the vicinity of dislocations, which is due to the presence of magnetoelastic coupling. The associated static long-wavelength magnetization fluctuations represent a contrast for elastic magnetic SANS and can be computed by means of the continuum theory of micromagnetics for samples close to magnetic saturation. Most importantly, this type of magnetic SANS — denoted as spin-misalignment scattering — has been predicted to be about $10-100$ times larger than the nuclear SANS which is related to the volume dilatations of dislocations [10]. Although a dislocation is defined with reference to an ordered crystalline lattice, both concepts, dislocations as well as shear transformations in disordered materials, are described using elastic continuum theory. We therefore conjecture that the ideas of Kronmüller, Seeger, and Wilkens can be adapted to the study of displacement fields in magnetic BMG.

The mechanisms by which spin disorder in magnetic materials is generated are essentially related to (i) magnetoelastic and magnetocrystalline anisotropy and to (ii) internal magnetostatic stray fields, for instance, due to spatially fluctuating materials parameters. To be more specific, magnetic forces generated by the distortion of the crystal lattice in the vicinity of a defect tend to modify the local magnetization vector field due to magnetoelastic coupling, while magnetocrystalline anisotropy tries to pull the magnetic moments along the principal axes of the crystal [12]. Likewise, jumps in the values of magnetization, exchange, or anisotropy constants at internal interfaces (*e.g.*, in a magnetic nanocomposite or nanoporous ferromagnet) give rise to inhomogenous magnetization states, which contribute significantly to the magnetic SANS signal. It is also important to emphasize that the adjustment of the magnetization along the respective local "easy" axes does not occur abruptly, *i.e.*, on a scale of the interatomic spacing, but requires a more extended range. This is a consequence of the quantum-mechanical exchange interaction, which spreads out local perturbations in the magnetization over larger distances. The size of such spin inhomogeneities is characterized by a micromagnetic exchange length, which varies continuously with the applied field and takes on values between about $1-100\,\mathrm{nm}$, a size regime which is routinely accessible by the SANS technique.

For the case of magnetic BMG alloys, as are studied in the present thesis, it may be expected that the displacement field couples to the magnetization distribution $\mathbf{M}(\mathbf{r})$ by virtue of the magnetoelastic coupling energy, which links the components of the strain tensor ε_{ij} to $\mathbf{M}$; in other words, the spins might decorate the spatial distribution of the displacement field. Since the spatial extent of these displacement fields (quadrupolar structures) is of the order of a few 10 nm, the SANS technique is ideally suited to visualize the associated spin structures in the bulk of the material; in fact, we are not aware of any other method which may accomplish this. Moreover, the application of an external magnetic field allows one to tune the size of the spin-misaligned regions, since the characteristic wavelength of the spin-misalignment fluctuations is expected to decrease with increasing field [13].

In the present work we discuss the influence of mechanical deformation on the magnetic microstructure of a soft and hard magnetic BMG by means of magnetic-field-dependent small-angle neutron scattering (SANS). The choice of these materials enables one to explore — in the spirit of a feasibility study — the limiting cases of weak and strong magnetic anisotropy and, hence, different degrees of magnetoelastic coupling of displacement to magnetization. We present and compare the results of unpolarized SANS measurements, and analyze their SANS cross sections in real space by computing the correlation function of the spin misalignment. Finally, we discuss how the expected scattering signal of displacement fields can be separated from other scattering contributions.

(ii) Small-angle neutron scattering (SANS) is a very popular method for investigating nanoscale structural and magnetic inhomogeneities in the bulk of materials. In most situations, SANS data are analyzed in reciprocal space, by fitting a particular model to the experimental SANS cross section. An alternative real-space approach to analyzing SANS data is the computation of the (auto)correlation function of the system, for instance by means of the indirect Fourier-transformation technique [14–17], which has recently been extended to allow for the analysis of two-dimensional small-angle scattering patterns of oriented samples [18, 19]. For dilute, monodisperse, and uniform particle-matrix systems, several analytical expressions for the density-density autocorrelation function $\gamma(r)$ or, likewise, for the distance distribution function $p(r) = r^2\gamma(r)$ have been derived (see, *e.g.* [20]); this is a well established procedure in small-angle x-ray scattering and in nuclear SANS, *e.g.* in the analysis of polymers [21] or in the study of the formation of magnetic nanocrystals in glass ceramics [22].

In the context of real-space analysis of scattering data, it is also worth to mention the recent progress made in the computation of the magnetic pair distribution function [23], which is obtained via Fourier transformation of the magnetic neutron scattering cross section. This approach permits the analysis of long and short-range magnetic correlations of a wide range of magnetic structures such as spin-density waves, spin-ice compounds, or molecular magnets.

Honecker and Michels have recently provided a theory of magnetic SANS of polycrystalline bulk ferromagnets [24], which was successfully employed in order to analyze the magnetic microstructure of iron-based two-phase nanocomposites [25]. In addition to nanocomposites, the theory is also applicable to the study of elemental ferromagnets, nanoporous magnets, or ferromagnetic steels; it provides information on the exchange-stiffness constant, as well as on the strength and spatial structure of the magnetic anisotropy and magnetostatic field.

Magnetic SANS of statistically-isotropic bulk ferromagnets is — in contrast to nuclear SANS on such structures — highly anisotropic, *i.e.* the magnetic SANS cross section depends not only on the magnitude but also on the orientation of the momentum-transfer vector. The results for the Fourier coefficients of the magnetization [24] demonstrate the unmistakable impact of the magnetodipolar interaction on magnetic SANS; magnetostatics is essential for understanding the complex magnetic-field-dependent angular anisotropies which may be observed on a two-dimensional position-sensitive detector; these anisotropies go beyond the well-known '$\sin^2\theta$' anisotropy of magnetic SANS. Furthermore, the classical particle-matrix concept of small-angle scattering is not adapted to the complex magnetic textures which may form inside the bulk of magnetic media (see discussion in the introduction of [13]); for such materials, the continuum theory of micromagnetics [26] provides the proper theoretical framework for computing the magnetic SANS cross section. The second focus of this thesis is to provide a discussion of the predictions of the micromagnetic SANS theory into real space by calculating the correlation function of the spin-misalignment SANS cross section.

(iii) The Dzyaloshinski-Moriya (DM) interaction [27, 28] has recently become anew the focus of an intense worldwide research effort in condensed-matter physics. This interaction is due to relativistic spin-orbit coupling, and in low-symmetry crystal structures lacking inversion symmetry it gives rise to antisymmetric magnetic interactions. Particularly well investigated classes of materials are ultrathin film nanostructures and noncentrosymmetric B20 transition-metal compounds (*e.g.*, MnSi, $\mathrm{Fe_{1-x}Co_xSi}$, or FeGe), where the DM interaction plays an important role for the formation of various kinds of inhomogeneous spin structures such as long-wavelength spirals, vortex states, and skyrmion textures (see, *e.g.*, Refs. [29–46] and references therein).

However, already in 1963, Arrott [47] pointed out that even in a high-symmetry lattice, where the antisymmetric DM term would normally vanish, this interaction is present in the vicinity of any lattice defect. Arrott argued that in antiferromagnetic crystals the DM interaction results in parasitic ferromagnetism, whereas in ferromagnets it gives rise to local antiferromagnetism (in this way reducing the spontaneous magnetization). Hence, based on these considerations, one may expect that the DM interaction substantially influences the magnetic microstructure of polycrystalline materials with a large defect density. In a sense, microstructural defects act as a source of additional local chiral interactions, similar to the above mentioned (intrinsic) DM interactions in noncentrosymmetric crystals.

One class of materials, where defects play a decisive role, are nanocrystalline magnets, which are characterized by an extremely large interface-to-volume ratio; note that the volume fraction of internal interfaces (*e.g.*, grain boundaries) scales as L^{-1}, where $L \sim 10-20\,\mathrm{nm}$ represents the average crystallite size. This implies that a significant amount of atoms ($\sim 10-20\,\mathrm{vol.\%}$) in such magnets are localized in the near-vicinity of interfaces, where inversion symmetry is likely to be broken. Consequently, the magnetic properties of a polycrystalline magnet may be substantially influenced by the DM term once its average grain size “goes nano”.

Thus, the DM interaction might reveal itself in magnets with many crystalline imperfections. Regarding the question of how to measure an ensuing “effect”: traditionally, the influence of lattice defects on the magnetization of bulk magnetic materials is studied by analyzing the high-field branch of a hysteresis curve (see, *e.g.*, the classic studies by Brown and Kronmüller [26, 48, 49]). However, this approach suffers from the disadvantages that it provides only integral (and no spatially-resolved) information and that the result of such an analysis may depend on the range of applied-field values over which the magnetization data are analyzed. As we will see below, neutron scattering and, in particular, polarized small-angle neutron scattering (SANS) [50–56] provides an important means to investigate the relevance of the defect-induced DM interaction on a microscopic scale and inside the bulk of inhomogeneous magnets. The third focus of this thesis is the study of the impact of the DM interaction on the elastic magnetic SANS cross section of lattice-defect-rich bulk ferromagnets (nanocrystalline Terbium and cold-rolled Cobalt).

The thesis is structured as follows: in Chapter 2 we provide an overview over the theoretical background of the problem and the theoretical results obtained during the present PhD thesis. This includes the micromagnetic theory, the description of the small-angle neutron scattering (SANS) cross section, the concept of the correlation function analysis of magnetic SANS, and the theoretical predictions of the influence of the Dzyaloshinsky-Moriya interaction on the magnetic spin-misalignment SANS. Chapter 3 describes the samples and the experimental techniques used, such as SANS, vibrating sample magnetometry (VSM), and X-ray diffraction (XRD). Chapter 4 presents and discusses the experimental results. Chapter 5 summarizes the main results of this thesis and provides an outlook to future studies.

Chapter 2

Theory

Chapter 2 is organized as follows. Section 2.1 introduces the model for the magnetic microstructure of bulk ferromagnets which underlies magnetic SANS theory used or developed during this PhD thesis work. Section 2.2 summarizes the main expressions for the unpolarized magnetic SANS cross section. Section 2.3 describes the correlation function analysis which helps to interpret the scattering data relating it to real-size objects, and presents the results of the theoretical investigation of correlation function behavior. Section 2.4 presents the study of the impact of the Dzyaloshinski-Moriya interaction on the magnetic microstructure and magnetic SANS cross section of bulk ferromagnets.

Note that the results presented in the Sections 2.3 and 2.4 are the part of the actual PhD work.

2.1 Micromagnetic theory

Micromagnetics is a phenomenological continuum theory which has been developed in order to describe the magnetization vector field $\mathbf{M}(\mathbf{r})$ of an arbitrarily-shaped ferromagnetic body when the applied magnetic field, the geometry of the ferromagnet, and the magnetic materials parameters are known [57, 48, 49, 58]. The characteristic length scale to which micromagnetic calculations apply varies between a few nanometers and a few hundred nanometers (implying the absence of discrete atomic and corresponding magnetic structure), which means that the micromagnetic computations are within the resolution of SANS, and therefore are well-adapted to the problem. Pioneering work in this direction was performed by Kronmüller et al [10] who calculated the magnetic SANS due to spin disorder related to the strain fields of dislocations.

In the present work, we are interested in the elastic spin-misalignment scattering, which results from the static magnetic microstructure of a bulk ferromagnet. Spin-misalignment scattering is of relevance whenever the magnitude of the externally applied magnetic field is insufficient to completely saturate the sample. The magnetic materials usually considered in this topic are characterized by a large number of microstructural defects (*e.g.* pores, grain or phase boundaries, dislocations, point defects). Examples for such materials are amorphous metallic alloys, polycrystalline elemental magnets with a nanometer crystallite size, heavily deformed (cold worked) metals, nanoporous ferromagnets, or multiphase magnetic nanocomposites, including magnetic steels.

A typical scheme of such material is presented on the Fig. 2.1. Figure 2.1(a) represents a sketch of an idealized two-dimensional nuclear microstructure; note that the system is not obliged to have a long-range crystalline order and the grain size may vary. The red arrows represent the crystallographic set of easy axes for the magnetization, which changes randomly at each internal interface (*e.g.*a grain boundary); for simplicity, it is assumed to be a uniaxial magnetic anisotropy. The hexagons' colors (blue and white) represents the spatial variation of the magnetic material's parameters (exchange constant A, anisotropy constant K and saturation magnetization M_s). In such concept, there are the two main sources causing a perturbation of the magnetic microstructure, which is identified by [24] as (i) spatial random variations in the direction and/or magnitude of the magnetic anisotropy field and (ii) spatial variations in the magnitude of the saturation magnetization. The characteristic length scales over which such variations occur may be related, for example, to the average particle or crystallite size, which for bulk nanomagnets typically is of the order of $10-50$ nm. Figure 2.1(b) shows a superposed magnetic microstructure in the presence of a strong applied magnetic field $\mathbf{H}_0$. The shown coarse-grained distribution of spins is only qualitative but suggests the existence of continuously varying nanoscale magnetization profiles, which give rise to a strongly field-dependent magnetic SANS cross section. Note also the absence of sharp interfaces in the magnetic microstructure in Fig. 2.1(b), in contrast to the grain microstructure presented in Fig. 2.1(a).

It was shown in [13], that spin-misalignment scattering, which is of main interest in the present work, typically dominates the magnetic SANS signal from bulk ferromagnets. The mechanisms by which spin disorder is generated are essentially related to (a) magnetoelastic and magnetocrystalline anisotropy and (b) internal magnetostatic stray fields, for instance, due to spatially fluctuating materials' parameters. To be more specific, forces due to the distortion of the lattice (in the vicinity of a defect) tend to rotate the local magnetization vector field $\mathbf{M}(\mathbf{r})$ along the main axes of the system of internal stresses (magnetoelastic coupling), while magnetocrystalline anisotropy tries to pull the magnetic moments along the principal axes of the crystal. Likewise, jumps in the values of magnetization, exchange, or anisotropy constants at internal interfaces (*e.g.*in a magnetic nanocomposite or nanoporous ferromagnet) give

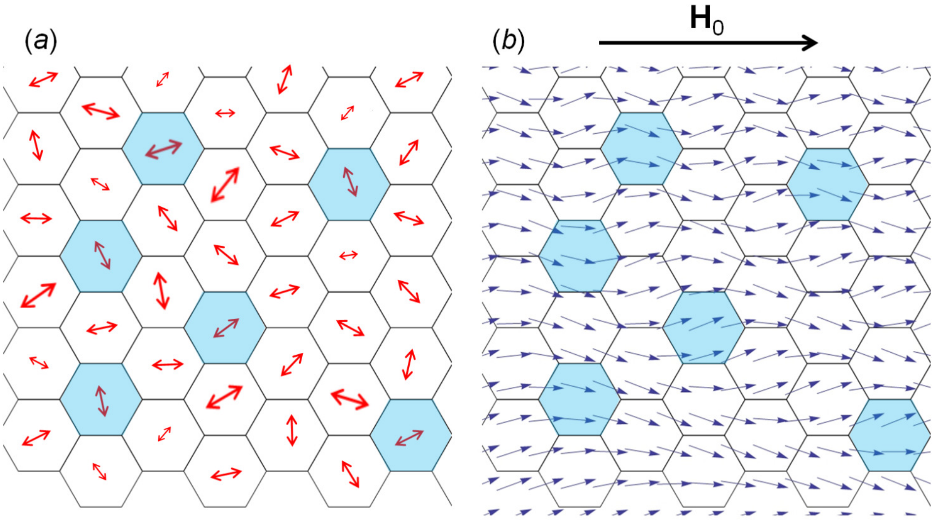

Fig. 2.1 Model for the magnetic microstructure of a bulk ferromagnet. (a) Sketch of an idealized two-dimensional (nuclear) grain microstructure. The red arrows represent spatial variation of the direction and/or magnitude of the magnetic anisotropy field; for simplicity, it is assumed to be a uniaxial magnetic anisotropy. The hexagons' colors represent the spatial variation of the magnetic material's parameters. (b) Superposed magnetic microstructure in the presence of an applied magnetic field $\mathbf{H}_0$.

rise to inhomogenous magnetization states, which contribute significantly to the magnetic SANS signal. Note that the adjustment of the magnetization along the respective local 'easy' axes does not occur abruptly, *i.e.*on a scale of the interatomic spacing, but requires a more extended range. This is a consequence of the quantum-mechanical exchange interaction, which spreads out local perturbations in $\mathbf{M}(\mathbf{r})$ over larger distances [59].

2.1.1 Magnetic energy contributions

The main problem in the micromagnetic theory is finding the equilibrium magnetization state of the system. In the concept of micromagnetics the total magnetic energy of a bulk ferromagnet can be expressed as

$$E_{\mathrm{tot}} = E_{\mathrm{z}} + E_{\mathrm{ex}} + E_{\mathrm{mc}} + E_{\mathrm{me}} + E_{\mathrm{m}}, \tag{2.1}$$

which consists of a number of energy contributions: the energy E_{z} due to interaction with an external field, the energy E_{ex} due to the exchange interaction, the magnetocrystalline energy E_{mc} and magnetoelastic energy E_{me} due to the magnetic anisotropy, and the magnetostatic energy E_{m}.

The energy term due to interaction with an external field is also called Zeeman's energy. The magnetic field $\mathbf{H}_0$ imposes a torque on the magnetization and tries to rotate the magnetic moments along its direction. The energy term is given by

$$E_\mathrm{z} = -\mu_0 \int_V \mathbf{M} \cdot \mathbf{H}_0 \, \mathrm{d}V, \tag{2.2}$$

where $\mu_0 = 4\pi \cdot 10^{-7}\,\mathrm{T\,m\,A^{-1}}$ is the permeability of free space.

The exchange energy is a positive definite quantity, which favors the parallel alignment of neighboring atomic magnetic moments in the crystal lattice; in other words, any nonuniformity in $\mathbf{M}$ has an energy cost. The energy of exchange interaction (for cubic crystal structures) can be approximated [60, 61] as

$$E_\mathrm{ex} = \int_V A \left((\nabla m_x)^2 + (\nabla m_y)^2 + (\nabla m_z)^2 \right) \, \mathrm{d}V, \tag{2.3}$$

where A denotes the exchange-stiffness constant, $\mathbf{m}$ is a magnetization unit vector $\mathbf{m} = \mathbf{M}/M_s$ in the direction of the magnetization, and the integral extends over the sample volume V. Typical values for A are of the order of 10 $\mathrm{pJm^{-1}}$ [49, 62]. Note that in multiphase magnets, the exchange constant is a function of the position inside the material, *i.e.* $A = A(\mathbf{r})$ [63–65]. Equation (2.3) represents a continuum expansion based on the discrete Heisenberg Hamiltonian $\mathscr{H}_\mathrm{ex} = -\sum_{i,j} J_{ij}(\mathbf{r}_{ij})\mathbf{S}_i(\mathbf{r}_i)\mathbf{S}_j(\mathbf{r}_j)$, by treating the localized magnetic moments with spins S_i as (quasi-)classical continuous vectors, taking into account only nearest neighbor exchange interactions (of equal the quantum mechanical exchange integral J), and by assuming small angles between neighboring spins (see [66] for a full derivation).

The magnetocrystalline anisotropy energy E_mc expresses the dependence of the magnetic energy of a ferromagnet on the orientation of the magnetization $\mathbf{M}$ relative to the crystal axes. The origin of magnetocrystalline anisotropy is related to the combined action of the spin-orbit (L-S) coupling and the crystal-field interaction. The magnetodipolar interaction may also contribute to E_mc [67, 68]; however, dipolar anisotropy is generally small and vanishes for ideal cubic and hexagonal lattices [66]. On a phenomenological level, E_mc is determined by an expression for the anisotropy energy density ω_{mc}, which is a function of the position $\mathbf{r}$ and of $\mathbf{M}$ [26],

$$E_\mathrm{mc} = \int_V \omega_\mathrm{mc} \left(\mathbf{r}, \mathbf{M}(\mathbf{r}) \right) \, \mathrm{d}V. \tag{2.4}$$

The magnetocrystalline anisotropy energy favors the orientation of $\mathbf{M}$ along certain crystallographic directions, the so-called easy axes. Expressions for E_mc reflect therefore the symmetry of the underlying crystal lattice. In particular, E_mc must be an even function of $\mathbf{M}$. Experimental values for the anisotropy constants range between about $10^2\,\mathrm{Jm^{-3}}$ (for soft magnetic materials) and $10^7\,\mathrm{Jm}^{-3}$ (for hard magnets) [49, 62, 69]. Note the E_{mc} is still present even for the materials that lack a long-range crystalline order like bulk metallic glass.

The magnetoelastic energy term is due to the magnetostriction effect [70]: when an unstressed specimen is magnetized by an applied magnetic field, the dimensions of the body change. The process continues until elastic counterforces provide for a state of stable equilibrium. The phenomenological expression for E_{me} reads:

$$E_{\mathrm{me}} = \int_V \omega_{\mathrm{me}}\, \mathrm{d}V, \tag{2.5}$$

where ω_{me} is the magnetoelastic energy density. The general treatment of magnetostrictive effects in deformable magnets is a highly complicated task [49]. With respect to the micromagnetic SANS theory (see Section 2.2 below), we note that we do not employ any of the equations for the magnetocrystalline and/or magnetoelastic energy density. Rather, the linearized micromagnetic equations are solved by using an approximate formal expression for ω, which includes a combination of both magnetocrystalline and magnetoelastic anisotropy. The analysis of experimental magnetic-field-dependent SANS data allows one to determine the Fourier coefficients of the magnetic anisotropy field which are related to that particular ω.

The magnetostatic energy is due to magnetodipolar interaction. Within the Lorentz continuum approximation, the magnetostatic field $\mathbf{H}_{\mathrm{d}}(\mathbf{r})$ that is created by the magnetization $\mathbf{M}$ is related to a magnetostatic self-energy [48]:

$$E_{\mathrm{m}} = -\frac{1}{2}\mu_0 \int_V \mathbf{M}\cdot\mathbf{H}_d\, \mathrm{d}V = \frac{1}{2}\mu_0 \int_{\text{all space}} |\mathbf{H}_d|^2\, \mathrm{d}V. \tag{2.6}$$

There, the demagnetizing field $\mathbf{H}_d$ may be derived from basic magnetostatics (*i.e.* the solution of the Poisson equation), which allows one to compute $\mathbf{H}_d$ from the scalar potential function $U(\mathbf{r})$:

$$\mathbf{H}_d(\mathbf{r}) = -\nabla U(\mathbf{r}) = \frac{1}{4\pi}\left(-\int_V \frac{(\mathbf{r}-\mathbf{r}')\,\nabla_{\mathbf{r}'}\cdot\mathbf{M}(\mathbf{r}')}{|\mathbf{r}-\mathbf{r}'|^3}\,\mathrm{d}V' + \int_S \frac{(\mathbf{r}-\mathbf{r}')\,\mathbf{n}\cdot\mathbf{M}(\mathbf{r}')}{|\mathbf{r}-\mathbf{r}'|^3}\,dS'\right). \tag{2.7}$$

The first integral in Eq. (2.7) is taken over the sample volume V and the second integral over the sample surface S of the ferromagnetic body. The magnetostatic self-energy $E_{\mathrm{m}} \geqslant 0$ tries to avoid any sort of abstract magnetic volume $(-\nabla\cdot\mathbf{M})$ or surface $(\mathbf{n}\cdot\mathbf{M})$ charges. The sources of $\mathbf{H}_d$ are due to inhomogeneities in $\mathbf{M}$, either in orientation or in magnitude.

2.1.2 Balance of torques equation

As it was mentioned above, the energy of a ferromagnet should be considered as a functional of its magnetization: $E_{\mathrm{tot}} = E_{\mathrm{tot}}\left(\mathbf{M}(\mathbf{r})\right)$. The state of equilibrium magnetization configuration corresponds to a (local) energy minimum. Therefore, at static equilibrium, the variation of E_{tot} must vanish, *i.e.*

$$\delta E_{\mathrm{tot}} = \delta(E_{\mathrm{z}} + E_{\mathrm{ex}} + E_{\mathrm{mc}} + E_{\mathrm{me}} + E_{\mathrm{m}}) = 0. \tag{2.8}$$

As detailed in [26, 71, 49, 72], variational calculus leads to a set of nonlinear partial integro-differential equations for the bulk, along with quite complex boundary conditions for the magnetization at the surface. In keeping with our interest in the magnetic microstructure within the bulk of macroscopic magnetic bodies, we restrict our attention here to the bulk equilibrium conditions. The static equations of micromagnetics (so-called Brown's equations) can be conveniently expressed as a balance-of-torques equation, which can be written as [26, 48, 49]:

$$\mathbf{M}(\mathbf{r}) \times \mathbf{H}_{\mathrm{eff}}(\mathbf{r}) = 0. \tag{2.9}$$

Equations (2.9) express the fact that at static equilibrium the torque on the magnetization $\mathbf{M}(\mathbf{r})$ due to an effective magnetic field $\mathbf{H}_{\mathrm{eff}}(\mathbf{r})$ vanishes everywhere inside the material. The effective field is defined as the functional derivative of the ferromagnetic total energy-density functional ω (with relation to energy: $E = \int\limits_V \omega \, \mathrm{d}V$) with respect to the magnetization:

$$\mathbf{H}_{\mathrm{eff}} = -\frac{1}{\mu_0} \cdot \frac{\delta \omega}{\delta \mathbf{M}} = \mathbf{H}_0 + \mathbf{H}_{\mathrm{ex}} + \mathbf{H}_p + \mathbf{H}_d, \tag{2.10}$$

with a uniform applied magnetic field $\mathbf{H}_0$ (corresponds to the E_{z}), the exchange field $\mathbf{H}_{\mathrm{ex}}$ (corresponds to E_{ex}), the magnetic anisotropy field $\mathbf{H}_p(\mathbf{r})$ (corresponds to E_{mc} and E_{me}), and the magnetostatic field $\mathbf{H}_d(\mathbf{r})$ (corresponds to E_{m}).

In the following derivations, it is assumed that the material is nearly saturated by a strong applied magnetic field $\mathbf{H}_0 \parallel \mathbf{e}_z$, and we express the magnetization as

$$\mathbf{M}(\mathbf{r}) = \left\{ M_x(\mathbf{r}) \ll M_s,\ M_y(\mathbf{r}) \ll M_s,\ M_z(\mathbf{r}) \approx M_s(\mathbf{r}) \right\}. \tag{2.11}$$

The local saturation magnetization is assumed to be a function of the position $\mathbf{r}$ inside the material [73, 74]:

$$M_s(\mathbf{r}) = M_s\left(1 + I_m(\mathbf{r})\right), \tag{2.12}$$

where I_m is an inhomogeneity function, which is small in magnitude and describes the local variation of M_s. The spatial average of I_m vanishes, $\langle I_m(\mathbf{r})\rangle = 0$, so that $\langle M_s(\mathbf{r})\rangle = M_s$ is the saturation magnetization (which can be measured with a magnetometer). Note that due to the constraint $|\mathbf{M}| = M_s$, there are only two independent components of $\mathbf{M}$. By defining the Fourier transform $\widetilde{F}(\mathbf{q})$ of a continuous function $F(\mathbf{r})$ as

$$\widetilde{F}(\mathbf{q}) = \frac{1}{(2\pi)^{3/2}} \int_V F(\mathbf{r}) \exp(-i\mathbf{q}\mathbf{r})\, \mathrm{d}V, \tag{2.13}$$

where $i^2 = -1$ and $\mathbf{q}$ is the wavevector, one can write for the magnetization Fourier coefficient $\widetilde{\mathbf{M}}(\mathbf{q})$ up to the first order in $\widetilde{I}_m$

$$\widetilde{\mathbf{M}}(\mathbf{q}) = \left\{\widetilde{M}_x(\mathbf{q}),\, \widetilde{M}_y(\mathbf{q}),\, M_s(\delta(\mathbf{q}) + \widetilde{I}_m(\mathbf{q}))\right\}, \tag{2.14}$$

where $\delta(\mathbf{q})$ is the Dirac's Delta function.

As it was written above, the solution of Eq. (2.8) with respect to $\mathbf{M}(\mathbf{r})$ provides the functional expressions for the components of $\mathbf{H}_{\mathrm{eff}}$ (compare Eq. (2.10)). The exchange field (see Eq.(2.3)) is given by [61]

$$\mathbf{H}_{\mathrm{ex}} = \frac{2A}{\mu_0 {M_s}^2}\, \nabla^2\mathbf{M} = l_M^2\, \nabla^2\mathbf{M}, \tag{2.15}$$

with l_M being a micromagnetic length scale of magnetostatic interaction, and the vector Laplace operator of a vector field $\mathbf{f}$ given by $\nabla^2\mathbf{f} = \left\{\nabla^2 f_x,\, \nabla^2 f_y,\, \nabla^2 f_z\right\}$. In the present work, the values for the exchange-stiffness constant A and for the DM interaction constant D are assumed to be uniform throughout the material (in contrast to the local saturation magnetization). The corresponding Fourier transform reads

$$\widetilde{\mathbf{H}}_{\mathrm{ex}}(\mathbf{q}) = -l_M^2 q^2 \left\{\widetilde{M}_x,\, \widetilde{M}_y,\, M_s\widetilde{I}_m\right\}. \tag{2.16}$$

The remaining fields in the balance-of-torques Eq. (2.9) have also convenient analytical representations in terms of their Fourier transforms. The magnetostatic field $\mathbf{H}_d(\mathbf{r})$ can be written as the sum of the demagnetizing field $\mathbf{H}_d^s(\mathbf{r})$ due to surface charges and of the magnetostatic field $\mathbf{H}_d^b(\mathbf{r})$ which is related to volume charges (compare to the sum of two integrals over the sample volume and over the sample surface in Eq. (2.7)), *i.e.*, $\mathbf{H}_d(\mathbf{r}) = \mathbf{H}_d^s(\mathbf{r}) + \mathbf{H}_d^b(\mathbf{r})$. In the high-field limit (when the magnetization is close to saturation) and for samples with an ellipsoidal shape with $\mathbf{H}_0$ directed along a principal axis of the ellipsoid, one may approximate the demagnetizing field due to the surface charges by the *uniform* field $\mathbf{H}_d^s = -N_d M_s \mathbf{e}_z$, where $0 < N_d < 1$ denotes the corresponding demagnetizing factor. The field $H_d^s = -N_d M_s$ can then be combined with the applied magnetic field $\mathbf{H}_0$ to yield the internal magnetic field $H_i = H_0 - N_d M_s$ (*i.e.*, the $\mathbf{q} = 0$ Fourier component of $\mathbf{H}_d(\mathbf{r})$) [48]. At $\mathbf{q} \neq 0$, the Fourier component $\widetilde{\mathbf{H}}_d^b(\mathbf{q})$ of $\mathbf{H}_d^b(\mathbf{r})$ is found from basic magnetostatics ($\nabla \cdot \mathbf{B} = 0$; $\nabla \times \mathbf{H}_d = 0$)[61] :

$$\widetilde{\mathbf{H}}_d^b(\mathbf{q}) = -\frac{\mathbf{q} \cdot (\mathbf{q} \cdot \widetilde{\mathbf{M}}(\mathbf{q}))}{q^2}, \tag{2.17}$$

so that the total $\widetilde{\mathbf{H}}_d(\mathbf{q})$ is

$$\widetilde{\mathbf{H}}_d(\mathbf{q}) = H_i \delta(\mathbf{q})\, \mathbf{e}_z - \frac{\mathbf{q} \cdot (\mathbf{q} \cdot \widetilde{\mathbf{M}}(\mathbf{q}))}{q^2}. \tag{2.18}$$

Up to the first order in I_m, the z-component of the magnetic anisotropy field $\mathbf{H}_p(\mathbf{r})$ does not produce a torque on the magnetization vector[74], so that we will omit it here and represent the Fourier transform of $\mathbf{H}_p(\mathbf{r})$ as

$$\widetilde{\mathbf{H}}_p(\mathbf{q}) = \left\{ \widetilde{H}_{p,x}(\mathbf{q}), \widetilde{H}_{p,y}(\mathbf{q}), 0 \right\}. \tag{2.19}$$

This term is a source of spin disorder since it increases the magnitude of the transversal Fourier components (see below). The field $\mathbf{H}_p(\mathbf{r})$ contains the information about the sample's microstructure (*e.g.*, crystallite size, inhomogeneous lattice strain, crystallographic texture) [75]. Note that no assumption is made about the particular form of the magnetic anisotropy (magnetocrystalline and/or magnetoelastic). We also remind the reader that due to the condition $|\mathbf{M}| = M_s$, there are only two independent components of $\mathbf{H}_p(\mathbf{r})$. In case of a weak spatial dependency of A (with fluctuations of the order of the saturation-magnetization fluctuation $I_m(\mathbf{r})$), the quantity l_M must be understood as spatial averages of the corresponding expressions. In this situation, the first-order expansion of the Brown's equations (2.9) is still valid and contains no additional terms [74].

By using Eqs. (2.16, 2.18, 2.19) in the balance of torque equation and by neglecting terms of higher than linear order in $\widetilde{M}_x$, $\widetilde{M}_y$, and $\widetilde{I}_m$ (including terms such as $\widetilde{M}_x \widetilde{I}_m$ and $\widetilde{H}_{p,x} \widetilde{I}_m$), we obtain, in Fourier space, and for a general orientation of the wavevector $\mathbf{q} = \left\{ q_x, q_y, q_z \right\}$, the following set of linear equations for $\widetilde{M}_x$ and $\widetilde{M}_y$ [48]:

$$\widetilde{M}_x \left(1 + p \frac{q_x^2}{q^2} \right) + \widetilde{M}_y \left(p \frac{q_x q_y}{q^2} \right) = p \left(\widetilde{H}_{p,x} - M_s \widetilde{I}_m \frac{q_x q_z}{q^2} \right), \tag{2.20}$$

$$\widetilde{M}_y \left(1 + p \frac{q_y^2}{q^2} \right) + \widetilde{M}_x \left(p \frac{q_x q_y}{q^2} \right) = p \left(\widetilde{H}_{p,y} - M_s \widetilde{I}_m \frac{q_y q_z}{q^2} \right). \tag{2.21}$$

The dimensionless function

$$p(q,H_i) = \frac{M_s}{H_{\mathrm{eff}}(q,H_i)} \tag{2.22}$$

depends on the effective magnetic field (should not be confused with the one in Eq. (2.9))

$$H_{\mathrm{eff}} = \left(1 + l_H^2 q^2\right) H_i, \tag{2.23}$$

and

$$l_H(H_i) = \sqrt{\frac{2A}{\mu_0 M_s H_i}} \tag{2.24}$$

denotes the micromagnetic exchange length of the field, which is a measure for the size of inhomogeneously magnetized regions around microstructural lattice defects.

The present approach is of the first order in the amplitude of the inhomogeneity function $\widetilde{I}_m$, which entails the neglect of complicated convolution products. We refer to Ref. [74] for a micromagnetic SANS theory which is up to the second order in $\widetilde{I}_m$.

The solutions of Eqs. (2.20) and (2.21) are:

$$\widetilde{M}_x = \frac{p\left(\widetilde{H}_{p,x}\left[1 + p\frac{q_y^2}{q^2}\right] - M_s \widetilde{I}_m \frac{q_x q_z}{q^2} - \widetilde{H}_{p,y} p \frac{q_x q_y}{q^2}\right)}{1 + p\frac{q_x^2 + q_y^2}{q^2}}, \tag{2.25}$$

$$\widetilde{M}_y = \frac{p\left(\widetilde{H}_{p,y}\left[1 + p\frac{q_x^2}{q^2}\right] - M_s \widetilde{I}_m \frac{q_y q_z}{q^2} - \widetilde{H}_{p,x} p \frac{q_x q_y}{q^2}\right)}{1 + p\frac{q_x^2 + q_y^2}{q^2}}, \tag{2.26}$$

Besides computing the magnetic SANS cross section (see the Section 2.2), the above results for the transversal Fourier components given by Eqs. (2.25) and (2.26)) can also be used for obtaining the autocorrelation function of the spin-misalignment [76] and the approach-to-saturation law.

2.2 SANS cross sections and theory

The present Section is devoted to the theoretical description of small-angle neutron scattering (SANS) cross section. The SANS cross section, which is measured during a neutron scattering experiment, describes how well neutrons scatter depending on their initial and final energy, on the direction of scattered neutrons, and on the internal sample structure. Thus, study of the experimental scattering cross section may provide information on the sample nuclear and magnetic microstructure.

The section is organized as follows. First, we discuss basic neutron properties and why it is used as a probe in Section 2.2.1. Then we discuss the basics of the neutron scattering in non-magnetic approach and show the general derivation of an elastic coherent nuclear scattering cross section in Section 2.2.2. After that, we introduce the magnetic SANS cross section in 2.2.3 and discuss its properties based on the micromagnetic theory in Section 2.2.4.

2.2.1 Basic neutron properties

Neutrons were discovered by Chadwick in 1932 [77], who was rewarded for the discovery by the Nobel Prize in Physics in 1935. A neutron has zero charge, which means it does not interact with Coulomb potential, thus its interactions with matter are confined to the short-range nuclear and magnetic interactions. This allows neutrons to be able to penentrate deeply into the matter, in contrast to electrons or protons, and makes them a unique probe for investigating bulk condensed matter. For example, the resolution of Lorentz microscopy generally ranges from $5-50\,\mathrm{nm}$ for transmitted electrons to $15\,\mu\mathrm{m}$ for back-scattered electrons [70], while neutrons are able to penetrate mm-thick samples. Additionally, neutrons have magnetic moment, that added to their depth penetration convert them as the ideal candidate for the study of internal magnetic structures of bulk condensed matter. Additionally neutrons are in most cases non-destructive technique (specially for inorganic samples), which makes them very useful for studying the organic and living matter.

Table 2.1 Basic neutron properties and useful relations.

Mass:	$\mathrm{m} = 1.675 \cdot 10^{-27}\,\mathrm{kg}$
Charge:	0
Magnetic dipole moment:	$\mu_n = 1.0419 \cdot 10^{-3}\,\mu_B = -1.913\,\mu_N$
Life time:	$t_{1/2} = 820\,s$
Spin:	1/2
Wavelength to velocity relation:	$\lambda(\text{Å}) = \frac{h}{mv} = \frac{3956}{v(m/s)}$

In the present work, we consider the case of the so-called cold neutrons. Cold neutrons are characterized by the energy of $0.1-10\,\mathrm{meV}$, which corresponds to a wavelength of several angstroms. The typical wavelength of the neutrons used in the presented experiments is $\sim 6\,\mathrm{\AA}$. Such wavelength is above Bragg cut-off, thus the scattering from the discrete nuclear or magnetic structure (which is typically of the size of few Å) is avoided. Using such neutrons in a SANS experiment provides the spatial resolution of the instrument of $\sim$ 3-300 nm.

2.2.2 SANS basics and short description of Nuclear SANS

The principal schematic of a scattering experiment is depicted in Fig. 2.2. We consider a beam of cold neutrons with a momentum-vector $\mathbf{k}_0$, all with the initial energy E, incident on a target. The target (or, in other words, the sample) is a general system of atoms with known elemental composition. A neutron from the incident beam is scattered inside the sample, with a resulting scattering direction defined by the angles 2ψ and ϕ. The resulting measure recorded during a scattering experiment is a distribution of the amount of the scattered neutrons in the solid angle $\mathrm{d}\Omega$ over different scattering directions divided by time. This value is called a scattering intensity $I=\varepsilon\sigma V_s\Phi$, where ε represents instrument "efficiency", σ is the so-called scattering cross section, V_s is the sample volume, and Φ is the incident neutron flux (*i.e.* the number of neutrons flying through the unit area per second, with the area being perpendicular to the direction of the neutron beam). While ε and Φ are parameters rather related to the experimental setup, it is the σ what carries the information about the sample's internal structure.

The partial differential cross section $\frac{\mathrm{d}^2\sigma}{\mathrm{d}\Omega\mathrm{d}E'}$ is a number of neutrons scattered per second $n'(2\psi,\varphi)$ into a solid angle $\mathrm{d}\Omega$ in the direction defined by angles 2ψ and φ, with final energy between E' and $E'+\mathrm{d}E'$, divided by incident neutron flux Φ. The relationship between σ and $\frac{\mathrm{d}^2\sigma}{\mathrm{d}\Omega\mathrm{d}E'}$ is a double integration over both $\mathrm{d}\Omega$ and $\mathrm{d}E'$ [78]:

$$\frac{\mathrm{d}^2\sigma}{\mathrm{d}\Omega\mathrm{d}E'}=\frac{n'(2\psi,\varphi)}{\Phi\mathrm{d}\Omega\mathrm{d}E'}. \tag{2.27}$$

In the case when the scattered neutrons energy is not analyzed, the corresponding measurement is called differential cross section.

$$\frac{\mathrm{d}\sigma}{\mathrm{d}\Omega}=\int\frac{\mathrm{d}^2\sigma}{\mathrm{d}\Omega\mathrm{d}E'}\,\mathrm{d}E'=\frac{n'(2\psi,\varphi)}{\Phi\mathrm{d}\Omega} \tag{2.28}$$

The cross sections are the quantities measured in a scattering experiment. The next step is to derive theoretical expressions for these quantities. In the present Section, cross sections

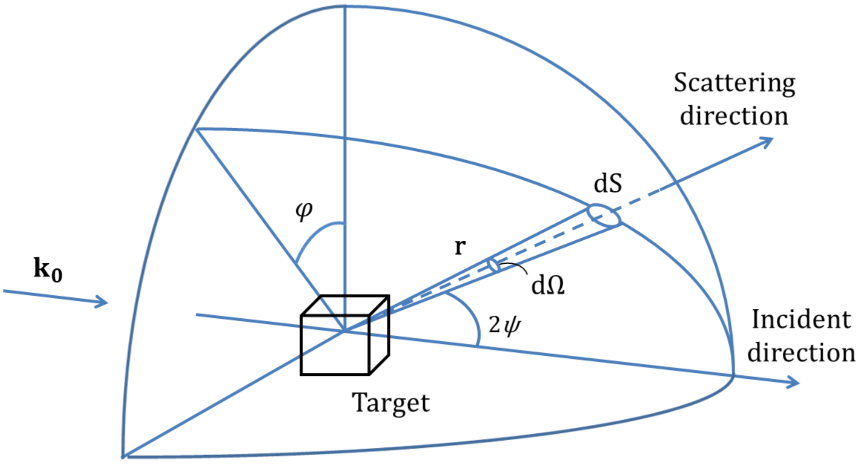

Fig. 2.2 Sketch of the scattering experiment geometry. Neutrons with wave vector $\mathbf{k}_0$ from the incident beam are scattered on the target, the 2ψ and φ define the resulting scattering direction, $\mathrm{d}\Omega$ is a solid angle.

σ are quoted per atomic concentration, *i.e.* $\mathrm{d}\Sigma/\mathrm{d}\Omega = \mathrm{d}\sigma/\mathrm{d}\Omega \cdot N/V_s$; also they do not take into account the initial and final spin states of the neutron. The definitions are extended to do this in the subsections about magnetic SANS (see Section 2.2.3).

In a general case, it is considered the differential scattering cross section $(\mathrm{d}\sigma/\mathrm{d}\Omega)_{\lambda\rightarrow\lambda'}$, representing the sum of all processes in which the state of the scattering system changes from λ to λ', and the state of the neutron changes from $\mathbf{k}$ to $\mathbf{k}'$. From this definition, the differential scattering cross section can be written as proportional to the sum of transition rates between each neutron state and each state of the scattering system [78]:

$$\left(\frac{\mathrm{d}\sigma}{\mathrm{d}\Omega}\right)_{\lambda\rightarrow\lambda'} = \frac{1}{\Phi}\frac{1}{\mathrm{d}\Omega}\sum_{\mathbf{k}'} W_{\mathbf{k},\lambda\rightarrow\mathbf{k}',\lambda'}, \tag{2.29}$$

where $W_{\mathbf{k},\lambda\rightarrow\mathbf{k}',\lambda'}$ is the number of transitions per second from the state $\mathbf{k},\lambda$ to the state $\mathbf{k}',\lambda'$. In order to evaluate the expression on the right-hand side of Eq. (2.29), there must be taken several assumptions. The first assumption is known as Fermi's golden rule which describes the transition rate $W_{\mathbf{k},\lambda\rightarrow\mathbf{k}',\lambda'}$ assuming that the rate is independent of time:

$$\sum_{\mathbf{k}'} W_{\mathbf{k},\lambda\rightarrow\mathbf{k}',\lambda'} = \frac{2\pi}{\hbar}\rho_{\mathbf{k}'}|\langle\mathbf{k}'\lambda'|V|\mathbf{k}\lambda\rangle|^2, \tag{2.30}$$

with V being a neutron potential and $\rho_{\mathbf{k}'}$ being the density of states (the number of momentum states in $\mathrm{d}\Omega$ per unit energy range for a neutron in the state $\mathbf{k}'$). With Eq. (2.29) and taking into account the energy conservation law, the partial differential scattering cross section from Eq. (2.27) can be written as

$$\left(\frac{\mathrm{d}^2\sigma}{\mathrm{d}\Omega \mathrm{d}E'}\right)_{\lambda\to\lambda'} = \frac{k'}{k}\left(\frac{m}{2\pi\hbar^2}\right)^2 |\langle \mathbf{k}'\lambda'|V|\mathbf{k}\lambda\rangle|^2 \delta(E_{\lambda'} - E_\lambda + E_{\mathbf{k}'} - E_{\mathbf{k}}), \tag{2.31}$$

where $\delta(E_{\lambda'} - E_\lambda + E_{\mathbf{k}'} - E_{\mathbf{k}})$ represents the energy conservation law, and $\hbar$ is the reduced Plank constant. The next approximation is the usage of Fermi's pseudopotential. It assumes the interaction potential V to be short-ranged (replacing the distance dependence with Dirac delta function) and spherically symmetric. For a general scattering system, the Fermi's pseudopotential reads

$$V_j(\mathbf{x}_j) = \frac{2\pi\hbar^2}{m} b_j \delta(\mathbf{x}_j), \tag{2.32}$$

where b_j is scattering length of the jth nucleus, $\mathbf{x}_j = \mathbf{r} - \mathbf{R}_j$, and $\mathbf{R}_j$ is the position vector of the jth nucleus. We recall that our entire derivation of the cross section is based on Fermi's golden rule, which for scattering processes is equivalent to the Born approximation; both are based on first-order perturbation theory. In fact, the conditions for this theory do not hold for the nuclear scattering of thermal neutrons. The justification for the use of the golden rule in these circumstances is that, when combined with the pseudopotential, it gives the required result of isotopic scattering for a single fixed nucleus [78].

The resulting expression is the basic expression for the partial differential cross section for nuclear scattering [78]:

$$\frac{\mathrm{d}^2\sigma_N}{\mathrm{d}\Omega \mathrm{d}E'} = \frac{k'}{k}\frac{1}{2\pi\hbar}\sum_{jj'} b_j b_j' \int_{-\infty}^{\infty} \langle \exp(-i\mathbf{q}\cdot\mathbf{R}_{j'}(0))\exp(i\mathbf{q}\cdot\mathbf{R}_j(t))\rangle \exp(-i\omega t)\,\mathrm{d}t, \tag{2.33}$$

where b_j and b_j' are scattering lengths of the nuclei, j and j' are the nucleus indexes, $\mathbf{q} = \mathbf{k} - \mathbf{k}'$ is the scattering vector, $\mathbf{R}_j(t) = \exp(iHt/\hbar)\mathbf{R}_j(0)\exp(-iHt/\hbar)$ is the time-dependent Heisenberg operator, with H being a Hamiltonian of the scattering system, and angular frequency ω is defined by $\hbar\omega = E - E'$. Note though the expression Eq. (2.33) may appear simple, its evaluation is a difficult task, except for the most elementary scattering systems.

One of the ways to bring the evaluation problem closer to the "practical" solution is taking averaged values of a scattering length b_j. Consider a scattering system containing a large number of nuclei - a condition usually well satisfied - where the scattering length b varies from one nucleus to another owing to nuclear spin or the presence of isotopes (or both). Let all possible values of a scattering length densities b_j occur with corresponding frequencies f_j, having a mean value $\bar{b}$. In such case, the partial differential cross section can be divided into two contributions [78]

$$\frac{\mathrm{d}^2\sigma_N}{\mathrm{d}\Omega\mathrm{d}E'} = \left(\frac{\mathrm{d}^2\sigma}{\mathrm{d}\Omega\mathrm{d}E'}\right)_{\mathrm{coh}} + \left(\frac{\mathrm{d}^2\sigma}{\mathrm{d}\Omega\mathrm{d}E'}\right)_{\mathrm{inc}}, \tag{2.34}$$

with coherent scattering

$$\left(\frac{\mathrm{d}^2\sigma}{\mathrm{d}\Omega\mathrm{d}E'}\right)_{\mathrm{coh}} = \frac{\sigma_{\mathrm{coh}}}{4\pi}\frac{k'}{k}\frac{1}{2\pi\hbar}\sum_{jj'}\int_{-\infty}^{\infty}\langle\exp(-i\mathbf{q}\cdot\mathbf{R}_{j'}(0))\exp(i\mathbf{q}\cdot\mathbf{R}_{j}(t))\rangle\ \exp(-i\omega t)\ \mathrm{d}t, \tag{2.35}$$

and incoherent scattering

$$\left(\frac{\mathrm{d}^2\sigma}{\mathrm{d}\Omega\mathrm{d}E'}\right)_{\mathrm{inc}} = \frac{\sigma_{\mathrm{inc}}}{4\pi}\frac{k'}{k}\frac{1}{2\pi\hbar}\sum_{j}\int_{-\infty}^{\infty}\langle\exp(-i\mathbf{q}\cdot\mathbf{R}_{j}(0))\exp(i\mathbf{q}\cdot\mathbf{R}_{j}(t))\rangle\ \exp(-i\omega t)\ \mathrm{d}t, \tag{2.36}$$

where $\sigma_{\mathrm{coh}} = 4\pi(\bar{b})^2$ and $\sigma_{\mathrm{inc}} = 4\pi(\bar{b^2} - (\bar{b})^2)$, with $\bar{b}^2$ and $\bar{b^2}$ being respectively the square of average of scattering length and average of squared scattering length. Note that while Eq. (2.35) depends on the correlation between the positions of both the same nucleus and different nuclei at different times (therefore, it gives interference effects), Eq. (2.36) depends on the correlation between the positions of only the same nucleus at different times (so it does not give interference effects). The physical interpretation is the following: the coherent scattering is the scattering, which the same system would give if all the scattering lengths were equal to $\bar{b}$. The incoherent scattering is the term must be added to the coherent scattering, in order to obtain the scattering due to the actual system. Physically the incoherent scattering arises from the random distribution of the deviations of the scattering lengths from their mean value. Note that the expression for σ_{inc} is actually proportional to the discrete random variance of b_j. For example, if the scattering system is a crystal of NaCl, the coherent scattering is that due to a hypothetical crystal in which all the sodium nuclei have scattering lengths equal $\bar{b}$ for sodium, and all the chlorine nuclei have scattering length equal to $\bar{b}$ for chlorine. The incoherent scattering is the sum of the incoherent scattering from the sodium nuclei and the incoherent scattering from the chlorine nuclei.

In the present work, we restrict our interest specifically to the coherent part of neutron scattering; the incoherent term is considered to be subtracted from the data during the "data reduction" procedure, as it is described in Chapter 3.

The duration of a SANS experiment is usually much greater in comparison to single neutron scattering time. Now, we need to relate the neutron scattering cross sections to thermal averages of operators belonging to the scattering system. We define two functions: first is $I(\mathbf{q},t)$, known as the intermediate scattering function [78]

$$I(\mathbf{q},t) = \frac{1}{N}\sum_{jj'}\langle \exp\left(-i\mathbf{q}\cdot\mathbf{R}_{j'}(0)\right)\exp\left(i\mathbf{q}\cdot\mathbf{R}_j(t)\right)\rangle, \tag{2.37}$$

and the second is $S(\mathbf{q},\omega)$, known as the scattering function of the system

$$S(\mathbf{q},\omega) = \frac{1}{2\pi\hbar}\int I(\mathbf{q},t)\exp\left(-i\omega t\right)\,\mathrm{d}t. \tag{2.38}$$

The scattering cross section now may be expressed using the functions above:

$$\left(\frac{\mathrm{d}^2\sigma}{\mathrm{d}\Omega\mathrm{d}E'}\right)_{\mathrm{coh}} = \frac{\sigma_{\mathrm{coh}}}{4\pi}\frac{k'}{k}NS(\mathbf{q},\omega). \tag{2.39}$$

We now show that elastic scattering is directly related to the function $I(\mathbf{q},t)$ evaluated at $t\to\infty$. Note that elastic scattering occurs only in solid matter, not in liquids nor in gases. The function $I(\mathbf{q},t)$ tend to the same limit as t tends to $\pm\infty$ [78]:

$$I(\mathbf{q},t) = I(\mathbf{q},\infty) + I'(\mathbf{q},t), \tag{2.40}$$

where $I'(\mathbf{q},t\to\infty) = 0$.

Then the scattering function gives:

$$S(\mathbf{q},\omega) = \frac{1}{2\pi\hbar}\int_{-\infty}^{\infty}\left(I(\mathbf{q},\infty)+I'(\mathbf{q},t)\right)e^{-i\omega t}\,\mathrm{d}t = \frac{1}{\hbar}\delta(\omega)I(\mathbf{q},\infty) + \frac{1}{2\pi\hbar}\int_{-\infty}^{\infty}I'(\mathbf{q},t)e^{-i\omega t}\,\mathrm{d}t \tag{2.41}$$

Since $\hbar\omega$ is the change in the energy of the neutron, the first term corresponds to the elastic scattering and the second term corresponds to inelastic scattering. In the expressions above, there was considered a general case when the energy of the incident neutron is E, and energy of the scattered neutron is E'. Now we restrict the scattering to be only elastic, *i.e.* when $|\mathbf{k}| = |\mathbf{k}'|$. This gives for the partial differential cross section [78]

$$\left(\frac{\mathrm{d}^2\sigma}{\mathrm{d}\Omega\mathrm{d}E'}\right)_{\mathrm{coh\ el}} = \frac{\sigma_{\mathrm{coh\ el}}}{4\pi}\frac{N}{\hbar}\delta(\omega)I(\mathbf{q},\infty), \tag{2.42}$$

and for differential cross section

$$\left(\frac{\mathrm{d}\sigma}{\mathrm{d}\Omega}\right)_{\mathrm{coh\ el}} = \frac{\sigma_{\mathrm{coh\ el}}}{4\pi}NI(\mathbf{q},\infty) \tag{2.43}$$

In the Eq. (2.37) with $t \to \infty$, the correlation between $\mathbf{R}_{j'}(0)$ and $\mathbf{R}_{j'}(\infty)$ becomes independent of time. Introducing the particle density operator

$$\rho(\mathbf{r}) = \sum_j \delta\left(\mathbf{r} - \mathbf{R}_j(0)\right) \tag{2.44}$$

with $\langle \rho(\mathbf{r}) \rangle$ being a thermal average of $\rho(\mathbf{r})$ at temperature T, allows us to express the intermediate scattering function as

$$NI(\mathbf{q}, \infty) = \left| \int \langle \rho(\mathbf{r}) \rangle e^{i\mathbf{q}\mathbf{r}} \mathrm{d}\mathbf{r} \right|^2 , \tag{2.45}$$

and the partial cross section

$$\left(\frac{\mathrm{d}\sigma}{\mathrm{d}\Omega}\right)_{\text{coh el}} = \frac{\sigma_{\text{coh el}}}{4\pi} \left| \int \langle \rho(\mathbf{r}) \rangle e^{i\mathbf{q}\mathbf{r}} \, \mathrm{d}\mathbf{r} \right|^2 \tag{2.46}$$

Now we assume an assembly of N identical scatterers of finite size. With that, we can separate the scattering from within the single particle from the interference between different particles [78].

$$\left(\frac{\mathrm{d}\sigma}{\mathrm{d}\Omega}\right)_{\text{coh el}} = \frac{\sigma_{\text{coh el}}}{4\pi} \left| \sum_{j=1}^{N} \rho_j^{\text{tot}} F_j(\mathbf{q}) e^{i\mathbf{q}\cdot\mathbf{r}_j} \right|^2 \tag{2.47}$$

where ρ_j^{tot} denotes total scattering power of the particle and $F_j(\mathbf{q})$ denotes a single particle form factor. Form factor $F_j(\mathbf{q})$ is defined as the normalized amplitude of scattering from within one particle with volume V_j

$$F_j(\mathbf{q}) = \frac{\int_{V_j} \rho_j(\mathbf{r}) e^{i\mathbf{q}\mathbf{r}'} \, \mathrm{d}^3 r'}{\int_{V_j} \rho_j(\mathbf{r}) \, \mathrm{d}^3 r'} \tag{2.48}$$

and for the case of a hard spherical particle with radius R reads $F(q) = 3 j_1(qR)/(qR)$, where $j_1(x)$ is a Bessel spherical function of the first kind.

In all above derivations, we assumed plane waves as initial and final states of a neutron. Now, let us consider the case of a "real" experiment. In the incident beam, a wave packet is produced by collimation (defining the direction of the beam) and monochromatization (defining the wavelength of the incident beam). Neither the direction $\mathbf{k}$ nor the wavelength λ have sharp values but rather have a distribution of finite width about their respective mean values. This wave packet can be described as a superposition of plane waves, and, as a consequence, the diffraction pattern will be a superposition of patterns for different incident wavevectors $\mathbf{k}$. The question arises, which information is lost due to these non-ideal conditions. This instrumental resolution is intimately connected with the coherence of the beam. Coherence is needed so that the interference pattern is not significantly destroyed. Coherence requires a phase relationship between the different components of the beam. Generally, two types of coherence can be distinguished.

First is a longitudinal (temporal) coherence - coherence of the beam. A measure for the longitudinal coherence is given by the length, on which two components of the beam with largest wavelength difference (λ and $\lambda+\Delta\lambda$) become fully out of phase [79].

$$l_{\parallel} = \frac{\lambda^2}{2\Delta\lambda}$$

The second is a transversal coherence - due to source extension. Because of the extension of the source (transverse beam size), the phase relation is destroyed for large source size or large divergence. The transversal coherence length is given by [79]

$$l_{\perp} = \frac{\lambda}{2\Delta\Psi},$$

where $\Delta\Psi$ is the divergence of the beam.

Together, the longitudinal and the two transversal coherence lengths (in two directions perpendicular to the beam propagation) define a coherence volume. This is a measure for a volume within the sample, in which the amplitudes of all scattered waves superimpose to produce an interference pattern. Normally, the coherence volume is significantly smaller than the sample size, typically a few 100 Å for neutron scattering, up to μm for synchrotron radiation. Scattering between different coherence volumes within the sample is no longer coherent, *i. e.* not the amplitudes but intensities of the contributions to the scattering pattern have to be added. This limits the real space resolution of a scattering experiment to the extension of the coherence volume.

$$V_{coh} = l_{\parallel} \cdot l_{\perp} \cdot l_{\perp}$$

In order to calculate the values of the coherence volume for the current experiment, let us take typical values, used in a SANS experiment: $\lambda = 6\,\mathrm{nm}$, $\Delta\lambda = 0.15\,\lambda$ and $\Delta\Psi = 0.9^\circ$. That gives $l_{\parallel} \approx 3\cdot 10^{-8}\,\mathrm{m}$ and $l_{\perp} \approx 1.91\cdot 10^{-7}\,\mathrm{m}$ with resulting

$$l_{coh} = \sqrt[3]{V_{coh}} \approx 10^{-7}\,\mathrm{m}$$

From a practical point of view, this value represents an upper bond of the lengths, distinguished in a SANS experiment.

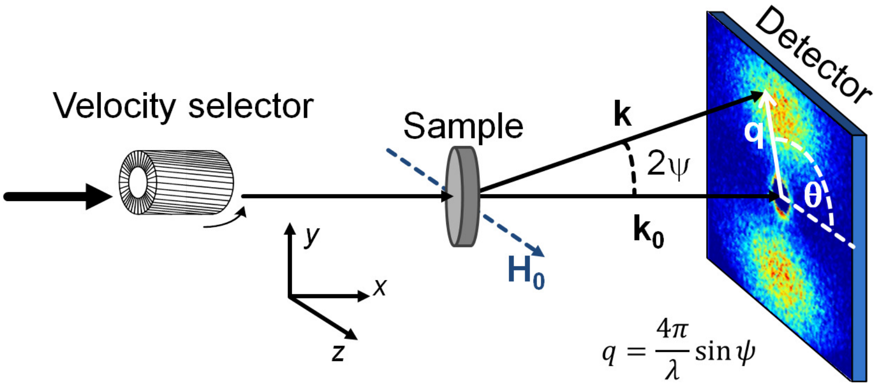

Fig. 2.3 Sketch of the perpendicular SANS geometry, where the applied magnetic field $\mathbf{H}_0$ is perpendicular to the wave vector $\mathbf{k}_0$ of the incoming neutron beam. The scattering vector $\mathbf{q}$ is defined as the difference between the wave vectors of the scattered $\mathbf{k}$ and incident neutrons $\mathbf{k}_0$; its magnitude $q = |q| = (4\pi/\lambda)\sin\,\psi$ depends on the mean wavelength λ of the neutrons (selected by the velocity selector) and on the scattering angle $2\,\psi$. The angle θ is the angle between $\mathbf{H}_0$ and $\mathbf{q}$ in the plane of the detector.

2.2.3 Magnetic SANS cross sections

Figure 2.3 depicts a typical sketch of the magnetic small-angle neutron scattering experiment. The applied magnetic field $\mathbf{H}_0 = H_0\,\mathbf{e}_z$ is perpendicular to the wave vector $\mathbf{k}_0 = k_0\,\mathbf{e}_x$ of the incoming neutron beam. We remind that the scattering is considered to be elastic ($k_0 = k = 2\pi/\lambda$) and that the component of $\mathbf{q}$ along the incident neutron beam q_x is neglected.

The magnetic interaction potential $V(\mathbf{r})$ is the interaction potential of the neutron magnetic dipole moment $\boldsymbol{\mu}_n$ and magnetic induction $\mathbf{B}(\mathbf{r})$. The expression for $V(\mathbf{r})$ is given by [80]

$$V(\mathbf{r}) = -\boldsymbol{\mu}_n \cdot \mathbf{B}(\mathbf{r}) = -\mu_n \boldsymbol{\sigma} \cdot \mathbf{B}(\mathbf{r}), \tag{2.49}$$

where $\boldsymbol{\sigma}$ is the Pauli operator, μ_n is the neutron magnetic moment and $\mathbf{B}(\mathbf{r})$ is the magnetic induction. The corresponding Fourier transform of the interaction potential is given by

$$\widetilde{V}(\mathbf{q}) = -\mu_n \boldsymbol{\sigma} \cdot \widetilde{\mathbf{B}}(\mathbf{q}) \tag{2.50}$$

with the Fourier transform of magnetic induction being

$$\widetilde{\mathbf{B}}(\mathbf{q}) = \mu_0 \mathbf{Q} = \mu_0 \frac{\mathbf{q} \times [\mathbf{M} \times \mathbf{q}]}{q^2}. \tag{2.51}$$

The Halpern-Johnson vector $\mathbf{Q}$ projects the magnetization vector $\mathbf{M}$ on the plane perpendicular to $\mathbf{q}$. From the properties of the Pauli operator, the expression for the $\widetilde{V}(\mathbf{q})$ results in

$$\widetilde{V}(\mathbf{q}) = -\mu_0\mu_n\boldsymbol{\sigma}\cdot\mathbf{Q} = -\mu_0\left[\left(\begin{smallmatrix}0 & 1\\ 1 & 0\end{smallmatrix}\right)Q_x + \left(\begin{smallmatrix}0 & -i\\ i & 0\end{smallmatrix}\right)Q_y + \left(\begin{smallmatrix}1 & 0\\ 0 & -1\end{smallmatrix}\right)Q_z\right] \tag{2.52}$$

With all the considerations above, for the elastic neutron spin-dependent atomic scattering cross section [50]

$$\frac{\mathrm{d}\sigma_{\mathrm{mag}}}{\mathrm{d}\Omega} = |\langle S^z|V|S_0^z\rangle| = \langle S^z|b_N + b_M\frac{\mathbf{Q}}{|\mathbf{Q}|}\cdot\boldsymbol{\sigma}|S_0^z\rangle|^2, \tag{2.53}$$

where b_N denotes the nuclear scattering length and b_M denotes the magnetic scattering amplitude. In case of forward scattering ($q_{\mathrm{x}} \approx 0$) $b_M = b_H\mu_a$ with $b_H = 2.7\cdot 10^{-15}\mathrm{m}/\mu_B$ and μ_a being the atomic magnetic moment [13].

Assuming the fact that we know the initial and final states of neutron, we can express the scattering cross sections for each combination of the neutron initial and final spin states:

$$\frac{\mathrm{d}\Sigma^{\pm\pm}}{\mathrm{d}\Omega} = \frac{1}{V}\sum_{i,j} e^{-i\mathbf{q}\cdot\mathbf{r}_{i,j}}\left(b_{N,i}b_{N,j}^{\star} \pm b_{N,i}b_H Q_{z,j}^{\star} \pm b_H Q_{z,i}b_{N,j}^{\star} + b_H^2 Q_{z,i}Q_{z,i}^{\star}\right) \tag{2.54}$$

and

$$\frac{\mathrm{d}\Sigma^{\pm\mp}}{\mathrm{d}\Omega} = \frac{1}{V}\sum_{i,j} e^{-i\mathbf{q}\cdot\mathbf{r}_{i,j}}b_H^2\left(Q_{x,i}Q_{x,j}^{\star} + Q_{y,i}Q_{y,j}^{\star} \mp i\mathbf{e}_z\cdot\mathbf{Q}_i\times\mathbf{Q}_j\right), \tag{2.55}$$

where the first superscript (*e.g.*, "+") that is attached to $\mathrm{d}\Sigma/\mathrm{d}\Omega$ refers to the spin state of the incident neutrons, whereas the second one (*e.g.*, "−") specifies the spin state of the scattered neutrons, V denotes the scattering volume, $\mathbf{r}_{i,j} = \mathbf{r}_i - \mathbf{r}_j$, $b_{N,i}$, and b_H correspond to the coherent nuclear and magnetic scattering lengths defined above and "*" refers to the complex conjugate quantities. Note that the spin-flip scattering cross sections contain a polarization-dependent term $i\mathbf{e}_z\cdot\mathbf{Q}_i\times\mathbf{Q}_j$, where $\mathbf{e}_z$ specifies the polarization direction of the incoming neutron beam. This chiral contribution can appear for spin configurations that have no inversion symmetry. These non-collinear magnetic structures characterize an axial vector $\mathbf{C}$ [81]. For example, in an antiferromagnetic helix phase, the direction of spiral rotation indicates chirality $\mathbf{C}$. If there is an anisotropic distribution of the helical orientations, an effective chirality vector $\mathbf{C} \neq 0$ results and an elastic, chiral scattering can be observed. In addition, the dynamic chirality of spin waves in ferromagnets can be investigated by inelastic chiral scattering [81]. In the absence of such contributions in Eq. (2.55), the two spin-flip scattering cross sections are identical and independent of the polarization of the incoming neutron beam. This is further discussed in Section 2.4. The non-spin flip channels, on the other hand, always contain two polarization dependent terms.

Since $\mathbf{H}_0$ is along $\mathbf{e}_z$ and the incident neutron beam is oriented along $\mathbf{e}_x$, the Halpern-Johnson vector can be written as

$$\mathbf{Q} = \begin{pmatrix} -M_x \\ -M_y \cos^2\theta + M_z \sin\theta\cos\theta \\ -M_z \sin^2\theta + M_y \sin\theta\cos\theta \end{pmatrix}. \tag{2.56}$$

In case of unpolarized neutron beam with no spin resolution, the scattering cross section $\mathrm{d}\Sigma/\mathrm{d}\Omega$ is a sum of all cross sections from Eqs. (2.54) and (2.55):

$$\frac{\mathrm{d}\Sigma}{\mathrm{d}\Omega} = \frac{1}{V}\sum_{i,j} e^{-i\mathbf{q}\cdot\mathbf{x}_{i,j}} \left(b_{N,i}b^{\star}_{N,j} + b_{H,i}b^{\star}_{H,j}Q_{z,i}Q^{\star}_{z,j}\right) + \frac{1}{V}\sum_{i,j} e^{-i\mathbf{q}\cdot\mathbf{x}_{i,j}} b_{H,i}b^{\star}_{H,j}\left(Q_{x,i}Q^{\star}_{x,j} + Q_{y,i}Q^{\star}_{y,j}\right) \tag{2.57}$$

In this work, we consider the neutron small-angle scattering along the forward direction, which arises from nanoscale variations of the nuclear scattering density and the magnitude and orientation of the magnetization vector field $\mathbf{M}(\mathbf{r})$ [82–85]. Since SANS generally provides no sub-nm resolution and thus no information about the structure on an atomic scale, we can express the discrete sums by Fourier integrals of a continuous nuclear scattering density $N(\mathbf{r})$ and replace the magnetization $\mathbf{M}(\mathbf{r})$ with the corresponding Fourier transforms. We define the continuous nuclear $N(\mathbf{r})$ and magnetic $\mathbf{M}(\mathbf{r})$ scattering length densities with their respective Fourier transforms $\widetilde{N}(\mathbf{q})$ and $\widetilde{\mathbf{M}}(\mathbf{q})$ as [86]

$$N(\mathbf{r}) = \sum_{\alpha} b_{N,\alpha}\rho_{\alpha}(\mathbf{r}) \leftrightarrow \widetilde{N}(\mathbf{q}) = \frac{1}{(2\pi)^{3/2}} \int N(\mathbf{r}) e^{-i\mathbf{q}\cdot\mathbf{r}}\, \mathrm{d}^3 r \tag{2.58}$$

and

$$\mathbf{M}(\mathbf{r}) = \sum_{\alpha} \mu_{\alpha}\rho_{\alpha}(\mathbf{r})\mathbf{m}_{\alpha}(\mathbf{r}) \leftrightarrow \widetilde{\mathbf{M}}(\mathbf{q}) = \frac{1}{(2\pi)^{3/2}} \int \mathbf{M}(\mathbf{r}) e^{-i\mathbf{q}\cdot\mathbf{r}}\, \mathrm{d}^3 r \tag{2.59}$$

with α being an alloy component, $\rho_{\alpha}(\mathrm{r})$ - atomic density, μ_{α} - magnitude of magnetic moment and $\mathbf{m}_{\alpha}$ - a magnetization unit vector. Using integral expressions (2.58) and (2.59), the elastic unpolarized SANS cross section $\mathrm{d}\Sigma/\mathrm{d}\Omega$ can be written as [13]:

$$\begin{aligned} \frac{\mathrm{d}\Sigma}{\mathrm{d}\Omega}(\mathbf{q}) = \frac{8\pi^3}{V} b_H^2 \Bigg(& \frac{|\widetilde{N}|^2}{b_H^2} + |\widetilde{M}_x|^2 + |\widetilde{M}_y|^2\cos^2\theta + \\ & |\widetilde{M}_z|^2\sin^2\theta - (\widetilde{M}_y\widetilde{M}_z^* + \widetilde{M}_y^*\widetilde{M}_z)\sin\theta\cos\theta \Bigg), \end{aligned} \tag{2.60}$$

where $\mathbf{q}$ denotes the scattering or momentum-transfer vector, V is the scattering volume, the constant b_H relates the atomic magnetic moment to the Bohr magneton, $\widetilde{N}(\mathbf{q})$ and $\widetilde{\mathbf{M}}(\mathbf{q})$ denote, respectively, the Fourier coefficients of the nuclear scattering-length density and of the magnetization $\mathbf{M}(\mathbf{r})$, θ is the angle between $\mathbf{H}_0$ and $\mathbf{q}$ so that $\mathbf{q} \cong q\{0,\ \sin\theta,\ \cos\theta\}$, and the asterisks "$*$" mark the complex-conjugated quantity.

At a saturating field, the magnetization reads $\mathbf{M}(\mathbf{r}) = \{0, 0, M_s(\mathrm{r})\}$, and the two remaining sources of scattering are the nuclear scattering and the scattering due to the saturation magnetization contrast. In such case, $\mathrm{d}\Sigma/\mathrm{d}\Omega$ reduces to the so-called residual scattering cross section

$$\frac{\mathrm{d}\Sigma_{\mathrm{res}}}{\mathrm{d}\Omega}(\mathbf{q}) = \frac{8\pi^3}{V}\left(|\widetilde{N}|^2 + b_H^2|\widetilde{M}_s|^2\sin^2\theta\right), \tag{2.61}$$

while for magnetic fields below saturation one may express the total cross section $\mathrm{d}\Sigma/\mathrm{d}\Omega$ as

$$\frac{\mathrm{d}\Sigma}{\mathrm{d}\Omega}(\mathbf{q}) = \frac{\mathrm{d}\Sigma_{\mathrm{res}}}{\mathrm{d}\Omega}(\mathbf{q}) + \frac{\mathrm{d}\Sigma_M}{\mathrm{d}\Omega}(\mathbf{q}), \tag{2.62}$$

where

$$\begin{aligned}\frac{\mathrm{d}\Sigma_M}{\mathrm{d}\Omega}(\mathbf{q}) = \frac{8\pi^3}{V}b_H^2\Big(|\widetilde{M}_x|^2 + |\widetilde{M}_y|^2\cos^2\theta + \left(|\widetilde{M}_z|^2 - |\widetilde{M}_s|^2\right)\sin^2\theta - \\ (\widetilde{M}_y\widetilde{M}_z^* + \widetilde{M}_y^*\widetilde{M}_z)\sin\theta\cos\theta\Big)\end{aligned} \tag{2.63}$$

denotes the so-called spin-misalignment SANS cross section. Note that $\widetilde{M}_z \cong \widetilde{M}_s$ in the approach-to-saturation regime, so that in this case $\mathrm{d}\Sigma_M/\mathrm{d}\Omega$ reduces to

$$\frac{\mathrm{d}\Sigma_M}{\mathrm{d}\Omega}(\mathbf{q}) = \frac{8\pi^3}{V}b_H^2\left(|\widetilde{M}_x|^2 + |\widetilde{M}_y|^2\cos^2\theta - (\widetilde{M}_y\widetilde{M}_z^* + \widetilde{M}_y^*\widetilde{M}_z)\sin\theta\cos\theta\right). \tag{2.64}$$

$\mathrm{d}\Sigma_M/\mathrm{d}\Omega$ contains the purely magnetic scattering due to the transversal spin components, with related Fourier amplitudes $\widetilde{M}_x(\mathbf{q})$ and $\widetilde{M}_y(\mathbf{q})$. Note that $\mathrm{d}\Sigma_M/\mathrm{d}\Omega$ also depends on spatial variations of the magnetization via the longitudinal Fourier component $\widetilde{M}_z$ in the $\widetilde{M}_y$-$\widetilde{M}_z$ cross term.

An example of a spin-misalignment cross section from Eq. (2.64) is given in Fig. 2.4. Note that the angular anisotropy of Eq. (2.64) is given not only by trigonometrical functions $\cos^2\theta$ and $\sin\theta\cos\theta$; in fact, the Fourier components themselves may be anisotropic. That makes the resulting spin-misalignment cross section highly anisotropic in most cases, and also suggests that the anisotropy may be field-dependent. On the figure, with the field decreasing from 163 mT to 45 mT, the anisotropy changes from "clover-leaf" to the "horizontal ellipse"-type.

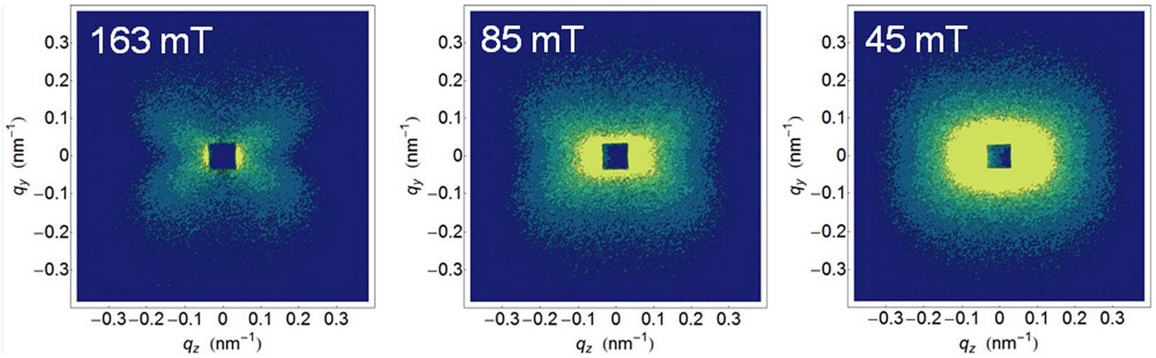

Fig. 2.4 Experimental spin-misalignment SANS cross sections of $Fe_{89}Zr_7B_3Cu$ [87] as observed on the 2D detector of the SANS scattering experiment (as depicted in Fig 2.3) at selected applied magnetic fields. $\mathbf{H}_0$ is horizontal in the plane.

2.2.4 Magnetic spin-misalignment SANS within micromagnetics approach

In the present Section, we use the expressions of the Fourier coefficients of the magnetization vector from Eqs. (2.25) and (2.26) for the evaluation of spin-misalignment SANS cross sections introduced in Section above. We remind, that in the approach of small-angle neutron scattering moment-transfer vector $\mathbf{q}$ is defined only in the plane of the detector: in case of perpendicular scattering geometry when $\mathbf{k}_0 \perp \mathbf{H}_0$ that means $\mathbf{q} = \{0,\, q_y,\, q_z\} = \{0,\, q\, \sin\theta,\, q\, \cos\theta\}$. Substituting that into Eqs. (2.25) and (2.26) gives

$$\widetilde{M}_x^2(\mathbf{q}) = M_s^2 \frac{\widetilde{H}_p^2(\mathbf{q})}{2H_{\mathrm{eff}}(q)^2}, \tag{2.65}$$

and

$$\widetilde{M}_y^2(\mathbf{q}) = M_s^2 \frac{\widetilde{H}_p^2(\mathbf{q})^2 + 2\widetilde{M}_z^2(\mathbf{q})\sin^2\theta\cos^2\theta}{2(H_{\mathrm{eff}}(q) + M_s\sin^2\theta)^2}, \tag{2.66}$$

and the cross-term

$$-(\widetilde{M}_y^*\widetilde{M}_z + \widetilde{M}_y\widetilde{M}_z^*) = M_s \frac{2\widetilde{M}_z^2(\mathbf{q})\sin\theta\cos\theta}{H_{\mathrm{eff}}(q) + M_s\sin^2\theta}. \tag{2.67}$$

With the expressions above, the cross section from Eq. (2.64) further decomposes into two contributions, which are related to the two main sources of the magnetic moments disorder (see the discussion in the beginning of Section 2.1). The first contribution, $S_H R_H$ is due to perturbing magnetic anisotropy fields and the second contribution $S_M R_M$ is related to magnetostatic fields. We remind the reader that the expressions Eqs. (2.65)–(2.67) were derived in the assumption of the case near magnetic saturation and for a weakly inhomogeneous bulk ferromagnet [24]. Also, note that the micromagnetic SANS theory considers a uniform exchange interaction and a random distribution of magnetic easy axes, but takes explicitly into account variations in the magnitude of the magnetization (via the function S_M, see Eq. (2.70) below). The expression for the spin-misalignment SANS cross section based on the two contributions of magnetic moments disorder reads:

$$\frac{\mathrm{d}\Sigma_M}{\mathrm{d}\Omega}(\mathbf{q}) = S_H(\mathbf{q})\, R_H(\mathbf{q}, H_i) + S_M(\mathbf{q})\, R_M(\mathbf{q}, H_i) \tag{2.68}$$

The anisotropy-field scattering function (in units of $\mathrm{cm}^{-1}\mathrm{sr}^{-1}$)

$$S_H(\mathbf{q}) = \frac{8\pi^3}{V}\, b_H^2\, |\widetilde{H}_p|^2 \tag{2.69}$$

depends on the Fourier coefficient $\widetilde{H}_p(\mathbf{q})$ of the magnetic anisotropy field, whereas the scattering function of the longitudinal magnetization (in units of $\mathrm{cm}^{-1}\mathrm{sr}^{-1}$)

$$S_M(\mathbf{q}) = \frac{8\pi^3}{V}\, b_H^2\, |\widetilde{M}_z|^2 \tag{2.70}$$

provides information on the magnitude $\Delta M \propto \widetilde{M}_z$ of the magnetization jump at internal (*e.g.* particle-matrix) interfaces. The corresponding (dimensionless) micromagnetic response functions can be expressed as

$$R_H(q, \theta, H_i) = \frac{p^2}{2}\left(1 + \frac{\cos^2\theta}{\left(1 + p\sin^2\theta\right)^2}\right) \tag{2.71}$$

and

$$R_M(q, \theta, H_i) = \frac{p^2 \sin^2\theta \cos^4\theta}{\left(1 + p\sin^2\theta\right)^2} + \frac{2p\sin^2\theta\cos^2\theta}{1 + p\sin^2\theta}, \tag{2.72}$$

where

$$p(q, H_\mathrm{i}) = \frac{M_s}{H_\mathrm{eff}(q, H_i)} \tag{2.73}$$

is a (dimensionless) function. The effective magnetic field

$$H_\mathrm{eff}(q, H_i) = H_i\left(1 + l_H^2 q^2\right) \tag{2.74}$$

depends on the internal magnetic field

$$H_i = H_0 - N_d M_s, \tag{2.75}$$

on $q = |\mathbf{q}|$, and on the exchange length

$$l_H(H_i) = \sqrt{\frac{2A}{\mu_0 M_s H_i}} \tag{2.76}$$

(M_s: saturation magnetization; A: exchange-stiffness parameter; $0 < N_d < 1$: demagnetizing factor; $\mu_0 = 4\pi 10^{-7}\,\mathrm{Tm/A}$). The θ-dependence of R_H and R_M is essentially a consequence of the magnetodipolar interaction. Depending on the values of q and H_i, and on the ratio $H_p/\Delta M$, a variety of angular anisotropies may be seen on a two-dimensional detector (see, *e.g.* Fig. 2.4) [88, 13].

One can perform an azimuthal average of Eq. (2.68), *i.e.* $(2\pi)^{-1}\int_0^{2\pi}(...)d\theta$. The resulting expressions for the response functions then read

$$R_H(q, H_i) = \frac{p^2}{4}\left(2 + \frac{1}{\sqrt{1+p}}\right) \tag{2.77}$$

and

$$R_M(q, H_i) = \frac{\sqrt{1+p} - 1}{2}, \tag{2.78}$$

so that the azimuthally-averaged total nuclear and magnetic unpolarized SANS cross section of a bulk ferromagnet can be written as

$$\frac{\mathrm{d}\Sigma}{\mathrm{d}\Omega}(q) = \frac{\mathrm{d}\Sigma_{\mathrm{res}}}{\mathrm{d}\Omega}(q) + \frac{\mathrm{d}\Sigma_M}{\mathrm{d}\Omega}(q), \tag{2.79}$$

where

$$\frac{\mathrm{d}\Sigma_{\mathrm{res}}}{\mathrm{d}\Omega}(q) = \frac{8\pi^3}{V}\left(|\widetilde{N}(q)|^2 + \frac{1}{2}b_H^2\,|\widetilde{M}_z(q)|^2\right) \tag{2.80}$$

and

$$\frac{\mathrm{d}\Sigma_M}{\mathrm{d}\Omega}(q) = S_H(q)\,R_H(q, H_i) + S_M(q)\,R_M(q, H_i). \tag{2.81}$$

In order to use Eqs. (2.69) and (2.70), we have to specify certain models for the anisotropy-field scattering function and for the scattering function of the longitudinal magnetization. We assume the sample to be a statistically-isotropic nearly saturated bulk ferromagnet which exhibits (weak) spatial fluctuations of the saturation magnetization and the magnetic anisotropy field. For such a system, the functions $\widetilde{N}$, $\widetilde{M}_z$, and $\widetilde{H}_p$ to depend only on the magnitude $q = |\mathbf{q}|$ of the scattering vector. Furthermore, we assume a monodisperse scattering system and that both functions $\widetilde{H}_p^2(q)$ and $\widetilde{M}_z^2(q)$ can be written as the product of the *same* single-particle form factor $P(q)$ and structure factor $S(q)$ [89], *i.e.*

$$\widetilde{H}_p^2(q) = \frac{H_p^2}{(8\pi)^3} V_p^2 P(q) S(q) \tag{2.82}$$

and

$$\widetilde{M}_z^2(q) = \frac{(\Delta M)^2}{(8\pi)^3} V_p^2 P(q) S(q), \tag{2.83}$$

where V_p is the particle volume. Later on in the calculations, we will use (for illustration purposes) the Percus-Yevick hard-sphere structure factor for $S(q)$ [90] and (unless stated otherwise) the sphere form factor for $P(q)$,

$$P(q) = 9\,\frac{j_1^2(qR)}{(qR)^2}, \tag{2.84}$$

where $j_1(x)$ denotes the spherical Bessel function of first order. Any other particle form factor or structure factor may be straightforwardly implemented (see below). We also note that the characteristic structure sizes of $\widetilde{H}_p^2$ and $\widetilde{M}_z^2$ need not be identical; these are related, respectively, to the spatial extent of regions with uniform magnetic anisotropy field and saturation magnetization.

Under these assumptions (same size and shape), $\widetilde{H}_p^2(q)$ and $\widetilde{M}_z^2(q)$ differ only by constant prefactors, *i.e.* the magnitude H_p of the mean magnetic anisotropy field and the jump ΔM of the magnitude of the magnetization at internal interfaces. In fact, it is the ratio of $H_p/\Delta M$ which determines the angular anisotropy and the asymptotic power-law dependence of $\mathrm{d}\Sigma_M/\mathrm{d}\Omega$ as well as the characteristic decay length of spin-misalignment fluctuations [24].

2.3 Correlation function analysis

In the following section, we discuss the correlation function analysis of magnetic SANS, in particular, the behavior of the correlation function of the spin-misalignment cross section. While scattering cross sections such as in Eq. (2.60) provides the information on the sample's internal microstructure, it is defined in the reciprocal q-space. This may be in some way "counter-intuitive", since the data observed may not be directly compared to the real-space objects. An alternative real-space approach to analyzing SANS data is the computation of the (auto)correlation function of the system, for instance by means of the indirect Fourier-transformation technique [14–17], which has recently been extended to allow for the analysis of two-dimensional small-angle scattering patterns of oriented samples [18, 19]. For dilute, monodisperse, and uniform particle-matrix systems, several analytical expressions for the density-density autocorrelation function $\gamma(r)$ or, likewise, for the distance distribution function $p(r) = r^2\gamma(r)$ have been derived (see, *e.g.* [20]); this is a well-established procedure in small-angle x-ray scattering and in nuclear SANS, *e.g.* in the analysis of polymers [21] or in the study of the formation of magnetic nanocrystals in glass ceramics [22].

The section is organized as follows. In Section 2.3.1, we introduce the correlation function of nuclear scattering and the analogous autocorrelation function of the spin-misalignment. In Section 2.3.2, we introduce the correlation function of the spin-misalignment SANS. In Section 2.3.3, we present the study of the correlation function of the spin-misalignment SANS behavior depending on various parameters, based on the modeling computations. In Section 2.3.4, we present the comparison of the theoretical computations to the experimental data.

The results presented in the section are the part of the actual PhD work and were published in [76].

2.3.1 Correlation function of nuclear SANS and autocorrelation function of the spin-misalignment

Before addressing the magnetic correlation functions, we will briefly recall the corresponding well-known results from nuclear SANS theory [91–93]. The nuclear SANS cross section,

$$\frac{\mathrm{d}\Sigma_N}{\mathrm{d}\Omega}(\mathbf{q}) = \frac{8\pi^3}{V}|\widetilde{N}(\mathbf{q})|^2, \tag{2.85}$$

can be expressed in terms of the autocorrelation function $C_N(\mathbf{r})$ of the (excess) nuclear scattering-length density $N(\mathbf{r})$ (in units of m^{-2}) as

$$\frac{\mathrm{d}\Sigma_N}{\mathrm{d}\Omega}(\mathbf{q}) = \int C_N(\mathbf{r}) \exp(-i\mathbf{q}\cdot\mathbf{r})\, \mathrm{d}^3r, \tag{2.86}$$

where

$$C_N(\mathbf{r}) = \frac{1}{V}\int \Delta N(\mathbf{x})\,\Delta N(\mathbf{x}+\mathbf{r})\, \mathrm{d}^3x, \tag{2.87}$$

and

$$\widetilde{N}(\mathbf{q}) = \frac{1}{(2\pi)^{3/2}}\int N(\mathbf{r}) \exp(-i\mathbf{q}\cdot\mathbf{r})\, \mathrm{d}^3r. \tag{2.88}$$

The function $\Delta N(\mathbf{r}) = N(\mathbf{r}) - \langle N\rangle$ denotes the so-called excess scattering-length density, where $\langle N\rangle$ is the (constant) average scattering-length density, which only gives a contribution to $\mathrm{d}\Sigma_N/\mathrm{d}\Omega$ at $\mathbf{q}=0$. The back-transform of Eq. (2.86) is

$$C_N(\mathbf{r}) = \frac{1}{8\pi^3}\int \frac{\mathrm{d}\Sigma_N}{\mathrm{d}\Omega}(\mathbf{q})\,\exp(i\mathbf{q}\cdot\mathbf{r})\;\mathrm{d}^3q, \tag{2.89}$$

which for isotropic systems reduces to

$$C_N(r) = \frac{1}{2\pi^2}\int\limits_0^\infty \frac{\mathrm{d}\Sigma_N}{\mathrm{d}\Omega}(q)\,\frac{\sin(qr)}{qr}\,q^2\;\mathrm{d}q. \tag{2.90}$$

In analogy to the above formalism, one may define the autocorrelation function of the spin misalignment as [94–96]

$$C_{SM}(\mathbf{r}) = \frac{1}{V}\int \Delta\mathbf{M}(\mathbf{x})\,\Delta\mathbf{M}(\mathbf{x}+\mathbf{r})\;\mathrm{d}^3x, \tag{2.91}$$

where $\Delta\mathbf{M}(\mathbf{r}) = \mathbf{M}(\mathbf{r}) - \langle\mathbf{M}\rangle$ denotes the deviation of the local magnetization vector field $\mathbf{M}(\mathbf{r})$ from the mean magnetization $\langle\mathbf{M}\rangle$. Alternatively, $C_{SM}(\mathbf{r})$ can be expressed as

$$C_{SM}(\mathbf{r}) = \frac{1}{V}\int \left|\widetilde{\Delta\mathbf{M}}(\mathbf{q})\right|^2 \exp(i\mathbf{q}\cdot\mathbf{r})\;\mathrm{d}^3q, \tag{2.92}$$

where $\widetilde{\Delta\mathbf{M}}(\mathbf{q})$ is the Fourier transform of $\Delta\mathbf{M}(\mathbf{r})$. In the high-field limit, $\langle\mathbf{M}\rangle$ is nearly parallel to the applied magnetic field with $|\langle\mathbf{M}\rangle| \cong M_s$, so that $\Delta\mathbf{M}(\mathbf{r}) \cong \left\{M_x(\mathbf{r}), M_y(\mathbf{r}), 0\right\}$ and

$$C_{SM}(\mathbf{r}) = \frac{1}{V}\int \left(|\widetilde{M}_x(\mathbf{q})|^2 + |\widetilde{M}_y(\mathbf{q})|^2\right) \exp(i\mathbf{q}\cdot\mathbf{r})\;\mathrm{d}^3q. \tag{2.93}$$

Note that in our theory of magnetic SANS [24], the magnetization components $M_{x,y,z}(\mathbf{r})$ are all considered to be real-valued.

The comparison of Eqs. (2.87) and (2.91) reveals an important difference between nuclear and magnetic scattering (besides the fact that $\Delta N(\mathbf{r})$ is a scalar and $\Delta\mathbf{M}(\mathbf{r})$ a vector quantity). While the nuclear SANS cross section $\mathrm{d}\Sigma_N/\mathrm{d}\Omega$ is directly proportional to the Fourier transform $|\widetilde{N}(\mathbf{q})|^2$ of $C_N(\mathbf{r})$, the function $|\widetilde{\Delta\mathbf{M}}(\mathbf{q})|^2$ (being the Fourier transfrom of $C_{SM}(\mathbf{r})$) does not represent the experimentally measurable quantity $\mathrm{d}\Sigma_M/\mathrm{d}\Omega$, which is a weighted sum of the Cartesian Fourier components $\widetilde{M}_{x,y,z}(\mathbf{q})$ of the magnetization, according to Eq. (2.64).

2.3.2 Correlation function of the spin-misalignment SANS

Therefore, we *define* the correlation function $C(\mathbf{r})$ of the spin-misalignment SANS cross section as the Fourier transform of $\mathrm{d}\Sigma_M/\mathrm{d}\Omega$, for which there is a well-described theory, according to

$$C(\mathbf{r}) = \frac{1}{8\pi^3} \int \frac{\mathrm{d}\Sigma_M}{\mathrm{d}\Omega}(\mathbf{q}) \exp(i\mathbf{q}\cdot\mathbf{r})\, \mathrm{d}^3q; \tag{2.94}$$

and the normalized version of Eq. (2.94),

$$c(\mathbf{r}) = \frac{C(\mathbf{r})}{C(\mathbf{r}=0)} = \int \frac{\mathrm{d}\Sigma_M}{\mathrm{d}\Omega}(\mathbf{q}) \exp(i\mathbf{q}\cdot\mathbf{r})\, \mathrm{d}^3q \Big/ \int \frac{\mathrm{d}\Sigma_M}{\mathrm{d}\Omega}(\mathbf{q})\, \mathrm{d}^3q. \tag{2.95}$$

We emphasize that the $C(\mathbf{r})$ defined above is not an autocorrelation function, as are $C_N(\mathbf{r})$ from Eq. (2.89) and $C_{SM}(\mathbf{r})$ from Eq. (2.93). Likewise, the well-known result that the evaluation of $C_N(\mathbf{r})$ and $C_{SM}(\mathbf{r})$ at the origin $\mathbf{r} = 0$ yields, respectively, the mean-squared density fluctuation (Porod invariant) and the mean-squared magnetization fluctuation does not pertain to the correlation function of the spin-misalignment SANS $C(\mathbf{r})$; the integral of $\mathrm{d}\Sigma_M/\mathrm{d}\Omega$ over reciprocal space does not provide an obvious invariant of the spin-misalignment SANS.

Spin-misalignment cross section $\mathrm{d}\Sigma_M/\mathrm{d}\Omega$ at a particular applied magnetic field H_i can be (approximately) obtained by subtracting the total nuclear and magnetic scattering at a saturating field from the measurement of the total $\mathrm{d}\Sigma/\mathrm{d}\Omega$ at the particular H_i.

The spin-misalignment SANS cross section for the perpendicular scattering geometry depends on both the magnitude q and the direction θ of the scattering vector $\mathbf{q}$ on the detector (*e.g.* see Fig. 2.12 below). The θ-dependence of $\mathrm{d}\Sigma_M/\mathrm{d}\Omega$ is a consequence of the magnetodipolar interaction - via the Fourier coefficients $\widetilde{M}_{x,y,z}(q,\theta)$ [97, 24, 88] - and of the trigonometric functions which are explicitly contained in the cross section, Eq. (2.64), and are due to the dipolar nature of the neutron-magnetic interaction. The final expression for the (azimuthally) θ-averaged $\frac{\mathrm{d}\Sigma_M}{\mathrm{d}\Omega} = \frac{\mathrm{d}\Sigma_M}{\mathrm{d}\Omega}(q)$ does contain the averages over these degrees of freedom. Since from a practical point of view it is easier to work with one-dimensional data, *i.e.* with $\frac{\mathrm{d}\Sigma_M}{\mathrm{d}\Omega} = \frac{\mathrm{d}\Sigma_M}{\mathrm{d}\Omega}(q)$, Eq. (2.95) may be simplified to

$$c(r) = \frac{\int_0^\infty \frac{\mathrm{d}\Sigma_M}{\mathrm{d}\Omega}(q)\, j_0(qr)\, q^2\, \mathrm{d}q}{\int_0^\infty \frac{\mathrm{d}\Sigma_M}{\mathrm{d}\Omega}(q)\, q^2\, \mathrm{d}q}, \tag{2.96}$$

where $j_0(x) = \sin(x)/x$ denotes the zeroth-order spherical Bessel function. Note that spherical Bessel functions are denoted with a lower-case '*j*', whereas Bessel functions with an upper-case 'J'. From now on, the correlation function defined as in Eq. (2.96) is called the "one-dimsensional" correlation function of the spin-misalignment SANS cross section. Note that it has the same mathematical structure as the corresponding Eq. (2.90) for nuclear SANS. Also, since for statistically-isotropic bulk ferromagnets $\mathrm{d}\Sigma_M/\mathrm{d}\Omega$ in the parallel scattering geometry is isotropic (independent of the angle θ) [13], Eq. (2.96) also applies to $\mathbf{k}_0 \parallel \mathbf{H}_0$.

In a SANS experiment, only the components of the momentum-transfer vector $\mathbf{q}$ perpendicular to the incident-beam direction ($\mathbf{k}_0$) are effectively probed, which from a mathematical point of view means that the measured cross section represents already an average over the incident-beam direction. For $\mathbf{k}_0 \perp \mathbf{H}_0$ ($q_x \cong 0$), this implies that $\frac{\mathrm{d}\Sigma_M}{\mathrm{d}\Omega} \cong \frac{\mathrm{d}\Sigma_M}{\mathrm{d}\Omega}(q_y, q_z)$, whereas $\frac{\mathrm{d}\Sigma_M}{\mathrm{d}\Omega} \cong \frac{\mathrm{d}\Sigma_M}{\mathrm{d}\Omega}(q_x, q_y)$ for $\mathbf{k}_0 \parallel \mathbf{H}_0$ ($q_z \cong 0$). In the discussion below, we will also study (for $\mathbf{k}_0 \perp \mathbf{H}_0$) the case of anisotropic two-dimensional correlations by considering the following expression for $c(y,z)$ [98]:

$$c(y,z) = \frac{\int\limits_{-\infty}^{+\infty}\int\limits_{-\infty}^{+\infty} \frac{\mathrm{d}\Sigma_M}{\mathrm{d}\Omega}(q_y, q_z)\cos(q_y y + q_z z)\,\mathrm{d}q_y\,\mathrm{d}q_z}{\int\limits_{-\infty}^{+\infty}\int\limits_{-\infty}^{+\infty} \frac{\mathrm{d}\Sigma_M}{\mathrm{d}\Omega}(q_y, q_z)\,\mathrm{d}q_y\,\mathrm{d}q_z}. \tag{2.97}$$

Due to the fact that $\frac{\mathrm{d}\Sigma_M}{\mathrm{d}\Omega} = \frac{\mathrm{d}\Sigma_M}{\mathrm{d}\Omega}(q_y, q_z)$, the $c(y,z)$ that is computed according to Eq. (2.97) represents a projection (average) of the three-dimensional correlation function $c(x,y,z)$ along the direction of the incident neutron beam [18, 19]

Equation (2.97) can be transformed into polar coordinates, which results in:

$$c(r,\phi) = \frac{\int\limits_{0}^{\infty}\int\limits_{0}^{2\pi} \frac{\mathrm{d}\Sigma_M}{\mathrm{d}\Omega}(q,\theta)\cos\left(qr\cos(\theta-\phi)\right) q d\theta\,\mathrm{d}q}{\int\limits_{0}^{\infty}\int\limits_{0}^{2\pi} \frac{\mathrm{d}\Sigma_M}{\mathrm{d}\Omega}(q,\theta) q d\theta\,\mathrm{d}q}, \tag{2.98}$$

where the angle ϕ specifies the orientation of $\mathbf{r} = (r,\phi)$ in the y-z-plane. By introducing the nth-order Bessel function [99],

$$J_n(z) = \frac{1}{2\pi}\int\limits_{0}^{2\pi} \cos(n\alpha - z\sin\alpha)\, d\alpha = \frac{1}{2\pi}\int\limits_{\delta}^{2\pi+\delta} \cos(n\alpha - z\sin\alpha)\, d\alpha, \tag{2.99}$$

where n is an integer and the last equation is valid for any angle δ, we can obtain an average of $c(r,\phi)$ over all angles ϕ in the detector plane:

$$c(r) = \frac{1}{2\pi}\int_0^{2\pi} c(r,\phi)\,d\phi = \frac{\int\limits_0^{\infty}\int\limits_0^{2\pi} \frac{\mathrm{d}\Sigma_M}{\mathrm{d}\Omega}(q,\theta)\,J_0(qr)\,q\,d\theta\;\mathrm{d}q}{\int\limits_0^{\infty}\int\limits_0^{2\pi} \frac{\mathrm{d}\Sigma_M}{\mathrm{d}\Omega}(q,\theta)\,q\,d\theta\;\mathrm{d}q}. \tag{2.100}$$

Since the integration with respect to the angle θ can be taken analytically (compare arguments leading to Eqs. (2.71) and (2.72)), it follows:

$$c(r) = \frac{\int\limits_0^{\infty} \frac{\mathrm{d}\Sigma_M}{\mathrm{d}\Omega}(q)\,J_0(qr)\,q\;\mathrm{d}q}{\int\limits_0^{\infty} \frac{\mathrm{d}\Sigma_M}{\mathrm{d}\Omega}(q)\,q\;\mathrm{d}q}. \tag{2.101}$$

Equation (2.101) is called the *averaged* “two-dimensional” correlation function of the spin-misalignment SANS cross section. Note that this expression differs from Eq. (2.96) which is obtained after three-dimensional integration of the θ-averaged $\mathrm{d}\Sigma_M/\mathrm{d}\Omega$.

It must be emphasized that correlation functions defined as Eq. (2.96) and as Eq. (2.101) are clearly different quantities: first is obtained from “complete” 3-dimensional Fourier transform and therefore require the knowledge of cross section in the whole 3D space, while the second one is defined for the cross sections obtained only in-plane (*i.e.* in the plane of detector as in real SANS experiment) and therefore is actually not “complete” Fourier transform of the cross section. Numerical calculations were done in order to compare these two correlation functions [76]. A possible case when these correlation functions can provide the same result is when the cross section is a function of only two coordinates.

2.3.3 Correlation function of the spin-misalignment SANS within micromagnetic approach

The following materials parameters were used in the calculations: saturation magnetization $\mu_0 M_s = 1.5\,\mathrm{T}$, exchange-stiffness constant $A = 2.5\times10^{-11}\,\mathrm{J/m}$, and $R = 5\,\mathrm{nm}$ for the particle radius in the sphere form factor $P(q)$ (Eq. (2.84)).

One-dimensional correlation functions

All results in this section are obtained by numerical integration of Eq. (2.96). In the first set of calculations, we concentrate on the dependence of the correlation functions on the applied

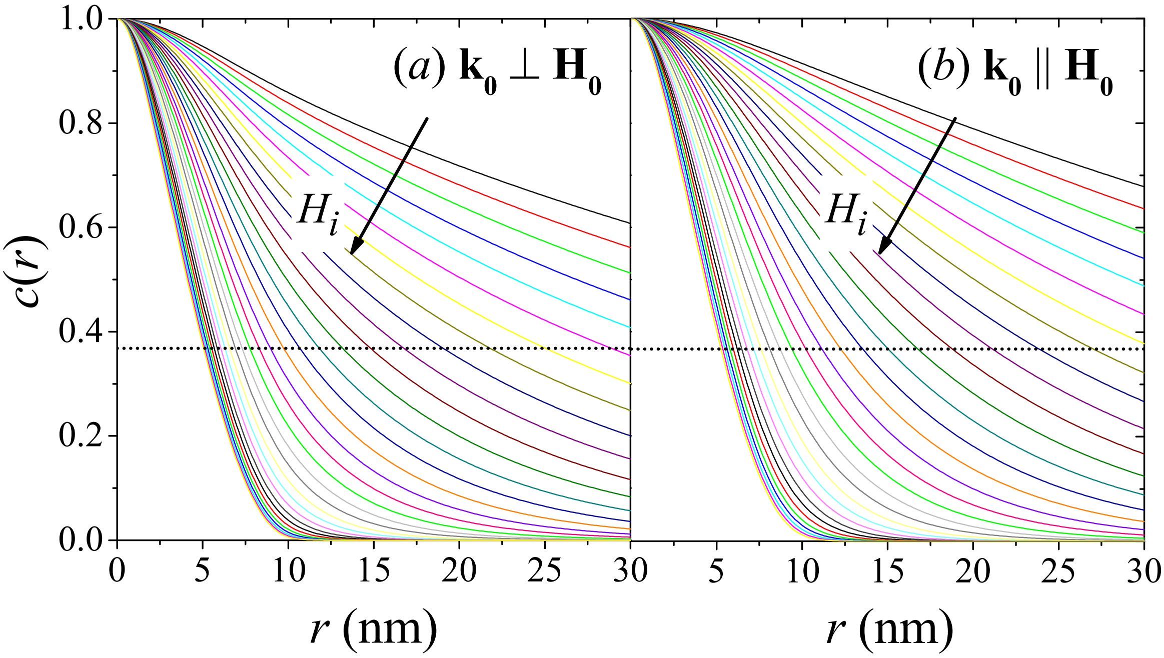

Fig. 2.5 Normalized correlation functions $c(r)$ of the spin-misalignment SANS cross section at several applied-field values H_i for (a) $\mathbf{k}_0 \perp \mathbf{H}_0$ and (b) $\mathbf{k}_0 \parallel \mathbf{H}_0$. H_i increases, respectively, from 0.01 T to 100 T on a logarithmic scale, *i.e.* $\mu_0 H_i^j = 10^{4\frac{j}{j_{\max}}-2}\,\mathrm{T}$, where $j_{\max} = 30$ and $j = 0,...,30$ ($S(q) = 1$; $H_p/\Delta M = 1$); the arrows specify the direction of increasing H_i. Dotted horizontal lines in (a) and (b): $c(r) = \exp(-1)$.

magnetic field H_i, scattering geometry ($\mathbf{k}_0 \perp \mathbf{H}_0$ and $\mathbf{k}_0 \parallel \mathbf{H}_0$), ratio $H_p/\Delta M$, single-particle form factor $P(q)$, and structure factor $S(q)$.

Fig. 2.5 displays the results for $c(r)$ at several values of H_i and for both scattering geometries, assuming a dilute scattering system (*i.e.* $S(q) = 1$) and $H_p/\Delta M = 1$. The dotted horizontal lines indicate the value of the correlation length l_C of the spin misalignment, which can be taken as a measure for the size of inhomogeneously magnetized regions around defects; l_C is *defined* as the $\exp(-1)$ decay-length, *i.e.* $c(r = l_C) = \exp(-1)$. However, this definition does not imply that the correlations decay exponentially. In fact, it is readily verified that the spin-misalignment correlations which are investigated in this study do not decay exponentially. We would also like to mention that an alternative route to extracting a spin-misalignment length may be realized by the computation of moments of the correlation function; for instance, for exponentially decaying $c(r)$ the above definition and $l_C = \int_0^\infty c(r)dr$ are equivalent.

Increasing H_i results in both scattering geometries in the suppression of transversal spin-misalignment fluctuations and in a concomitant reduction of the $c(r)$ and reduced l_C-values. At small fields, l_C may take on values of the order of 100 nm, which decrease to values of

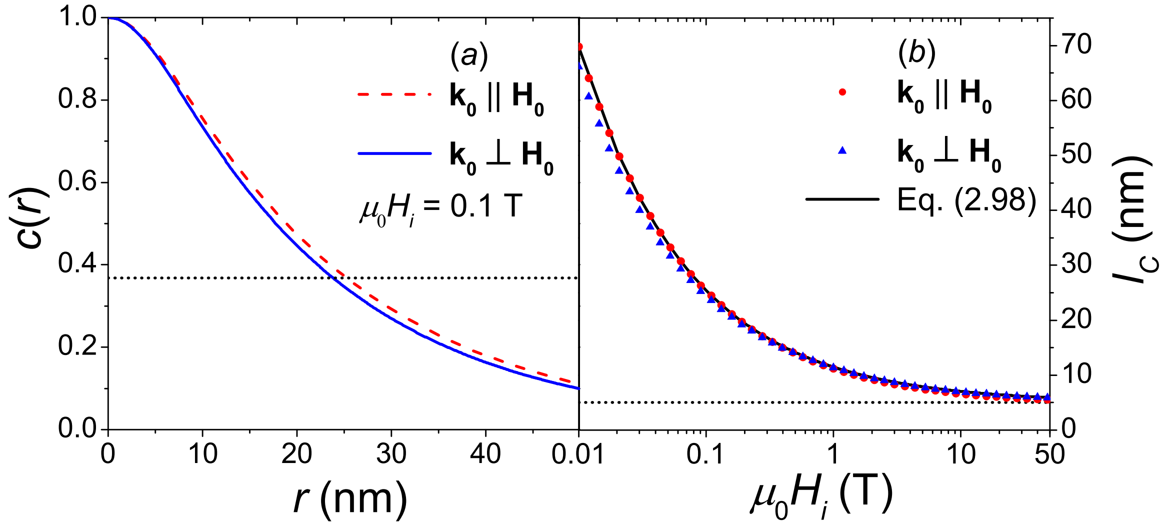

Fig. 2.6 (a) Comparison of the $c(r)$ for the two scattering geometries ($\mu_0 H_i = 0.1\,\mathrm{T}$; $S(q) = 1$; $H_p/\Delta M \rightarrow \infty$). Dotted horizontal line: $c(r) = \exp(-1)$. (b) Comparison of the field dependence of the spin-misalignment correlation length l_C for the two scattering geometries ($S(q) = 1$; $H_p/\Delta M \rightarrow \infty$) (log-lin scale). Solid line: Eq. (2.104). Dotted horizontal line: $l_C = R = 5\,\mathrm{nm}$.

the order of the assumed particle size, here $R = 5\,\mathrm{nm}$, for fields larger than a few Tesla (see also dotted horizontal line in Fig. 2.6b). For the chosen limiting case of $H_p/\Delta M \rightarrow \infty$, the difference between the $c(r)$ and the $l_C(H_i)$ in the two scattering geometries is only minor (see Fig. 2.6). However, noting that $c(r)$ in the parallel geometry is independent of $H_p/\Delta M$ and with reference to Figs. 2.7 and 2.8, we note that this difference increases with decreasing value of $H_p/\Delta M$.

Within the framework of our micromagnetic SANS theory of bulk ferromagnets [25, 74], the magnetic microstructure in real space, $\mathbf{M}(\mathbf{r})$, corresponds to a complicated convolution product between the magnetic anisotropy-field microstructure and micromagnetic functions. As a result, smoothly-varying magnetization profiles are at the origin of the related spin-misalignment scattering. In agreement with the absence of a sharp interface in the *magnetic* microstructure (compare Fig. 2.1b), we note that the correlation functions of bulk ferromagnets enter the origin $r = 0$ with zero slopes [100], so that

$$c(r) = 1 + kr^2 + \ldots \tag{2.102}$$

for $r \ll 1$ (where k is a constant). This observation may be compared to the well-known result for nuclear particle scattering, where (for isolated uniform particles) the first derivative of $c(r)$ evaluated at $r = 0$ is related to the particle surface. In particular, for small r, the

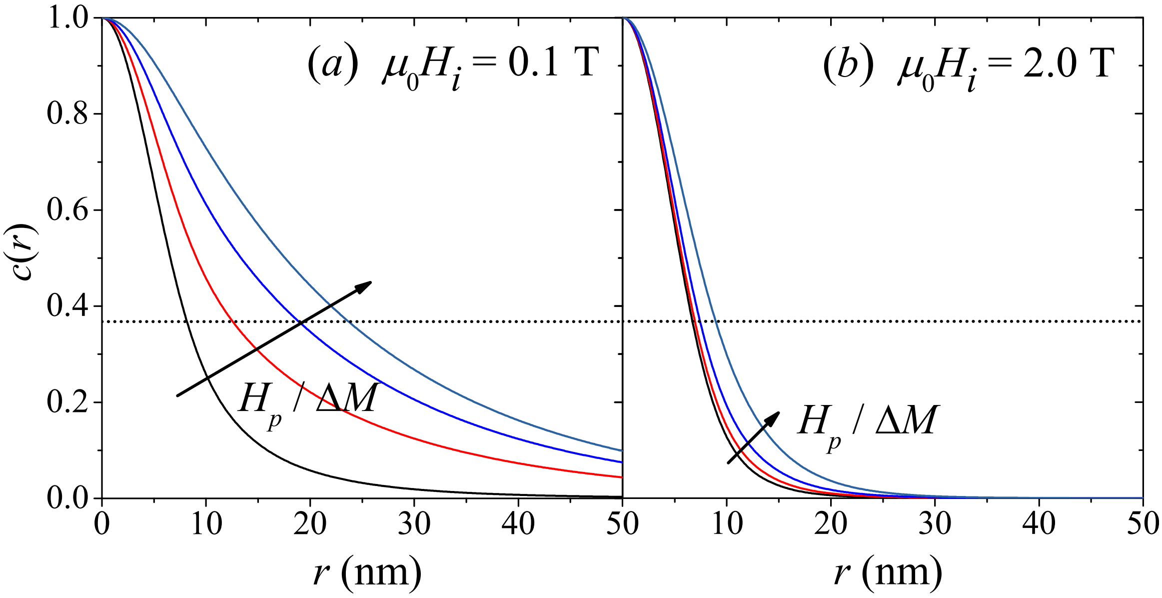

Fig. 2.7 $c(r)$ for several values of the ratio $H_p/\Delta M$ at (a) $\mu_0 H_i = 0.1\,\mathrm{T}$ and (b) $\mu_0 H_i = 2.0\,\mathrm{T}$ ($\mathbf{k}_0 \perp \mathbf{H}_0$; $S(q) = 1$). $H_p/\Delta M$ values: 0.004, 0.4, 0.8, 4; the arrows specify the direction of increasing $H_p/\Delta M$; for larger values of $H_p/\Delta M$, $c(r)$ remains effectively unchanged. Dotted horizontal lines in (a) and (b): $c(r) = \exp(-1)$.

correlation function can be expanded as [92]

$$c(r) = 1 + ar + br^2 + cr^3 + ..., \tag{2.103}$$

where the 'differential' parameters a, b, c are related to the size and shape of the particle; for example, for a uniform sphere one finds $a = -3/(4R)$, $b = 0$, and $c = 1/(16R^3)$.

The effect of the ratio $H_p/\Delta M$ on the correlation functions and on the l_C-values is shown in Figs. 2.7 and 2.8 (for $\mathbf{k}_0 \perp \mathbf{H}_0$ and $S(q) = 1$). Perturbations in the spin microstructure which are dominated by fluctuations of the magnetic anisotropy field ($H_p/\Delta M \gg 1$) decay on a larger length scale than magnetostatically dominated ($H_p/\Delta M \ll 1$) perturbations.

For soft magnets (with low crystalline anisotropy), the following relation for $l_C(H_i)$ has previously been suggested [13],

$$l_C(H_i) = R + l_H(H_i) = R + \sqrt{\frac{2A}{\mu_0 M_s H_i}}. \tag{2.104}$$

Equation (2.104) provides an excellent description of the field-dependent correlations (solid lines in Figs. 2.6b and 2.8 with $R = 5\,\mathrm{nm}$, $A = 2.5 \times 10^{-11}\,\mathrm{J/m}$, and $\mu_0 M_s = 1.5\,\mathrm{T}$). At large fields, when the spin-misalignment SANS cross section is small and the exchange length l_H

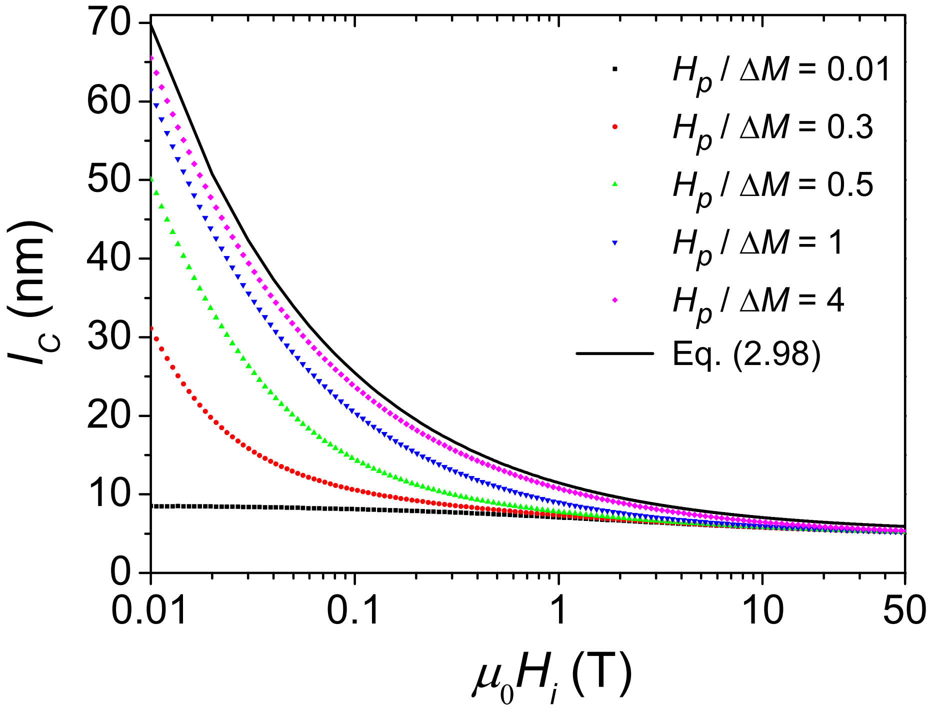

Fig. 2.8 Field dependence of the spin-misalignment correlation length l_C for different values of $H_p/\Delta M$ ($\mathbf{k}_0 \perp \mathbf{H}_0$; $S(q) = 1$) (log-lin scale). Solid line: Eq. (2.104).

takes on values of a few nanometers, l_C reflects, irrespective of $H_p/\Delta M$, the size of the (in this case spherical) defect.

For the perpendicular scattering geometry, Fig. 2.9 displays (for $\mu_0 H_i = 0.5\,\mathrm{T}$) the correlation function for different single-particle form factors $P(q)$, ignoring interparticle interactions ($S(q) = 1$). In addition to the sphere form factor (Eq. (2.84)), we have used in the expressions for $\widetilde{H}_p^2(q)$ and $\widetilde{M}_z^2(q)$ the cylinder form factor (radius: R; length: L) [89],

$$P(q) = \int_0^{\pi/2} \left[\frac{2J_1(qR\sin\alpha)}{qR\sin\alpha} \frac{\sin(\frac{1}{2}qL\cos\alpha)}{\frac{1}{2}qL\cos\alpha} \right]^2 \sin\alpha\, d\alpha, \tag{2.105}$$

and the form factor of an ellipsoid of revolution (semi-axes: $R, R, \varepsilon R$),

$$P(q) = \int_0^{\pi/2} 9 \left[\frac{j_1(qr(R,\varepsilon,\alpha))}{qr(R,\varepsilon,\alpha)} \right]^2 \sin\alpha\, d\alpha; \tag{2.106}$$

$J_1(x)$ denotes the first-order Bessel function, $j_1(x)$ is the first-order spherical Bessel function, and $r(R,\varepsilon,\alpha) = R(\sin^2\alpha + \varepsilon^2\cos^2\alpha)^{1/2}$; note that Eq. (2.106) reduces to the sphere form

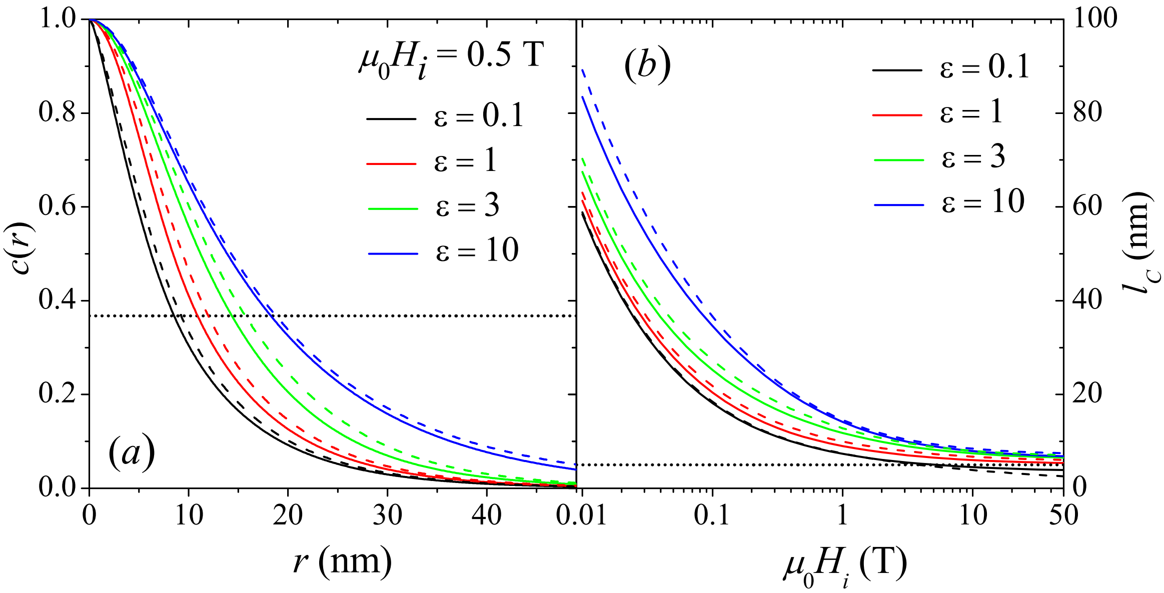

Fig. 2.9 Effect of particle form factor on the correlation function and correlation length. (*a*) $c(r)$ at $\mu_0 H_i = 0.5\,\mathrm{T}$ and for several particle form factors. Solid lines: form factor of ellipsoid of revolution ($R = 5\,\mathrm{nm}$) with ε decreasing from top to bottom ($\varepsilon = 1$ corresponds to the sphere form factor). Dashed lines: cylinder form factor with $R = 5\,\mathrm{nm}$ and $L = 2\varepsilon R$ ($\mathbf{k}_0 \perp \mathbf{H}_0$; $H_p/\Delta M = 1$; $S(q) = 1$). Dotted horizontal line: $c(r) = \exp(-1)$. (*b*) Corresponding $l_C(H_i)$ (log-lin scale). Dotted horizontal line: $l_C = R = 5\,\mathrm{nm}$.

factor for $\varepsilon = 1$. Besides the cylinder and ellipsoid of revolution form factor, we have also used other form factors (data not shown); the above form factors were chosen because they allow one to investigate different limiting cases (from thin circular discs to elongated spheroids and elongated thin rods). Examples of bulk magnetic materials with elongated cylindrically or elliptically-shaped precipitates are Alnico magnets [101], which are nanostructured alloys composed of Fe, Al, Ni, and Co.

It is seen in Fig. 2.9 that for a given form factor the shape of the correlation function and the value of the correlation length depend (as expected) on the particle dimensions. Isotropically distributed cylinders (dashed lines) with a radius equal to the radius of the ellipsoid of revolution and a length $L = 2\varepsilon R$ result in nearly the same (slightly larger) correlation functions as the ellipsoid of revolution; l_C at large fields appears to be related to the smallest dimension of the particle, although the precise dependency of $l_C(H_i \to \infty)$ on the particle dimensions is not clear to us. Note also that for the case of very thin discs and oblate spheroids ($\varepsilon \ll 1$), the correlation function still approaches the origin with zero slope (which becomes visible only for small r).

Finally, Fig. 2.10 illustrates the effect of interparticle interactions on the correlation function (Fig. 2.10*a*) and correlation length (Fig. 2.10*b*). In order to model the effect of

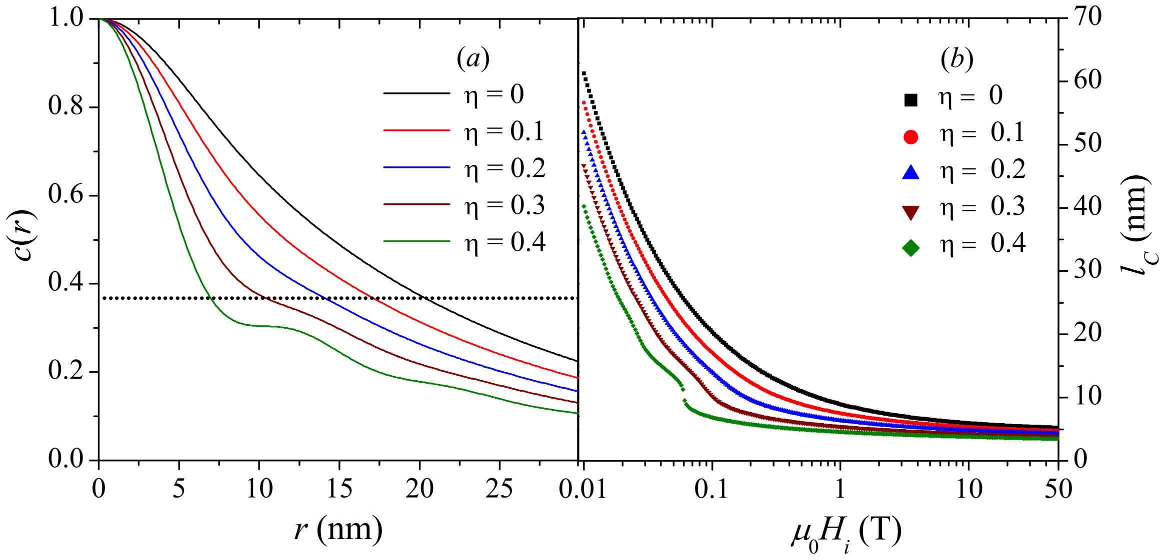

Fig. 2.10 Effect of hard-sphere volume fraction η on the correlation function and correlation length. (*a*) $c(r)$ at $\mu_0 H_i = 0.1\,\mathrm{T}$ and for several values of η increasing from top to bottom ($\mathbf{k}_0 \perp \mathbf{H}_0$; $H_p/\Delta M = 1$). Dotted horizontal line: $c(r) = \exp(-1)$. (*b*) Corresponding $l_C(H_i)$ (log-lin scale).

dense packing, we have used the Percus-Yevick hard-sphere structure factor for $S(q)$ [90] in Eqs. (2.82) and (2.83), and, as before, the sphere form factor for $P(q)$. Note also that the hard-sphere interaction radius R_{HS} in $S(q)$ was set equal to the sphere radius R.

It is clearly seen that with increasing particle volume fraction η the range of the correlations decreases. However, the characteristic features of the structure factor become only visible at relatively large values of η (above about 20%), while at the lower end of η-values both $c(r)$ and $l_C(H_i)$ are smoothly decaying functions. Furthermore, we note that with increasing η, *i.e.* with increasing interparticle interactions, we progressively introduce — in addition to the original (diffuse) spin-misalignment length l_C — a second *structural* correlation length into the system (compare the hump in l_C at around 50 mT for $\eta = 0.4$).

The field dependence of this feature is depicted in Fig. 2.11, where we show $c(r)$ for several H_i and for $\eta = 0.4$; here, we see that slight changes in H_i result in relatively large jumps in l_C ($l_C(0.08\,\mathrm{T}) = 7.7\,\mathrm{nm}$ and $l_C(0.05\,\mathrm{T}) = 13.8\,\mathrm{nm}$). This is an artifact which is clearly related to the strong structural correlations, and the determined correlation length now represents a field-dependent (unknown) average over the structural and the magnetic spin-misalignment correlation lengths. We note that by using other definitions for l_C, for instance in terms of some integral weight over $c(r)$, the position of the artifact on the H_i axis may be different but the effect of $S(q)$ will still become visible.

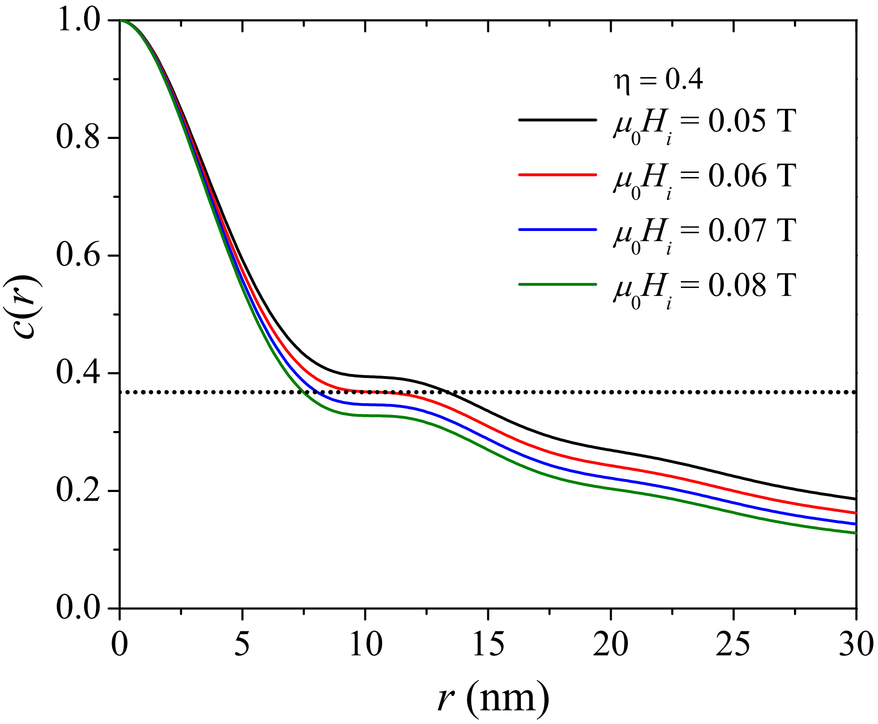

Fig. 2.11 $c(r)$ for $\eta = 0.4$ and for several values of the applied magnetic field H_i increasing from top to bottom ($\mathbf{k}_0 \perp \mathbf{H}_0$; $H_p/\Delta M = 1$). Dotted horizontal line: $c(r) = \exp(-1)$.

Two-dimensional correlation functions

Since the spin-misalignment SANS cross section is highly anisotropic for $\mathbf{k}_0 \perp \mathbf{H}_0$, the corresponding correlation function may also be anisotropic. We re-emphasize that the angular θ-dependence of $d\Sigma_M/d\Omega$ is a consequence of the trigonometric functions in the cross section (which are due to the dipolar neutron-magnetic interaction) and of the θ-dependence of the magnetization Fourier coefficients $\widetilde{M}_{x,y,z}(q,\theta)$ (which is due to the internal magnetostatic interaction) [13]. Fig. 2.12*a*-*d* shows $d\Sigma_M/d\Omega$ calculated from Eq. (2.64) at selected applied magnetic fields (and for $S(q) = 1$); the change in the angular anisotropy that becomes visible in Fig. 2.12*a*-*d*, from a spike-type anisotropy at low fields (*a*) to a cloverleaf-shaped anisotropy at large fields (*d*), is related to the field dependence of the Fourier coefficients and manifests that different terms in the response functions (Eqs. (2.71) and (2.72)) dominate in different field regimes. For instance, the spike anisotropy (Fig. 2.12*a*) was recently observed in an isotropic sintered Nd-Fe-B magnet [102]; it is related to magnetostatic terms $p \sin^2\theta$ in the denominator of the response functions.

The corresponding two-dimensional correlation functions, computed according to Eq. (2.97), are displayed in Fig. 2.12*e*-*h*, where we plot the $c(y,z)$ at the same fields as the $d\Sigma_M/d\Omega$. While the spin-misalignment SANS cross section at small fields (Figs. 2.12*a* and *b*) is

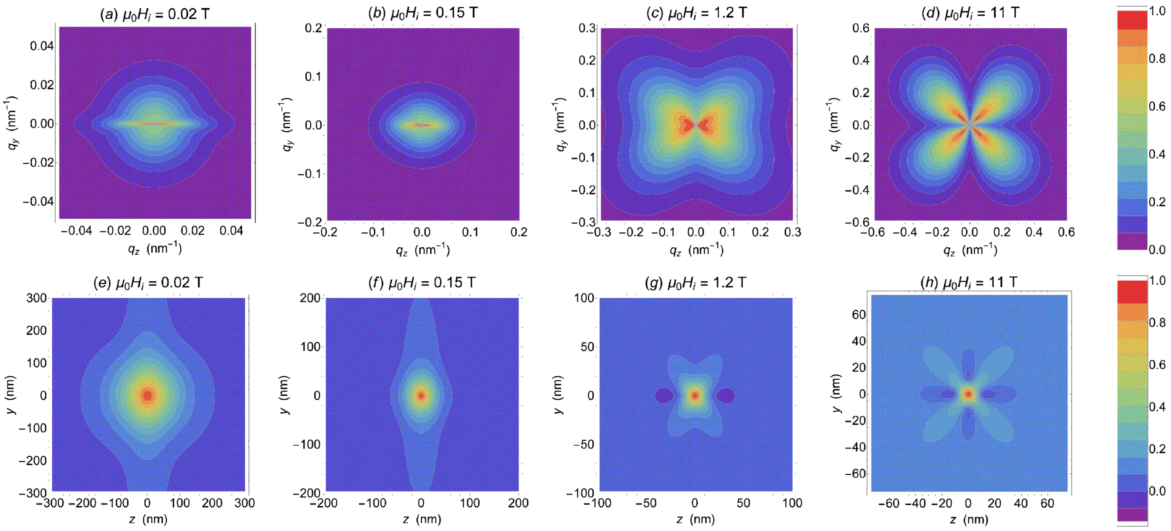

Fig. 2.12 (upper row) (*a*)-(*d*) Contour plots of normalized $\mathrm{d}\Sigma_M/\mathrm{d}\Omega$ (Eq. (2.64)) at applied magnetic fields as indicated ($\mathbf{k}_0 \perp \mathbf{H}_0$; $H_p/\Delta M = 1$; $\mathbf{H}_0$ is horizontal). For $\widetilde{H}_p^2$ and $\widetilde{M}_z^2$, we used the form factor of the sphere with a radius of $R = 5\,\mathrm{nm}$ (Eq. (2.84); $S(q) = 1$). (lower row) (*e*)-(*h*) Corresponding two-dimensional correlation functions $c(y,z)$, which were computed according to Eq. (2.97) ($H_p/\Delta M = 1$).

enhanced parallel to the applied-field direction, the correlation function exhibits maxima in the direction perpendicular to the field; the range of the correlations extends to several hundreds of nanometers (Figs. 2.12*e* and *f*). Increasing the field results in the suppression of the correlations and at the largest field $\mathrm{d}\Sigma_M/\mathrm{d}\Omega$ possesses a nearly fourfold anisotropy with maxima along the detector diagonals and minima along the horizontal and vertical axes (Fig. 2.12*d*), which translate into the corresponding extrema in $c(y,z)$ (Fig. 2.12*h*).

In Fig. 2.13*a*, we depict the correlation function along different directions: while the correlation length at 1.2 T varies only relatively little with direction (from 8.8 nm to 10.9 nm), the functional dependencies of the $c(y,z)$ are significantly different, with the correlation function along the horizontal z-direction becoming negative at $r \cong 18\,\mathrm{nm}$; the curves in Fig. 2.13*a* were obtained by solving Eq. (2.98) for $\phi = 0, \pi/4, \pi/2$. In nuclear SANS, negative values of the distance distribution function $p(r)$ are attributed to distances that connect regions with opposite sign of the scattering-length density more frequently than regions with the same sign [103]. However, for magnetic SANS, such an easily accessible interpretation of the correlation function $c(r)$ of the spin-misalignment SANS cross section in terms of a specific magnetization distribution is not straightforward; this is mainly related to the (above mentioned) fact that $c(r)$ does not directly represent the correlations in the magnetic microstructure (as does C_{SM}), but also includes the magnetodipolar interaction of the neutrons with the sample (via the trigonometric functions and the cross term in the cross

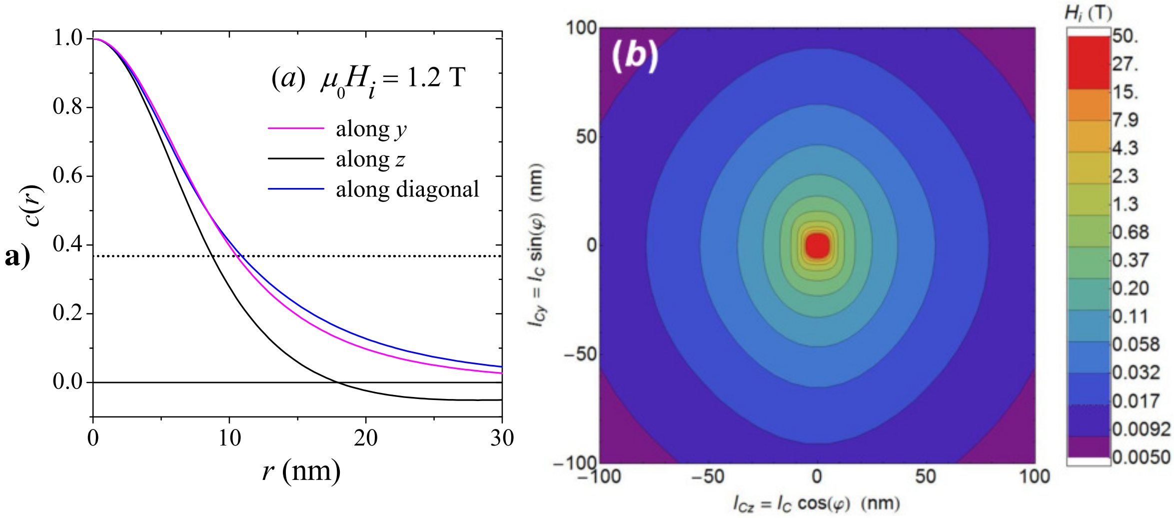

Fig. 2.13 (a) $c(r)$ along different real-space directions (same parameters as in Fig. 2.12g). Dotted horizontal line: $c(r) = \exp(-1)$. (b) Contour plot revealing the in-plane (ϕ) variation of l_C for several values of the applied magnetic field H_i. Logarithmic color scale for the field is used.

section). The anisotropy of the correlations is further depicted in Fig. 2.13b, where we show a contour plot for several values of H_i. This graph reveals a relatively weak anisotropy of l_C; at small fields, the correlations along the vertical (y) direction decay on a larger length scale than along the horizontal (z) direction; with increasing field, the anisotropy becomes less pronounced.

Figure 2.14 compares (for $\mathbf{k}_0 \perp \mathbf{H}_0$) the results for the one-dimensional (Eq. (2.96)) and the averaged two-dimensional (Eq. (2.101)) correlation functions of the spin-misalignment SANS. We remind that the former is obtained by three-dimensional integration of the azimuthally-averaged $\frac{d\Sigma_M}{d\Omega} = \frac{d\Sigma_M}{d\Omega}(q)$, whereas the latter by two-dimensional integration of $\frac{d\Sigma_M}{d\Omega} = \frac{d\Sigma_M}{d\Omega}(q,\theta)$ (compare Section 2.3.2). At small fields, the results for the $c(r)$ and $l_C(H_i)$ differ considerably, whereas for $\mu_0 H_i > 1\,\mathrm{T}$ both equations yield almost the same correlation lengths.

The question may arise which one of these correlation functions shall be used in order to analyze experimental data. From an experimental point of view, the averaged two-dimensional Eq. (2.101) reflects the data-analysis procedure, namely that the measured $d\Sigma_M/d\Omega$ is a function of only two independent components of the scattering vector. In fact, elastic scattering in small-angle approximation only probes correlations in the directions perpendicular to the incident beam. Reconstruction (from experimental $d\Sigma_M/d\Omega$) of the one-dimensional $c(r)$ (which is an orientation average of the three-dimensional correlation function) is always an extrapolation.

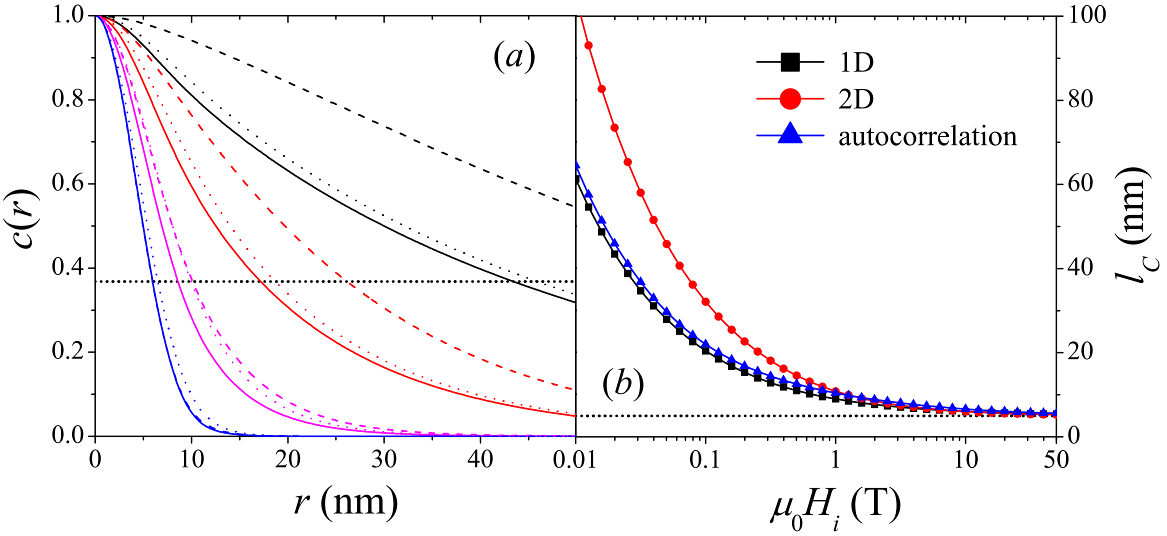

Fig. 2.14 (*a*) Comparison between the one-dimensional (Eq. (2.96); solid lines) and the averaged two-dimensional (Eq. (2.101); dashed lines) correlation functions of the spin-misalignment SANS cross section and the autocorrelation function of the spin misalignment (dotted lines) ($\mathbf{k}_0 \perp \mathbf{H}_0$; $H_p/\Delta M = 1$; $S(q) = 1$). $c(r)$ at selected H_i; values of H_i (in T) increasing from top to bottom: 0.02, 0.15, 1.2, 11. Dotted horizontal line: $c(r) = \exp(-1)$. (*b*) Corresponding $l_C(H_i)$ (log-lin scale) (lines are guide to the eyes). Dotted horizontal line: $l_C = R = 5\,\mathrm{nm}$.

Comparison to experimental data

In order to test our magnetic SANS theory, we depict in Fig. 2.15 a comparison between experiment and theory; in particular, we have fitted Eqs. (2.96) and (2.101) (using Eq. (2.81) for $d\Sigma_M/d\Omega$) to experimental data for the correlation function of the spin-misalignment SANS cross section of nanocrystalline Co and Ni [94]. These $C(r)$ data have previously been analyzed in [104] using a simple approach based on the autocorrelation function of the spin misalignment, neglecting terms due to spatial fluctuations of the saturation magnetization. Such contributions are included in the present theory via the term $S_M R_M$ in Eq. (2.81). The nanocrystalline Co and Ni samples constitute fully dense polycrystalline metals with average crystallite sizes of $D = 10\,\mathrm{nm}$ (Co) and $D = 49\,\mathrm{nm}$ (Ni) [75]. The experimental SANS data of both samples were recorded between $q_{\min} \cong 0.01\,\mathrm{nm}^{-1}$ and $q_{\max} \cong 1.0\,\mathrm{nm}^{-1}$. The correlation functions were then obtained by direct Fourier transformation according to Eq. (2.96), so that this expression should actually also be used for the data analysis. Nevertheless, we have also employed the two-dimensional Eq. (2.101) for fitting the experimental $C(r)$ data, which is motivated by the fact that for larger applied fields the difference between both correlation functions is only minor (compare Fig. 2.14). In the following discussion, one should keep

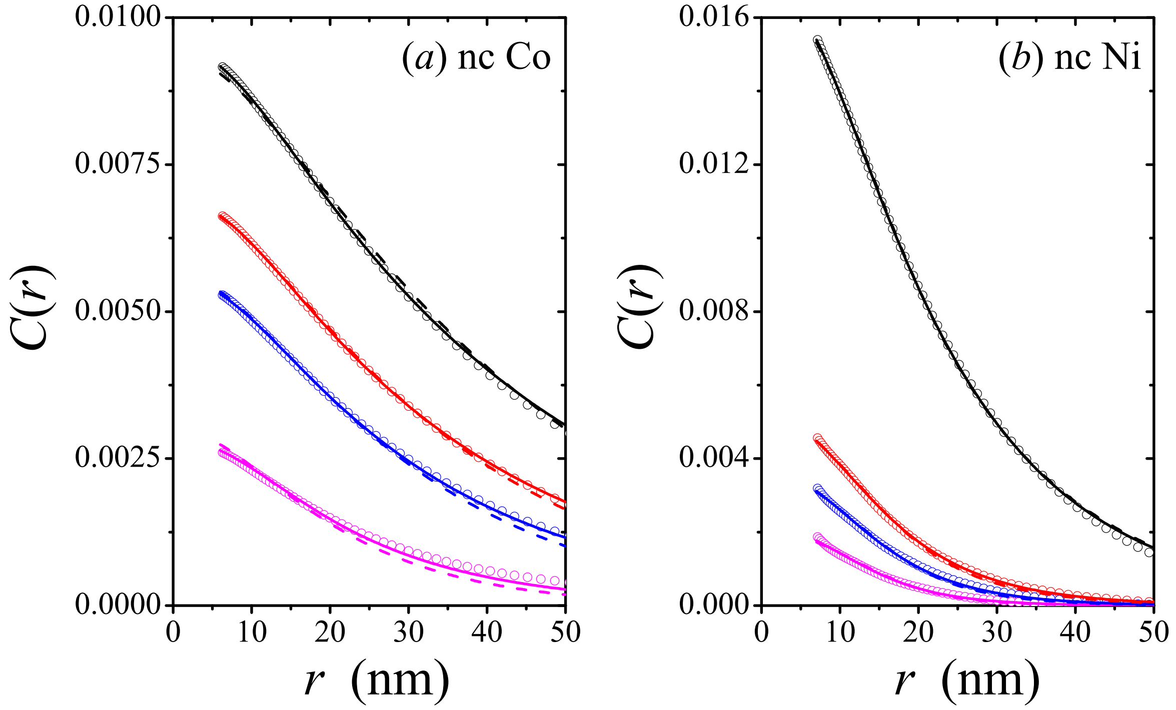

Fig. 2.15 Comparison between experimental and theoretical data. (○) Correlation functions of the spin-misalignment SANS cross section of (*a*) nanocrystalline Co and (*b*) nanocrystalline Ni with average crystallite sizes of $D = 10\,\mathrm{nm}$ (Co) and $D = 49\,\mathrm{nm}$ (Ni) [75]. $C(r)$ data are taken from [94]. Solid lines: fit based on Eq. (2.96); dashed lines: fit based on Eq. (2.101). Values of the internal magnetic field H_i (in mT) from top to bottom, respectively: (a) 54, 80, 107, 243; (b) 190, 570, 800, 1240. In both analyses, we have used the sphere form factor for $P(q)$ and $S(q) = 1$.

in mind that for the analysis of this particular $C(r)$ data, Eq. (2.96) represents the proper theoretical model.

In the fitting procedure, the integrals in Eqs. (2.96) and (2.101) were approximated by discrete sums, where the upper integration limit of '∞' was taken as $q_{\max} \cong 5 - 10\,\mathrm{nm}^{-1}$ and the typical q-resolution was set to $\Delta q \cong 0.01 - 0.02\,\mathrm{nm}^{-1}$. The resulting expressions were fitted by means of a nonlinear (Levenberg-Marquardt) fitting routine to the experimental $C(r)$ data. We have treated the exchange-stiffness constant A, the ratio $H_p/\Delta M$, and R as *global* fit parameters. Since we work with unnormalized $C(r)$ data, we have introduced field-dependent *local* scaling constants K_1, K_2, K_3, and K_4 (one for each data set); $M_s = 1434\,\mathrm{kA/m}$ for Co and $M_s = 522\,\mathrm{kA/m}$ for Ni were held constant; since the experimental SANS data (*e.g.* Fig. 1 in [94]) do not give a visible indication for a strong impact of dense packing, we have for simplicity decided to set $S(q) = 1$. The results for the global fit parameters are summarized

Table 2.2 Results for the global fit parameters A, $H_p/\Delta M$, and R obtained by fitting Eqs. (2.96) and (2.101) to the correlation functions of nanocrystalline Co and Ni displayed in Fig. 2.15.

	Co [Eq. (2.96)]	Co [Eq. (2.101)]	Ni [Eq. (2.96)]	Ni [Eq. (2.101)]
A (pJ m^{-1})	54.6 ± 0.6	29.1 ± 0.6	15.1 ± 0.1	13.7 ± 0.4
$H_p/\Delta M$	13.4 ± 0.0	4.0 ± 0.1	5.6 ± 0.0	0.5 ± 0.1
R (nm)	10.2 ± 0.1	8.2 ± 0.6	9.9 ± 0.1	13.0 ± 0.1

in Table 1. The data analysis was restricted to r-values below about 50 nm and to fields larger than 50 mT, where the magnetization of both samples approaches saturation [75].

As is seen in Fig. 2.15 (solid and dashed lines), both equations provide a reasonable global description of the field-dependent correlations. The obtained values for the anisotropy-field radii R of both materials are in the range between $8 - 13\,\mathrm{nm}$, slightly smaller than the ones estimated previously [104]. The parameter R characterizes the length scale over which the magnetic anisotropy field $\mathbf{H}_p(\mathbf{r})$ is uniform; for single-crystal grains, R is sensibly related to the average crystallite size (compare Fig. 2.1*a*). Therefore, the finding $R \cong 8 - 10\,\mathrm{nm}$ for Co suggests that the magnetic anisotropy field is approximately homogeneous on a length scale of the order of the average grain size of 10 nm, whereas for Ni nonuniformities in $\mathbf{H}_p(\mathbf{r})$ exist on a scale smaller than the average crystallite size of 49 nm, presumably related to twin faults or to the defect cores of grain boundaries [94]. While the obtained values for the exchange-stiffness constant of Ni (using both equations) are larger by a factor of about two than the ones reported in the literature [49], the A-value for Co using Eq. (2.101) agrees excellently with literature data and with the result of our previous SANS data analysis (in Fourier space) [94]. Values for the ratio of $H_p/\Delta M$ have not been determined previously for these materials, but our results suggest (except for the case of Ni using Eq. (2.101)) that perturbations in the spin microstructure due to spatially fluctuating magnetic anisotropy fields dominate over magnetostatic fluctuations; this might be expected, since in single-phase ferromagnets variations in M_s are relatively small, compared to *e.g.* nanocomposites [86]. Overall, the good agreement between experiment and theory suggests that Eq. (2.96) may be used for the analysis of real-space correlations of bulk magnetic materials. Equation (2.101) may also be employed for the analysis of experimental data, provided that the original $d\Sigma_M/d\Omega$ has been Fourier-transformed according to Eq. (2.101).

2.3.4 Calculation of the correlation function from the SANS experimental data

The results for correlation function presented in Chapter 4 were calculated by numerical integration of Eq. (2.97) using the trapezoidal rule [105].

$$\begin{aligned} C(y,z) &= \sum_{j=1}^{N_j} \left((q_{y_{j+1}} - q_{y_j}) \, \frac{\mathrm{I}_1(j+1) + \mathrm{I}_1(j)}{2} \right) \\ \mathrm{I}_1(j) &= \sum_{i=1}^{N_i} \left((q_{z_{i+1}} - q_{z_i}) \, \frac{\mathrm{I}_0(i+1,j) + \mathrm{I}_0(i,j)}{2} \right) \\ \mathrm{I}_0(i,j) &= \frac{\mathrm{d}\Sigma}{\mathrm{d}\Omega}(q_{y_i}, q_{z_i}) \, \cos(yq_{y_i} + zq_{z_i}). \end{aligned} \tag{2.107}$$

Since the values of $\mathrm{d}\Sigma/\mathrm{d}\Omega$ obtained from SANS experiment are always known in the limited q-range, the Fourier transform from Eq. (2.107) results in artificial oscillations with the frequency depending on $q_{\min}$ and $q_{\max}$. Limitation of the scattering data with $q_{\min}$ results in oscillations with relatively large frequency $\sim \frac{\pi}{q_{\min}}$, and limitation of the scattering data with $q_{\max}$ results in oscillations with relatively large frequency $\sim \frac{\pi}{q_{\max}}$. Moreover, the integral $\int_0^{q_{\min}} I(\mathbf{q}) e^{i\mathbf{qr}} \, \mathrm{d}\mathbf{q}$ definitely has a strong impact on the values of $c(r)$ since the intensity at low q is usually much larger than as at high q. Therefore, it is necessary to extrapolate the data to the $q_{\min} \to 0$ and $q_{\max} \to \infty$.

Low-q data were extrapolated with the assumption of a constant $\mathrm{d}\Sigma/\mathrm{d}\Omega$ for $q < q_{\min}$. This is a simplified case of the so-called Guinier extrapolation, which at $q \to 0$ reads

$$I(q) \sim e^{-\frac{q^2 R_G^2}{3}},$$

with R_G being a radius of gyration, which depends on the mean size of the particles R and on their shape. High-q data are usually extrapolated by power-law

$$I \sim q^n.$$

However, in the case for the experiment below, the spin-misalignment scattering cross sections tend to decrease to zero for q larger than a certain value of $0.1 - 10\,\mathrm{nm}^{-1}$, thus there was no need of high-q data extrapolation.

2.4 Influence of Dzyaloshinsky-Moriya interaction on the magnetic spin-misalignment SANS

The results presented in this section are the part of the actual PhD work and were published in [106].

The Dzyaloshinsky-Moriya (DM) interaction [27, 28] has recently become anew the focus of an intense worldwide research effort in condensed-matter physics. This interaction is due to relativistic spin-orbit coupling, and in low-symmetry crystal structures lacking inversion symmetry it gives rise to antisymmetric magnetic interactions. Particularly well-investigated classes of materials are ultrathin film nanostructures and noncentrosymmetric B20 transition-metal compounds (*e.g.*, MnSi, $\mathrm{Fe_{1-x}Co_xSi}$, or FeGe), where the DM interaction plays an important role for the formation of various kinds of inhomogeneous spin structures such as long-wavelength spirals, vortex states, and skyrmion textures (see, *e.g.*, Refs. [29–46] and references therein).

However, already in 1963, Arrott [47] pointed out that even in a high-symmetry lattice, where the antisymmetric DM term would normally vanish, this interaction is present in the vicinity of any lattice defect. Arrott argued that in antiferromagnetic crystals the DM interaction results in parasitic ferromagnetism, whereas in ferromagnets it gives rise to local antiferromagnetism (in this way reducing the spontaneous magnetization). Hence, based on these considerations, one may expect that the DM interaction substantially influences the magnetic microstructure of polycrystalline materials with a large defect density. In a sense, microstructural defects act as a source of additional local chiral interactions, similar to the above mentioned (intrinsic) DM interactions in noncentrosymmetric crystals.

One class of materials, where defects play a decisive role, are nanocrystalline magnets, which are characterized by an extremely large interface-to-volume ratio; note that the volume fraction of internal interfaces (*e.g.*, grain boundaries) scales as L^{-1}, where $L \sim 10-20\,\mathrm{nm}$ represents the average crystallite size. This implies that a significant amount of atoms ($\sim 10-20$ vol.%) in such magnets are localized in the near-vicinity of interfaces, where inversion symmetry is likely to be broken. Consequently, the magnetic properties of a polycrystalline magnet may be substantially influenced by the DM term once its average grain size "goes nano".

Thus, the DM interaction might reveal itself in magnets with many crystalline imperfections. Let us now address the question of how to measure an ensuing "effect". Traditionally, the influence of lattice defects on the magnetization of bulk magnetic materials is studied by analyzing the high-field branch of a hysteresis curve (see, *e.g.*, the classic studies by Brown and Kronmüller [48, 49, 26]). However, this approach suffers from the disadvantages that it provides only integral (and no spatially-resolved) information and that the result of such an analysis may depend on the range of applied-field values over which the magnetization data are analyzed. As we will see below, neutron scattering and, in particular, polarized small-angle neutron scattering (SANS) [50–56] provides an important means to investigate the relevance of the defect-induced DM interaction on a microscopic scale and inside the bulk of inhomogeneous magnets.

2.4.1 DM interaction energy contribution and balance of torques equation

The Dzyaloshinsky-Moriya (DM) interaction [27, 28] is due to relativistic spin-orbit coupling, and it gives rise to antisymmetric magnetic interactions in low-symmetry crystal structures which lacks inversion symmetry. In a general bulk statistically-isotropic ferromagnet, the influence of DM interaction is usually negligible. For expression of the energy term, we consider a phenomenological DM interaction energy term (for cubic crystal structures) [29–31]

$$E_{\mathrm{DM}} = \frac{D}{{M_s}^2} \int_V \mathrm{M} \cdot [\nabla \times \mathbf{M}]\, \mathrm{d}V, \tag{2.108}$$

where D (in units of $\mathrm{J/m^2}$) denotes an effective DM interaction constant taking on positive or negative values depending on the material.

We remind the reader that the energy of a ferromagnet should be considered as a functional of its magnetization: $E_{\mathrm{tot}} = E_{\mathrm{tot}}(\mathbf{M}(\mathbf{r}))$, and that the state of equilibrium magnetization configuration corresponds to a (local) energy minimum. Taking into account energy term from Eq. (2.108) and recalling Eq. (2.8), the new variance of E_{tot} reads

$$\delta E_{\mathrm{tot}} = \delta(E_{\mathrm{z}} + E_{\mathrm{ex}} + E_{\mathrm{mc}} + E_{\mathrm{me}} + E_{\mathrm{m}} + E_{\mathrm{DM}}) = 0. \tag{2.109}$$

In the same way as in Section 2.1, in order to find the expressions for the components of $\widetilde{\mathbf{M}}$, it is necessary to solve the so-called balance-of-torques equation (*cf.* Eq. (2.9)). The effective magnetic field (compare Eq. (2.10)), with now taking into account DM interaction, reads:

$$\mathbf{H}_{\mathrm{eff}} = -\frac{1}{\mu_0} \cdot \frac{\delta \omega}{\delta \mathbf{M}} = \mathbf{H}_0 + \mathbf{H}_{\mathrm{ex}} + \mathbf{H}_p + \mathbf{H}_d + \mathbf{H}_{\mathrm{DM}}, \tag{2.110}$$

where the field $\mathbf{H}_{\mathrm{DM}}$ corresponds to E_{DM}.

All the H_{eff} components were introduced in Section 2.1.2, except H_{DM}. The expression for the field due to the DM interaction is

$$\mathbf{H}_{DM} = -l_D\, [\nabla \times \mathbf{M}], \tag{2.111}$$

where $l_D = \frac{2D}{\mu_0 M_s^2}$ is the micromagnetic length scale of DM interaction. The corresponding Fourier transform is

$$\widetilde{\mathbf{H}}_{DM}(\mathbf{q}) = -i l_D \left[\mathbf{q} \times \widetilde{\mathbf{M}}\right]. \tag{2.112}$$

By using Eqs. (2.110, 2.112) in the balance-of-torque equation (*cf.* Eq. (2.9)) and by neglecting terms of higher than linear order in $\widetilde{M}_x$, $\widetilde{M}_y$, and $\widetilde{I}_m$ (including terms such as $\widetilde{M}_x \widetilde{I}_m$ and $\widetilde{H}_{p,x} \widetilde{I}_m$), we obtain, in Fourier space, and for a general orientation of the wavevector $\mathbf{q} = \left\{q_x, q_y, q_z\right\}$, the following set of linear equations for $\widetilde{M}_x$ and $\widetilde{M}_y$ [48]:

$$\widetilde{M}_x \left(1 + p\frac{q_x^2}{q^2}\right) + \widetilde{M}_y \left(p\frac{q_x q_y}{q^2} - i p\, l_D q_z\right) = p\left(\widetilde{H}_{p,x} - M_s \widetilde{I}_m \left[\frac{q_x q_z}{q^2} + i l_D q_y\right]\right), \tag{2.113}$$

$$\widetilde{M}_y \left(1 + p\frac{q_y^2}{q^2}\right) + \widetilde{M}_x \left(p\frac{q_x q_y}{q^2} + i p\, l_D q_z\right) = p\left(\widetilde{H}_{p,y} - M_s \widetilde{I}_m \left[\frac{q_y q_z}{q^2} - i l_D q_x\right]\right). \tag{2.114}$$

The solutions of Eqs. (2.113) and (2.114) are:

$$\widetilde{M}_x = \frac{p\left(\widetilde{H}_{p,x}\left[1 + p\frac{q_y^2}{q^2}\right] - M_s \widetilde{I}_m \frac{q_x q_z}{q^2}\left[1 + p\, l_D^2 q^2\right] - \widetilde{H}_{p,y} p \frac{q_x q_y}{q^2} - i\left[M_s \widetilde{I}_m (1+p) l_D q_y - \widetilde{H}_{p,y} p\, l_D q_z\right]\right)}{1 + p\frac{q_x^2 + q_y^2}{q^2} - p^2 l_D^2 q_z^2}, \tag{2.115}$$

$$\widetilde{M}_y = \frac{p\left(\widetilde{H}_{p,y}\left[1 + p\frac{q_x^2}{q^2}\right] - M_s \widetilde{I}_m \frac{q_y q_z}{q^2}\left[1 + p\, l_D^2 q^2\right] - \widetilde{H}_{p,x} p \frac{q_x q_y}{q^2} + i\left[M_s \widetilde{I}_m (1+p) l_D q_x - \widetilde{H}_{p,x} p\, l_D q_z\right]\right)}{1 + p\frac{q_x^2 + q_y^2}{q^2} - p^2 l_D^2 q_z^2}, \tag{2.116}$$

2.4.2 Influence of Dzyaloshinsky-Moriya interaction on magnetic spin-misalignment SANS

We remind the reader that the present discussions are concentrated on the perpendicular scattering geometry, which has the wavevector $\mathbf{k}_0$ of the incoming neutron beam perpendicular to the applied magnetic field $\mathbf{H}_0 \parallel \mathbf{e}_z$. In such geometry, the scattering or momentum-transfer vectors for these two geometries reduce to

$$\mathbf{q} \cong \left\{0, q_y, q_z\right\} = q\left\{0, \sin\theta, \cos\theta\right\}. \tag{2.117}$$

For $q_x = 0$ ($\mathbf{k}_0 \perp \mathbf{H}_0$), Eqs. (2.115) and (2.116) reduce to

$$\widetilde{M}_x = \frac{p\left(\widetilde{H}_{p,x}\left[1 + p\frac{q_y^2}{q^2}\right] - i\left[M_s \widetilde{I}_m (1+p) l_D q_y - \widetilde{H}_{p,y} p\, l_D q_z\right]\right)}{1 + p\frac{q_y^2}{q^2} - p^2 l_D^2 q_z^2}, \tag{2.118}$$

$$\widetilde{M}_y = \frac{p\left(\widetilde{H}_{p,y} - M_s\widetilde{I}_m\frac{q_yq_z}{q^2}\left[1+p\,l_D^2q^2\right] - i\widetilde{H}_{p,x}p\,l_Dq_z\right)}{1+p\frac{q_y^2}{q^2}-p^2l_D^2q_z^2}. \tag{2.119}$$

Several comments are in place: (i) We note that both Fourier components $\widetilde{M}_x(\mathbf{q})$ and $\widetilde{M}_y(\mathbf{q})$ are complex functions, which (at $q \neq 0$) depend explicitly on the longitudinal magnetization Fourier coefficient

$$\widetilde{M}_z(\mathbf{q}) = M_s\widetilde{I}_m(\mathbf{q}). \tag{2.120}$$

Since $\widetilde{M}_z \propto \Delta M$, [73] this term models inhomogeneities in the magnetic microstructure that are due to jumps ΔM in the magnetization at internal interfaces (*e.g.*, particle-matrix boundaries). Furthermore, the magnetic anisotropy field Fourier component $\widetilde{H}_p$ and $\widetilde{M}_z$ both exhibit a tendency to increase the amplitudes of the transversal Fourier coefficients and are, thus, the sources of spin disorder in the system (this is best seen by inspecting the averaged squared functions Eqs. (2.121)−(2.126) below). (ii) Terms in $\widetilde{M}_x$ and $\widetilde{M}_y$ such as q_y^2/q^2 or q_xq_y/q^2 are due to the long-range magnetodipolar interaction (compare to the above expression for $\widetilde{\mathbf{H}}_d(\mathbf{q})$). These contributions (in combination with terms related to the DM interaction) give rise to an angular anisotropy *already* in the Fourier components (see Figs. 2.16 and 2.17); this anisotropy (θ-dependence, see below) adds on top of the anisotropy that is related to the trigonometric functions originating from the dipolar neutron-magnetic interaction. (iii) The denominator of $\widetilde{M}_x$ and $\widetilde{M}_y$ has (for $\mathbf{k}_0 \perp \mathbf{H}_0$) a singularity for $1+pq_y^2/q^2 = p^2l_D^2q_z^2$, which becomes particularly noticeable at small fields and for small q along the horizontal direction ($\theta = 0$) where $q_y = 0$. For large q or large H_i, the effective magnetic field takes on large values, [83] so that $p \ll 1$ and the term $p^2l_D^2q_z^2$ is much smaller than $1+pq_y^2/q^2$. However, we remind that the present theory is valid in the approach-to-saturation regime when the sample consists of a single magnetic domain and one considers small deviations of magnetic moments (due to spatially varying H_p, M_s, and due to the DM interaction) relative to the applied field direction. Without the DM interaction ($l_D = 0$), Eqs. (2.118) and (2.119) reduce to Eqs. (2.65) and (2.66).

Now it is possible to evaluate the scattering cross sections by computing appropriate averages of functions such as $|\widetilde{M}_x|^2$, $|\widetilde{M}_y|^2$, $-(\widetilde{M}_y\widetilde{M}_z^* + \widetilde{M}_y^*\widetilde{M}_z)$, or $-(\widetilde{M}_x\widetilde{M}_y^* + \widetilde{M}_x^*\widetilde{M}_y)$, where the asterisks "$*$" mark the complex-conjugated quantity. The results for the perpendicular scattering geometry ($\mathbf{k}_0 \perp \mathbf{H}_0$) are [106]:

$$|\widetilde{M}_x|^2 = \frac{p^2}{2}\frac{\widetilde{H}_p^2\left(\left[1+p\sin^2\theta\right]^2+p^2l_D^2q^2\cos^2\theta\right)+2\widetilde{M}_z^2(1+p)^2l_D^2q^2\sin^2\theta}{\left(1+p\sin^2\theta-p^2l_D^2q^2\cos^2\theta\right)^2}, \tag{2.121}$$

$$|\widetilde{M}_y|^2 = \frac{p^2}{2} \frac{\widetilde{H}_p^2 \left(1 + p^2 l_D^2 q^2 \cos^2\theta\right) + 2\widetilde{M}_z^2 \left(1 + p\, l_D^2 q^2\right)^2 \sin^2\theta \cos^2\theta}{\left(1 + p \sin^2\theta - p^2 l_D^2 q^2 \cos^2\theta\right)^2}, \tag{2.122}$$

$$-\left(\widetilde{M}_y \widetilde{M}_z^* + \widetilde{M}_y^* \widetilde{M}_z\right) = \frac{2\widetilde{M}_z^2 p \left(1 + p\, l_D^2 q^2\right) \sin\theta \cos\theta}{1 + p \sin^2\theta - p^2 l_D^2 q^2 \cos^2\theta}. \tag{2.123}$$

The results for the parallel scattering geometry ($\mathbf{k}_0 \parallel \mathbf{H}_0$) are:

$$|\widetilde{M}_x|^2 = \frac{p^2}{2} \frac{\widetilde{H}_p^2 \left(1 + p(2+p) \sin^2\theta\right) + 2\widetilde{M}_z^2 (1+p)^2 l_D^2 q^2 \sin^2\theta}{(1+p)^2}, \tag{2.124}$$

$$|\widetilde{M}_y|^2 = \frac{p^2}{2} \frac{\widetilde{H}_p^2 \left(1 + p(2+p) \cos^2\theta\right) + 2\widetilde{M}_z^2 (1+p)^2 l_D^2 q^2 \cos^2\theta}{(1+p)^2}, \tag{2.125}$$

$$-\left(\widetilde{M}_x \widetilde{M}_y^* + \widetilde{M}_x^* \widetilde{M}_y\right) = p^2 \frac{\left(\widetilde{H}_p^2 p(2+p) + 2\widetilde{M}_z^2 (1+p)^2 l_D^2 q^2\right) \sin\theta \cos\theta}{(1+p)^2}. \tag{2.126}$$

For graphically displaying the Fourier components and SANS cross sections, we employ the sphere form factor for both $\widetilde{H}_p^2$ from Eq. (2.82) and $\widetilde{M}_z^2$ from Eq. (2.83). The averaged Fourier coefficients, Eqs. (2.121)−(2.126), need only to be multiplied by the corresponding trigonometric functions and summed up in order to obtain the magnetic SANS cross section.

Figures 2.16 and 2.17 visualize, respectively, for $\mathbf{k}_0 \perp \mathbf{H}_0$ and $\mathbf{k}_0 \parallel \mathbf{H}_0$ the angular anisotropy of the Fourier coefficients on a two-dimensional detector. It is seen that all Fourier coefficients are highly anisotropic, *e.g.*, $|\widetilde{M}_x|^2$ for $\mathbf{k}_0 \perp \mathbf{H}_0$ changes with increasing field from horizontally to vertically elongated. These anisotropies are clearly a consequence of the magnetodipolar interaction and of terms such as $l_D^2 q^2 \cos^2\theta$ related to the DM interaction. Note that both cross terms (CT) change sign at the borders between quadrants [Figs. 2.16(g)−2.16(i) and Figs. 2.17(g)−2.17(i)]. However, on multiplication with $\sin\theta\cos\theta$ (in order to arrive at the corresponding contribution to the cross section, compare Eq. (2.60) below) these terms become positive definite (at least for not too small q and H_i).

Although the averages of the magnetization Fourier components for $\mathbf{k}_0 \parallel \mathbf{H}_0$ are highly anisotropic (Fig. 2.17), the ensuing magnetic SANS cross sections are isotropic (θ-independent) for statistically isotropic materials. Therefore, we discuss for the remainder of this thesis only the (unpolarized and spin-polarized) SANS cross sections for the perpendicular scattering geometry.

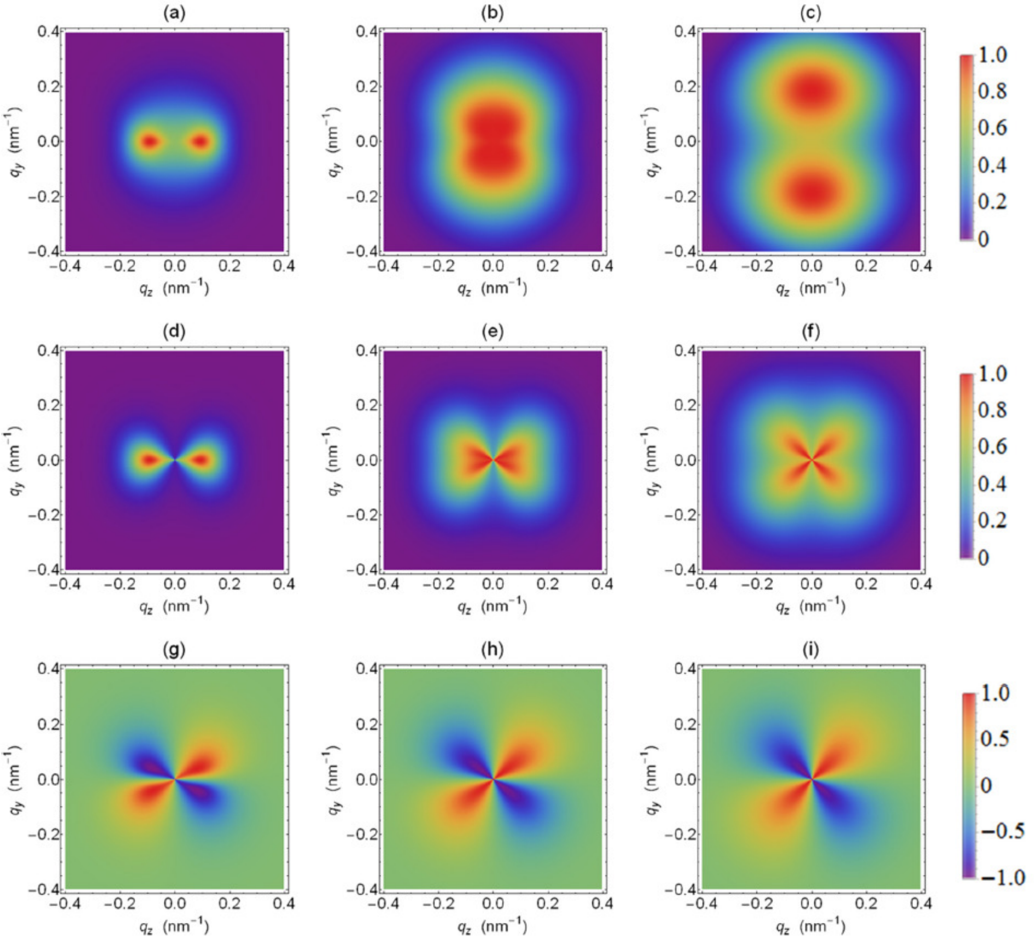

Fig. 2.16 Contour plots of the Fourier components of the magnetization at selected applied magnetic fields ($\mathbf{k}_0 \perp \mathbf{H}_0$). $|\widetilde{M}_x|^2$ (upper row), $|\widetilde{M}_y|^2$ (middle row), and $CT = -(\widetilde{M}_y\widetilde{M}_z^* + \widetilde{M}_y^*\widetilde{M}_z)$ (lower row) (based on Eqs. (2.121)−(2.123)). $\mathbf{H}_0 \parallel \mathbf{e}_z$ is horizontal in the plane. H_i values (in T) from left to right column: 0.5; 1.5; 10.0. All data were normalized to unity by the respective maximum value.

We remind the reader that for $\mathbf{k}_0 \perp \mathbf{H}_0$, the spin-misalignment unpolarized SANS cross section $\mathrm{d}\Sigma_M/\mathrm{d}\Omega$ reads (for more, see Eq. (2.64) and the discussion in Section 2.2.3):

$$\frac{\mathrm{d}\Sigma_M}{\mathrm{d}\Omega}(\mathbf{q}) = \frac{8\pi^3}{V} b_H^2 \left(|\widetilde{M}_x|^2 + |\widetilde{M}_y|^2 \cos^2\theta - (\widetilde{M}_y\widetilde{M}_z^* + \widetilde{M}_y^*\widetilde{M}_z) \sin\theta\cos\theta \right).$$

The spin-misalignment unpolarized SANS cross section $\mathrm{d}\Sigma_M/\mathrm{d}\Omega$ is shown in Fig. 2.18. With increasing field, $\mathrm{d}\Sigma_M/\mathrm{d}\Omega$ changes its angular anisotropy from an elliptically-distorted pattern with maxima along the horizontal direction (see Fig. 2.18(a)) to a clover-leaf-type anisotropy (see Fig. 2.18(b) and 2.18(c)). Figure 2.19 displays the (over 2π) azimuthally-averaged $\mathrm{d}\Sigma_M/\mathrm{d}\Omega$ at $\mu_0 H_i = 0.8\,\mathrm{T}$ with and without the DM term. Since the DM interaction

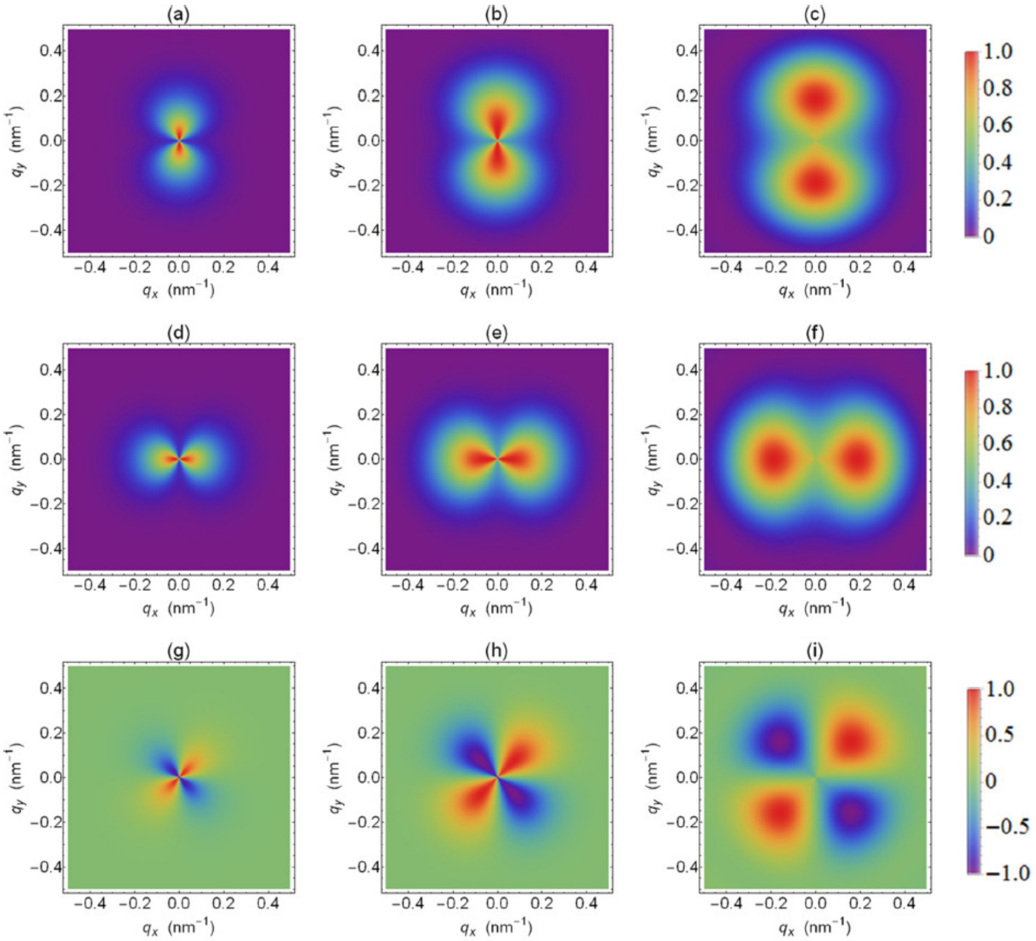

Fig. 2.17 Same as Fig. 2.16, but for $\mathbf{k}_0 \parallel \mathbf{H}_0$. $|\widetilde{M}_x|^2$ (upper row), $|\widetilde{M}_y|^2$ (middle row), and $CT = -(\widetilde{M}_x\widetilde{M}_y^* + \widetilde{M}_x^*\widetilde{M}_y)$ (lower row) (based on Eqs. (2.124)−(2.126)).

introduces nonuniformity into the spin structure, the spin-misalignment scattering cross section is larger when this term is included.

Assuming a perfect neutron optics and neglecting nuclear spin-incoherent SANS, the spin-flip SANS cross section of a bulk ferromagnet can be written as [107, 108]:

$$\frac{d\Sigma^{\pm\mp}}{d\Omega}(\mathbf{q}) = \frac{8\pi^3}{V} b_H^2 \Big(|\widetilde{M}_x|^2 + |\widetilde{M}_y|^2 \cos^4\theta + |\widetilde{M}_z|^2 \sin^2\theta\cos^2\theta \\ -(\widetilde{M}_y\widetilde{M}_z^* + \widetilde{M}_y^*\widetilde{M}_z)\sin\theta\cos^3\theta \mp i\chi(\mathbf{q}) \Big) , \tag{2.127}$$

where

$$\chi(\mathbf{q}) = \left(\widetilde{M}_x\widetilde{M}_y^* - \widetilde{M}_x^*\widetilde{M}_y\right)\cos^2\theta - \left(\widetilde{M}_x\widetilde{M}_z^* - \widetilde{M}_x^*\widetilde{M}_z\right)\sin\theta\cos\theta . \tag{2.128}$$

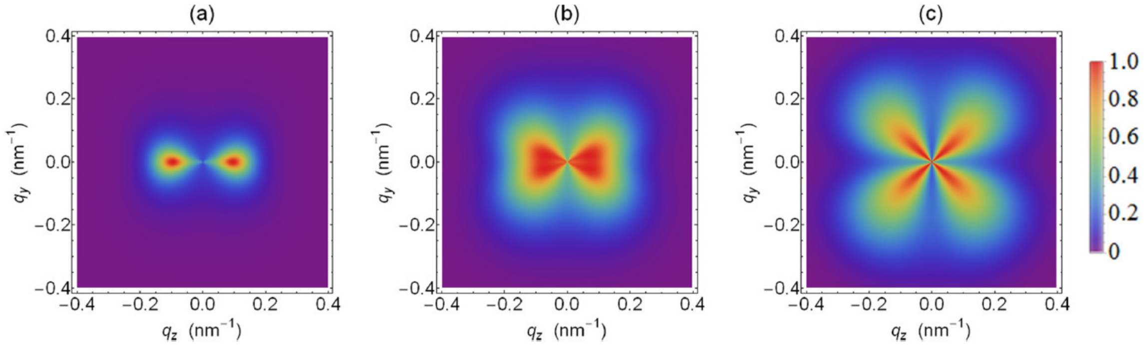

Fig. 2.18 Contour plots of $\mathrm{d}\Sigma_M/\mathrm{d}\Omega$ at selected applied magnetic fields (based on Eq. (2.64)) ($\mathbf{k}_0 \perp \mathbf{H}_0$). H_i values (in T) from left to right: 0.4; 0.8; 4.2. All data were normalized to unity by the respective maximum value.

We remind the reader that $\widetilde{M}_z$ is assumed to be real-valued and isotropic. The first superscript (*e.g.*, "+") that is attached to $\mathrm{d}\Sigma/\mathrm{d}\Omega$ in Eq. (2.127) refers to the spin state of the incident neutrons, whereas the second one (*e.g.*, "−") specifies the spin state of the scattered neutrons. Obviously, $\chi = 0$ when $\widetilde{M}_{x,y,z}$ are real-valued ($l_D = 0$). Inserting the expressions for the Fourier coefficients from Eqs. (2.118) and (2.119), and averaging over the direction of the magnetic anisotropy field yields for the difference of cross sections $-2i\chi(\mathbf{q}) = \frac{\mathrm{d}\Sigma^{+-}}{\mathrm{d}\Omega} - \frac{\mathrm{d}\Sigma^{-+}}{\mathrm{d}\Omega}$:

$$-2i\chi(\mathbf{q}) = \frac{2\widetilde{H}_p^2 p^3 \left(2 + p\sin^2\theta\right) l_D q \cos^3\theta + 4\widetilde{M}_z^2 p(1+p)^2 l_D q \sin^2\theta\cos\theta}{\left(1 + p\sin^2\theta - p^2 l_D^2 q^2\cos^2\theta\right)^2}. \qquad (2.129)$$

Using both the anisotropy-field Fourier coefficient $\widetilde{H}_p^2(qR)$ and for the longitudinal magnetization Fourier coefficient $\widetilde{M}_z^2(qR)$, the quantity $-2i\chi(\mathbf{q})$ is plotted in Fig. 2.20. The asymmetry term from Eq. (2.129) can also be studied by half-polarized experiments (polarized incident beam only), where the spin-up $\frac{\mathrm{d}\Sigma^{+}}{\mathrm{d}\Omega} = \frac{\mathrm{d}\Sigma^{++}}{\mathrm{d}\Omega} + \frac{\mathrm{d}\Sigma^{+-}}{\mathrm{d}\Omega}$ and spin-down $\frac{\mathrm{d}\Sigma^{-}}{\mathrm{d}\Omega} = \frac{\mathrm{d}\Sigma^{--}}{\mathrm{d}\Omega} + \frac{\mathrm{d}\Sigma^{-+}}{\mathrm{d}\Omega}$ SANS cross sections are measured.

At small fields, two extrema parallel and antiparallel to the field axis are observed (see Fig. 2.20(a) and 2.20(b)), whereas at larger fields additional maxima and minima appear approximately along the detector diagonals (see Fig. 2.20(c) and 2.20(d)). This change in anisotropy is due to the different field dependencies of the terms proportional to $\widetilde{H}_p^2$ and $\widetilde{M}_z^2$ in the enumerator of Eq. (2.129). The azimuthally-averaged expression $-2i\chi(q,H)$ is shown in Fig. 2.21 as a function of the applied magnetic field H_i for a fixed value of the DM constant D (*cf.* Fig. 2.21(a)) and as a function of D for a fixed H_i-value (*cf.* Fig. 2.21(b)). The strong field dependency of $-2i\chi(q,H)$ may be employed in order to experimentally determine the DM constant. Note that $-2i\chi(\mathbf{q})$ describes an asymmetry arising in the *elastic* SANS cross

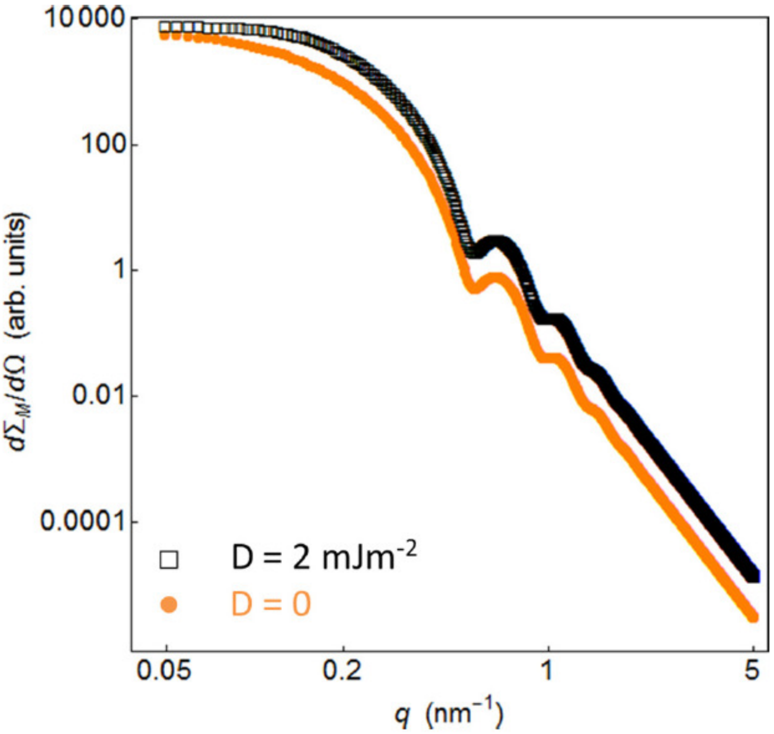

Fig. 2.19 Azimuthally-averaged $\mathrm{d}\Sigma_M/\mathrm{d}\Omega$ at $\mu_0 H_i = 0.8\,\mathrm{T}$ with and without the DM term (see inset) (log-log scale) ($\mathbf{k}_0 \perp \mathbf{H}_0$). Both $\mathrm{d}\Sigma_M/\mathrm{d}\Omega$ have been convoluted with the same Gaussian distribution function ($\overline{R} = 8\,\mathrm{nm}$; $\sigma = 0.7$) for both $\widetilde{H}_p^2$ and $\widetilde{M}_z^2$.

section due to the effect of the DM interaction on the *static magnetic microstructure*. We refer to Refs. [109, 110] for studies which address the inelastic and critical scattering related to the DM term.

For statistically isotropic systems (*e.g.*, polycrystalline magnetic materials), the predicted effect may not be observable due to the random orientation of the interfaces (grain boundaries) and the ensuing random orientation of the DM vectors. Therefore, one strategy to observe the polarization dependence of the spin-flip SANS cross section might be experiments on heavily deformed (cold-worked) magnets possessing a texture axis [111, 112] or on field-cooled nanocrystalline rare-earth magnets. [113, 114] For the latter, nanocrystallinity is required in order to guarantee a high defect (interface) density, whereas field cooling from the paramagnetic state at room temperature to a low-temperature ferromagnetic state may orient the DM vectors on the interfaces. On the other hand, introducing the effective DM interaction into the material via mechanical deformation may require form factors for $\widetilde{H}_p^2$ and $\widetilde{M}_z^2$ that are different from the spherically symmetric one used here for graphical visualization.

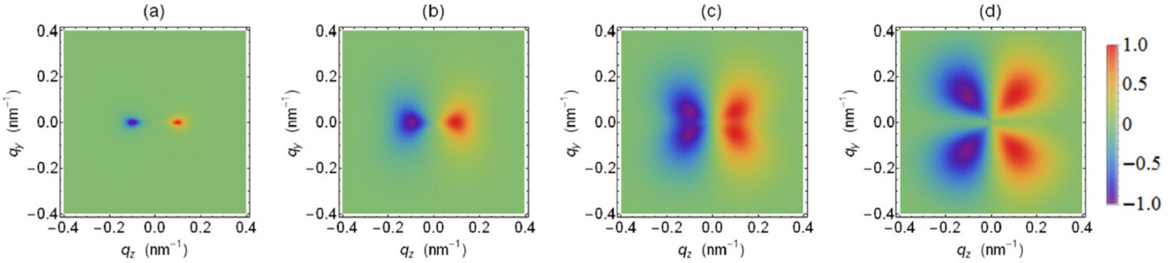

Fig. 2.20 Contour plots of the spin-flip difference cross section $-2i\chi(\mathbf{q})$ [Eq. (2.129)] at selected applied magnetic fields ($\mathbf{k}_0 \perp \mathbf{H}_0$). H_i values (in T) from left to right: 0.3; 0.6; 1.0; 3.5. All data were normalized to unity by the respective maximum value.

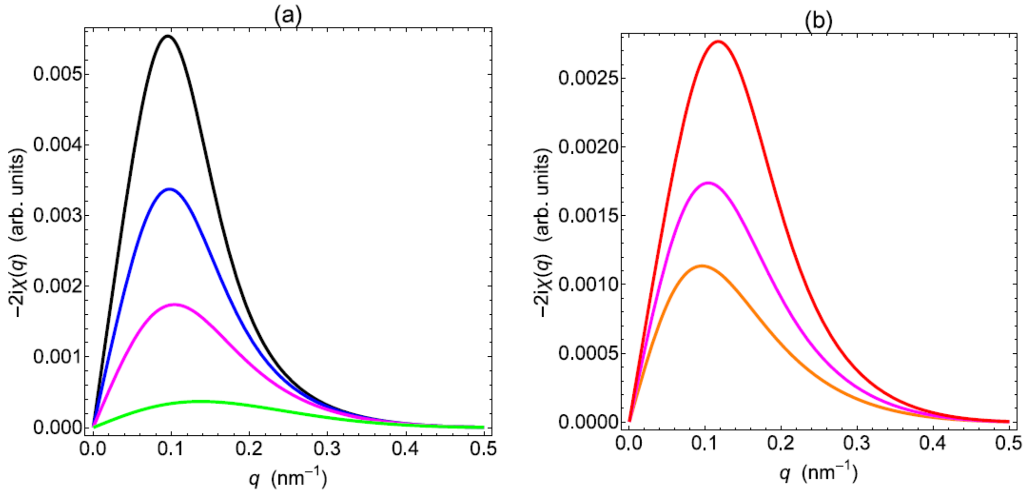

Fig. 2.21 Azimuthal average of the spin-flip difference cross section, $-2i\chi(q,H) = -2i\int_0^{\pi/2}\chi(q,H,\theta)d\theta$, at (a) selected applied magnetic fields and constant $D = 2.0\,\mathrm{mJ/m^2}$, and (b) for constant field $\mu_0 H_i = 0.8\,\mathrm{T}$ but varying DM constant D ($\mathbf{k}_0 \perp \mathbf{H}_0$). The field (in T) in (a) increases from top to bottom: 0.5; 0.6; 0.8; 2.0. The DM constant (in $\mathrm{mJ/m^2}$) in (b) increases from bottom to top: 1.5; 2.0; 2.5.

Chapter 3

Experimental

3.1 Samples and preparation

In the present work two systems of bulk metallic glass (BMG) have been studied: the first system is a soft magnetic alloy with the nominal composition $Fe_{70}Mo_5Ni_5P_{12.5}B_{2.5}C_5$, the second system is a hard magnetic alloy with the nominal composition $(Nd_{60}Fe_{30}Al_{10})_{92}Ni_8$. For each of two compositions, three samples were prepared for the SANS experiment: one called "As-cast" remained in the initial state, second called "Aged" was annealed at a moderate temperature (see the exact values below) in order to remove any stress induced during the sample preparation, and third called "Deformed" was deformed by an external compression force in order to study the effect of mechanical deformations on sample micromagnetic structure.

The soft magnetic samples with the nominal composition $Fe_{70}Mo_5Ni_5P_{12.5}B_{2.5}C_5$ were produced by Glassimetal Technology Inc. From the as-cast cylinder with 4 mm diameter, three discs with thicknesses of, respectively, 0.36, 0.38, and 0.28 mm were cut. One sample remained in the as-cast state, one specimen was aged at a temperature of 358 °C for 8 h in N_2 atmosphere, and one disc was mechanically deformed. Compression force was applied in the plane of the disc with a maximum value of 10^5 N. As a result of the deformation, the diameter of the disc in the applied-force direction was reduced from 4.0 to 3.6 mm; the resulting overall plastic deformation amounts to $\approx 3.5\,\%$.

The hard magnetic samples with the nominal composition $(Nd_{60}Fe_{30}Al_{10})_{92}Ni_8$ were produced at Universität des Saarlandes. First, master ingots of the alloy were produced from high-purity elements in an electric arc melter under Ar atmosphere. Then, pieces of the master ingots were remelted in a customized suction casting arc-melting device under Ar atmosphere, and cast into a water-cooled copper mold, yielding thin plates with dimensions of approximately $20 \times 10 \times 0.6$ mm. Three discs with thicknesses of, respectively, 0.48, 0.63, and 0.32 mm were wire-cut from the grinded plates. One sample remained in the as-cast state, one specimen was aged (annealed at 300 °C for 10 h in N_2 atmosphere) and one was first aged (annealed at 300 °C in N_2 atmosphere for 10 h) and then mechanically deformed. The deformation force was applied in the direction normal to the plane of the disc, with a resulting reduction of disc thickness from 0.32 to 0.31 mm (overall true plastic strain: $\varepsilon_p \cong 2.1\,\%$).

For the purpose of studying the microstructural-defect-induced Dzyaloshinski-Moriya interaction, there were prepared two Tb samples, and one Co sample. Disk-shaped nanocrystalline Tb samples with diameter of 8 mm and thickness $\sim 500\,\mu$m were synthesized by means of the inert-gas condensation technique, as described in detail in [95, 115, 116]. One Tb specimen was investigated in the as-prepared nanocrystalline state, while a second (reference) sample was annealed at 500 °C for 6 h; the annealing procedure induces grain growth, in this way reducing the volume fraction of grain boundaries. The average crystallite size of the as-prepared nanocrystalline Tb sample was determined by analysis of wide-angle x-ray diffraction data and found to be $D = 21 \pm 6\,$nm, while for the coarse-grained specimen $D \gtrsim 100\,$nm. Vibrating sample magnetometry was used to measure hysteresis loops and ac susceptibility. The Co sample was prepared from a high-purity polycrystalline ingot, which was deformed by cold rolling. As a result of the deformation, the thickness of the disc was reduced from 1.11 to 0.83 mm (overall true plastic strain: $\varepsilon_p \cong 25\,\%$).

3.2 Sample characterization measurements

The amorphous state of all the samples was checked before and after heat or mechanical deformation treatment by means of x-ray wide-angle diffraction and transmission electron microscopy. X-ray diffraction was performed in Bragg-Brentano geometry; the instrument (Bruker XRD) is equipped with Cu anode, which characteristic X-ray spectral lines correspond to the Kα transitions of the copper atom (radiation wavelength $\lambda = 0.15418\,$nm). The observed wide blurred peaks indicate the absence of any long-range periodic ordering in the samples (while for a crystalline material sharp peaks are expected).

The magnetic properties were studied using a vibrating sample magnetometer (Cryogenic VSM). The setup scheme is similar to other analogous setups [117]: a sample is put into a uniform magnetic field and is driven into a periodic sinusoidal motion; the periodic motion of the sample with non-zero magnetic moment $\mathbf{M}$ results in changing of magnetic flux passing through the pick-up coils; the voltage, which is induced by changing of magnetic flux passing through the pick-up coils, is proportional to the total magnetic moment of the sample. In the present work we have measured the field dependence of the mass magnetization M_z (mass magnetization is the sample magnetic moment divided by its mass). The magnetization data

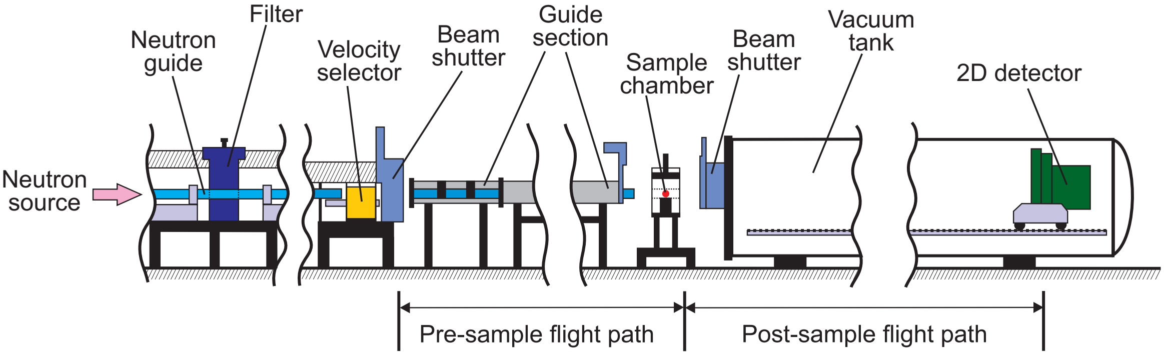

Fig. 3.1 An example a typical of SANS setup, based on the sketch of the NG-3 instrument from NIST [118].

were recorded at room temperature; the applied-field direction was in the plane of the samples (as in the SANS experiments). Magnetic field was provided by superconducting magnet and was varied from 14 T to -14 T. The samples masses were measured with absolute error 0.5 mg, which is less than 1% of relative error.

3.3 SANS experiment

Small-angle neutron scattering (SANS) is a popular technique for investigating nanoscale structural and magnetic inhomogeneities in the bulk of materials. It allows to study structure of material bulk of a scale 1-300 nm, providing information on both nuclear and magnetic structure of material. SANS is widely used in such fields as: biology, soft matter physics, nanostructured solid materials, (nano-)magnetism. The required size of a sample is usually of the order of 0.1-10 mm.

A typical scheme of SANS experiment is presented in Fig. 3.1 [118]. First of all, a high neutron flux (typical modern values are of the order of $\sim 10^{16}$) has to be produced, either by nuclear fission or spallation source. A nuclear fission neutron source is based on the uranium fission process; examples of such neutron sources are the Institut-Laue-Langevin, Grenoble, France and the Maier-Leibnitz Neutron Source, FRM-2 Garching, Germany. A spallation neutron source is based on the process when extremely high energy particles (*e.g.* accelerated protons) hit the target made of a neutron-rich material (*e.g.* W, U or Hg), exiting a heavy nucleus and causing them to radiate neutrons. Examples of such neutron sources are the Paul Scherrer Institut (Villingen, Switzerland) and ISIS (STFC Rutherford Appleton Laboratory, United Kingdom).

After being produced, neutron flux passes moderator media, which are typically large water (light or heavy) volumes surrounding the neutron source core. It is necessary in order to reduce neutron energy and obtain the wavelength of the order of several Å. Additionally it also serves as a biological shielding.

Produced at neutron source, neutrons are distributed to the SANS setup by neutron optical devices called neutron guides. The principle of their operation is based on total internal reflection phenomena and is similar to the one of light guides, where the light propagating in an optically dense media is totally reflected from the glass air-interface. An example of neutron guides are the NG-7 and NG-3 guide tubes at NIST, which supply the 30 m SANS instruments are coated internally with a thin layer of ^{58}Ni and have estimated transmission losses of about $1-2\,\% \cdot \mathrm{m}^{-1}$ [118].

Before entering the setup the beam is filtered, in order to remove remaining core γ-rays and fast neutrons. The filters consist of up to 200 mm of high-purity Bi, in the form of large (several tens of mm on a side) randomly oriented single-crystal grains, and 200 mm of vacuum-cast, polycrystalline beryllium [119], cooled to 77 K in a liquid-nitrogen cryostat.

Then the incoming neutron flux is monochromatized to a required λ by a wave-selector. The neutron wavelength is usually chosen as compromise between flux intensity and desired q-resolution of the instrument. The selector has a set of slotted disks that are spaced and phased along an angle to form helical pathways, thus the rotational frequency of the selector determines the mean wavelength of the quasi-continuous transmitted beam. Immediately following the velocity selector, a low-efficiency fission monitor is placed, which counts the intensity of the monochromatic beam during data collection, accumulating it in a separate channel. Completed data sets are then normalized to a fixed number of neutrons incident on the sample, removing the influence of any variation in the reactor power or cold source temperature during the measurement.

In order to avoid scattering from sample or sample holder edges, the sample is usually masked by a cadmium (or borated aluminum) plate with a hole in the center; the exposed area of the sample is desired to be as large as possible. The sample may be exposed to different environment conditions: temperature T, magnetic field $\mathbf{H}_0$ etc. The only requirements are: the device should be reasonably transparent to the neutron beam in order to reduce background scattering, and it should have low ability to be activated by incoming neutron flux.

Right after the sample there is a vacuum tank with the detector inside. A stepping-motor-driven carriage moves along rails inside the vessel to vary the sample-to-detector distance, which determines accessible q-range. The two-dimensional position-sensitive neutron detectors used on the SANS instruments are multiwire proportional counters (MWPC). The counter has three planes of parallel wires, a central anode wire plane and two orthogonal cathode wire planes, each with a $\sim$ 10 mm spacing between adjacent wires. The spatial resolution function, measured with a collimated beam incident on a 1 mm aperture in front of the detector, is approximately Gaussian with a full-width at half maximum (FWHM) equal to 10 mm in both directions. The first signal from each cathode plane that crosses a preset threshold level determines the coordinate assigned to the position of the captured neutron. A coincidence circuit verifies that a threshold crossing occurs on both the X and Y cathodes within a preset interval (typically 100 ns) before sending the digitized event coordinates to the data acquisition system. From the point of view of data acquisition, the detector MWPC system corresponds to the two-dimensional discrete pixel grid; it provides the neutrons counts intensity map for each pixel, and for each pixel it is possible to calculate related neutron momentum-transfer vector $\mathbf{q}$. In order to protect the detector from the direct beam and remove it from experimental data, there are beam stops made from a boron carbide/aluminium composite material or a ^{6}Li-loaded silicate glass have been found to be equally effective in stopping the unscattered beam without producing any detectable background in the counter.

The scattering data measured during experiment contains actually not only scattering from the sample, but several additional undesired contributions: dark-current scattering, sample container (empty cell) scattering, accidently counted gamma-rays, etc. In order to extract the scattering from the sample from experimental data, it must be treated in so-called "data reduction" process prior to be analyzed. Part of the data treatment is usually done automatically by setup software during the data acquisition or before the experiment (*e.g.* detector calibration, data smearing corrections etc.), part requires additional measurements, *i.e.* reference measurements: empty cell scattering, sample and empty cell transmission, empty beam transmission and "dark current" (parasitic) scattering.

The standard scattering measurement provides as a result a two-dimensional intensity $I(\mathbf{q})$ distribution over all of the detector area. The transmission T is the ratio of neutron counts passed through the sample to the incident neutron counts; thus the transmission measurement is limited only to the area around the primary beam. During such measurement, the beamstop has to be displaced and thus the detector must be protected by a beam attenuator (or by set of different attenuators with attenuation coefficients). The time of data acquisition of any measurement should be sufficient to get not less than $\sim 3 \cdot 10^6$ counts (as a rule of thumb), in order to obtain reasonable value of the measurements statistical error. Note that in case the subtracted data (spin-misalignment SANS, difference between the sample and background etc.) are the interest of experiment, it is the difference between total counts that should satisfy the criteria, while the required amount of counts for the particular measurement may be higher.

To summarize, for a complete data reduction procedure it is necessary to measure:

1. Sample scattering intensity I_{sample}:

$$I_{\text{sample}} = I_0 \, T_{\text{sample + cell}} \left(\frac{d\Sigma_{\text{sample}}}{d\Omega} + \frac{d\Sigma_{\text{cell}}}{d\Omega} \right) + I_{\text{blocked beam}}, \tag{3.1}$$

where I_0 is a flux coefficient:

$$I_0 = \phi \, A \, d \, \Delta\Omega \, \varepsilon \, t,$$

ϕ is incident neutron flux, A is sample area, d is sample thickness, $\Delta\Omega$ is solid angle of each pixel, ε is detector efficiency and t is data acquisition time.

2. Empty cell (sample holder) scattering intensity I_{cell}:

$$I_{\text{cell}} = I_0 \, T_{\text{cell}} \frac{d\Sigma_{\text{cell}}}{d\Omega} + I_{\text{blocked beam}}. \tag{3.2}$$

3. Blocked beam intensity $I_{\text{blocked beam}}$ - (also called "dark current" scattering) measurement when there is no incident neutron beam, thus it consists of detector counts triggered by other sources like: cosmic rays, accidentally passing gamma-rays.

4. Sample and empty cell transmissions

$$T_{\text{sample, cell}} = \frac{N_{\text{sample, cell}}}{N_0}, \tag{3.3}$$

where $N_{\text{sample, cell}}$ is amount of counts in the direct beam area with sample or empty cell, and N_0 is is amount of counts in the direct beam area with no sample in the beam path.

5. Empty beam transmission (for absolute scaling):

$$I_D = \phi A \, T_{\text{att}} \, \Delta\Omega \, \varepsilon \, t, \tag{3.4}$$

where T_{att} is attenuation coefficient.

Once everything is measured, the corrected data can be calculated by the following equation [120]:

$$I_{\text{corr}} = (I_{\text{sample}} - I_{\text{blocked beam}}) - \frac{T_{\text{sample + cell}}}{T_{\text{cell}}} (I_{\text{cell}} - I_{\text{blocked beam}}). \tag{3.5}$$

Additionally, the detector efficiency should be taken into account. The detector efficiency is usually measured before the experiment (*e.g.* in the beginning of facility cycle) as scattering of a standard sample which gives strongly isotropic scattering: water or plexiglass. This procedure relates corrected intensity to the final expression of intensity $I_{\text{calibrated}} =$

$I_{\mathrm{corr}} \cdot$ detector efficiency. With that measurement sensitivity of each pixel can be calculated and $I_{\mathrm{calibrated}}$ can be obtained.

The final expression for the calibrated intensity $I_{\mathrm{calibrated}}$ reads:

$$I_{\mathrm{calibrated}} = \phi A \; d \; T_{\mathrm{sample + cell}} \; \frac{\mathrm{d}\Sigma_{\mathrm{sample}}}{\mathrm{d}\Omega} \; \Delta\Omega \; \varepsilon \; t, \tag{3.6}$$

and finally the cross section in absolute units is calculated as:

$$\frac{\mathrm{d}\Sigma_{\mathrm{sample}}}{\mathrm{d}\Omega} = \frac{I_{\mathrm{calibrated}}}{I_D} \cdot \frac{1}{d} \cdot \frac{T_{\mathrm{att}}}{T_{\mathrm{sample + cell}}}. \tag{3.7}$$

All required mathematical procedures are implemented in GRASP [121] (or by a number of other programs like IGOR Pro [122], QTIKWS [123] etc.).

The actual SANS experiments were carried out at the instruments D33 [124] at the Institut Laue-Langevin (ILL), Grenoble, France and at the instrument SANS-I [125] at the Paul Scherrer Institute (PSI), Villingen, Switzerland. During the presented experiments, unpolarized incident neutrons were used with a mean wavelength of $\lambda = 6\,\text{Å}$ and a wavelength broadening of $\Delta\lambda/\lambda \sim 10\,\%$ (FWHM). The data were acquired at q-range of $0.035\,\mathrm{nm}^{-1} \lesssim q \lesssim 1.5\,\mathrm{nm}^{-1}$. Neutron-scattering data were recorded at room temperature as a function of an external magnetic field $\mathbf{H}_0$, which was applied perpendicular to the wave vector $\mathbf{k}_0$ of the incident neutron beam ($\mathbf{k}_0 \perp \mathbf{H}_0$); see Fig. 2.3 for a sketch of the SANS setup. The field was cycled by first applying a large value, which is assumed to bring the sample into the approach-to-saturation regime, and then decreasing it following the major hysteresis loop. SANS-data reduction (correction for background scattering, transmission, detector efficiency) was carried out using the GRASP software package [121].

The SANS experiment on Tb and Co samples was carried out at the SANS-I instrument at the Paul Scherrer Institute, Villigen, Switzerland. We used polarized incident neutrons with a mean wavelength of $\lambda = 6\,\text{Å}$ broadening of $\Delta\lambda/\lambda \sim 10\,\%$ (FWHM). The external magnetic field $\mathbf{H}_0$ was provided by a cryomagnet and applied perpendicular to the wave vector $\mathbf{k}_0$ of the incident neutron beam. The beam was polarized by means of a remanent FeSi supermirror transmission polarizer ($m = 2.6$), and a rf spin flipper, installed close to the sample position, allowed us to reverse the initial neutron polarization; the flipping efficiency of the rf flipper is $e \approx 99\,\%$ and the polarization of the beam is $P = 93\,\%$.

Chapter 4

Experimental results and discussion

4.1 Magnetic small-angle neutron scattering on bulk metallic glasses

4.1.1 Soft magnetic bulk metallic glass $\mathrm{Fe_{70}Mo_5Ni_5P_{12.5}B_{2.5}C_5}$

The results of the magnetization measurements are shown in Fig. 4.1. All samples are classified as soft magnetic, and a field of the order of 0.2 T is sufficient to magnetically saturate them. The saturation magnetization of the aged sample ($M_s = 111.6\,\mathrm{emu\,g^{-1}}$) is slightly larger than the saturation magnetization of the other two samples ($M_s = 109.5\,\mathrm{emu\,g^{-1}}$ for the as-cast and $M_s = 108.3\,\mathrm{emu\,g^{-1}}$ for the deformed BMG). The inset in Fig. 4.1 depicts the field dependence of the total detector count rate. In the saturated state, the count rate is extremely low (only $1-2\,\mathrm{counts\ mm^{-1}\,sr^{-1}}$), which indicates a quite weak residual scattering cross section (compare Eqs. (2.60)$-$(2.61)). Reducing the applied field below 200 mT results in a strong increase of the count rate (compare with the $M(H_0)$ data in Fig. 4.1), which suggests that the measured total $\mathrm{d}\Sigma/\mathrm{d}\Omega$ is dominated by the spin-misalignment scattering (compare Eqs. (2.60)$-$(2.64)). The as-cast and deformed samples assume at zero and low fields a plateau value of the count rate to then monotonically decrease and practically vanish beyond 250 mT; the aged sample starts out from a much lower count rate at zero field to then increase and assume a maximum at around 80 mT, followed by a monotonic decrease similar to the other samples. This difference in count-rate behavior between the samples is however not visible in the $M(H_0)$ data. Note that for fields below about 50 mT the count rates of all samples change only very weakly, while the values of $M(H_0)$ keep decreasing.

The experimental two-dimensional unpolarized SANS cross sections $\mathrm{d}\Sigma/\mathrm{d}\Omega$ are displayed in Fig. 4.2. In agreement with the field dependence of the count rates, the scattering

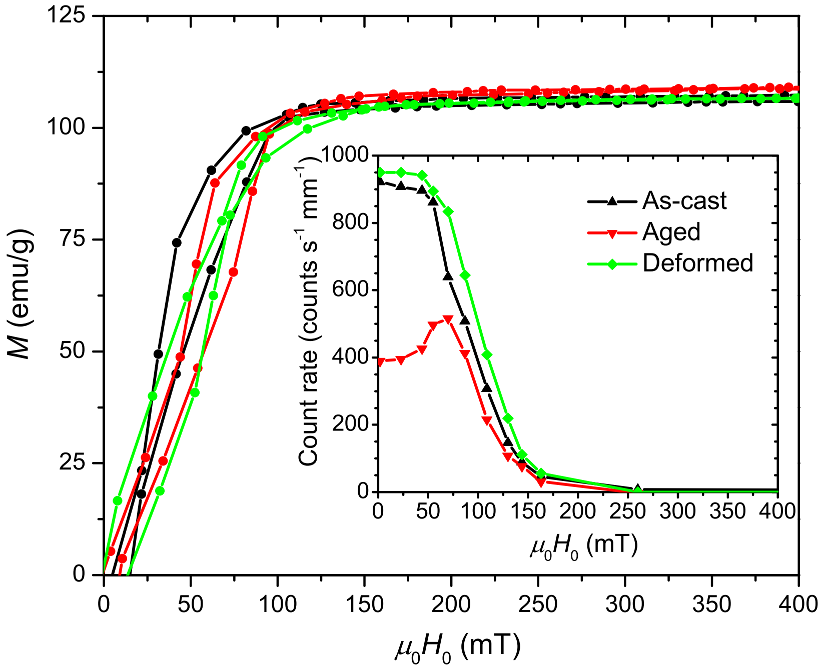

Fig. 4.1 Room-temperature magnetization curves of as-cast, aged, and deformed $\mathrm{Fe_{70}Mo_5Ni_5P_{12.5}B_{2.5}C_5}$ (only the upper right quadrant is shown). Inset shows the field dependence of the neutron count rate of the samples normalized by the respective sample thickness. Measured q-range for the count rate is $0.035\,\mathrm{nm}^{-1} \lesssim q \lesssim 0.3\,\mathrm{nm}^{-1}$.

at saturation (left column in Fig. 4.2, $\mu_0 H_0 = 1496\,\mathrm{mT}$) is for all samples much weaker than the scattering at lower fields; additionally $\mathrm{d}\Sigma/\mathrm{d}\Omega$ at saturation is isotropic. From the expression for the residual SANS cross section (*cf.* Eq.(2.61)), one may see that $\mathrm{d}\Sigma_{\mathrm{res}}/\mathrm{d}\Omega$ consists of two terms: the isotropic nuclear scattering $\sim |\widetilde{N}|^2$, and the anisotropic longitudinal magnetic scattering $\sim |\widetilde{M}_z|^2 \sin^2\theta$. Note that for statistically isotropic samples both Fourier components $|\widetilde{N}|^2$ and $|\widetilde{M}_z|^2$ are isotropic [13]. Therefore, the observed isotropic pattern of the residual scattering cross section strongly indicates that the nuclear scattering term dominates $\mathrm{d}\Sigma_{\mathrm{res}}/\mathrm{d}\Omega$, *i.e.*, $|\widetilde{N}|^2 \gg b_H^2 |\widetilde{M}_z|^2$. Moreover, since $\mathrm{d}\Sigma_{\mathrm{res}}/\mathrm{d}\Omega$ and, hence, $|\widetilde{N}|^2$ is much smaller than the spin-misalignment SANS cross section, this then implies that $\mathrm{d}\Sigma_M/\mathrm{d}\Omega = S_H R_H + S_M R_M$ is dominated by the anisotropy-field related scattering term $S_H R_H$, rather than by the magnetostatic contribution $S_M R_M$ (compare Eqs.(2.68)−(2.70)).

With decreasing field down to the remanent state, the two-dimensional SANS patterns in Fig. 4.2 reveal a combination of different angular anisotropies, which can be related to the different magnetization Fourier components in Eq. (2.60). Overall, the cross sections in Fig. 4.2 exhibit an elongation along the horizontal field direction for fields down to a few 10 mT, which is a strong indication for the presence of long-range spin misalignment (*cf.* the term $|\widetilde{M}_y|^2 \cos^2\theta$ in Eq. (2.60)). In particular, we refer to the data at 70 mT which

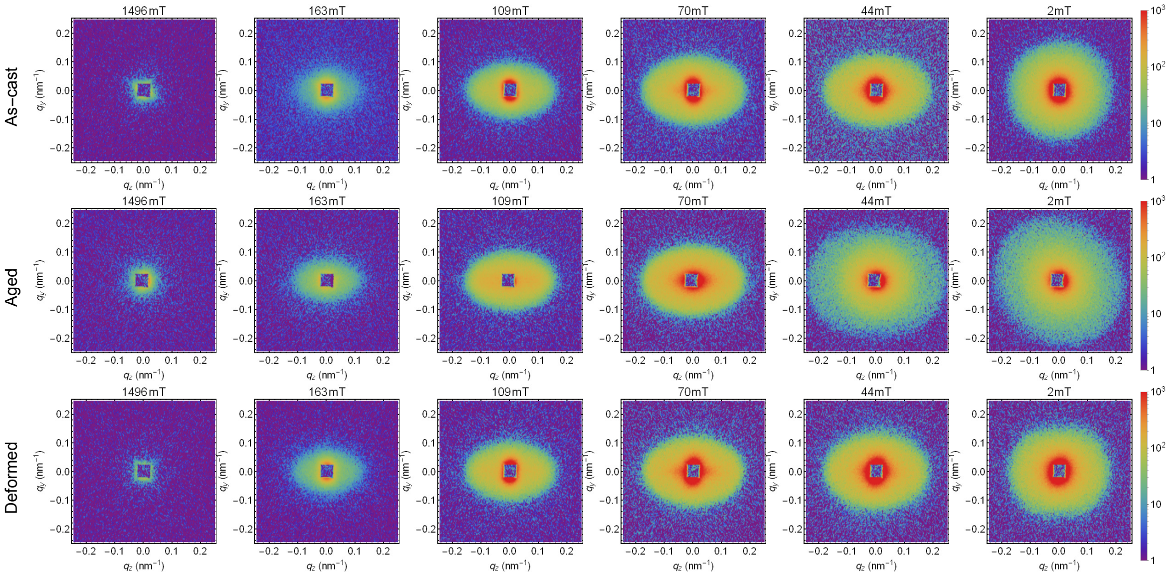

Fig. 4.2 Two-dimensional total (nuclear and magnetic) unpolarized SANS cross sections $d\Sigma/d\Omega$ of as-cast, aged, and deformed BMG alloy $Fe_{70}Mo_5Ni_5P_{12.5}B_{2.5}C_5$ at selected applied magnetic fields (logarithmic color scale). $\mathbf{H}_0$ is horizontal in the plane. Note the relatively pronounced and sharp maximum ("spike") of the $d\Sigma/d\Omega$ of the deformed sample at 70 mT.

show at small q a pronounced sharp maximum of the neutron intensity for directions parallel and antiparallel to the applied field. This so-called "spike anisotropy" has previously been observed in a SANS study on sintered Nd-Fe-B magnets [102], and it is related to the formation of flux-closure patterns on a nanometer length scale; more specifically, it is related to the term $p \sin^2\theta$ in the denominator of the response function R_H (see Eq. (2.71)). Figure 4.3 illustrates the angular dependence of $d\Sigma_M/d\Omega$ taken at $\mu_0 H_0 = 70\,\mathrm{mT}$ for a set of q-values near the beamstop (shown in red color) and near the borders of the detector (shown in dark blue color). While the aged sample shows maxima only at angles $\theta \sim 0°$ and $180°$, which are related to an horizontal elongation of $d\Sigma/d\Omega$, the as-cast and deformed samples both exhibit additional peaks at $\theta \sim 90°$, which quickly fade away with increasing q. This behavior can be best observed at fields of 109 mT and 70 mT, although it is present down to the remanent state. When approaching zero field, the SANS cross sections tend to be more isotropic, although for the aged sample $d\Sigma/d\Omega$ reveals an elongated angular anisotropy oriented at about 135° relative to the horizontal direction. This feature might be related to the unusual low-field behavior of the count rate in Fig. 4.1; to this end, we can only speculate that its origin may be related to the formation of domain structure absent in the other two specimens. Note the absence of any sign of clover-leaf-shaped angular anisotropy (with maxima roughly along the detector diagonals, *cf.* the angular variation of R_M). As discussed

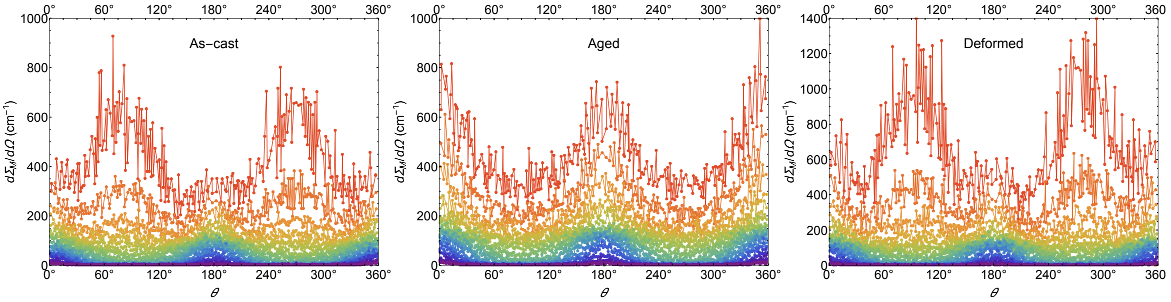

Fig. 4.3 Comparison of the angular θ-dependence of $\mathrm{d}\Sigma_M/\mathrm{d}\Omega$ of as-cast, aged, and deformed $\mathrm{Fe_{70}Mo_5Ni_5P_{12.5}B_{2.5}C_5}$ at $\mu_0 H_0 = 70\,\mathrm{mT}$. Red color corresponds to low q-values around the beamstop ($q \cong 0.035\,\mathrm{nm}^{-1}$), while blue color represents high q-values from around the borders of the detector ($q \cong 0.2\,\mathrm{nm}^{-1}$).

before, this can be related to the fact that the spin-misalignment SANS cross section of the soft magnetic BMG is dominated by the term $S_H R_H$ due to the magnetic anisotropy field.

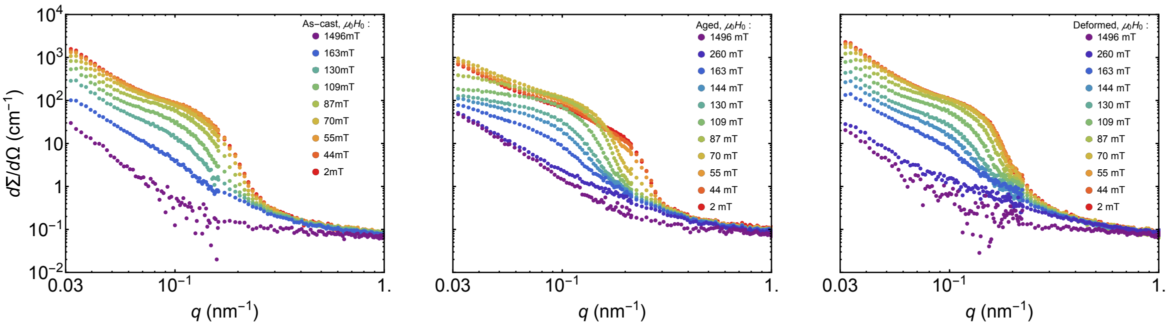

Fig. 4.4 Azimuthally-averaged total $\mathrm{d}\Sigma/\mathrm{d}\Omega$ of as-cast, aged, and deformed $\mathrm{Fe_{70}Mo_5Ni_5P_{12.5}B_{2.5}C_5}$ at selected applied magnetic fields (see insets, log-log scale).

The radially-averaged total and spin-misalignment scattering cross sections were obtained by integration of the corresponding two-dimensional data over an angular range of 2π and are respectively displayed in Figs. 4.4 and 4.5. In agreement with the count rate in Fig. 4.1, all samples show strong spin-misalignment scattering with a change of $\mathrm{d}\Sigma_M/\mathrm{d}\Omega$ by up to two orders of magnitude between saturation and $0\,\mathrm{T}$. For the as-cast and deformed samples, the scattering monotonously increases with decreasing field down to $\sim 70\,\mathrm{mT}$, and then remains essentially unchanged for smaller fields; note, however, that (for these samples) the angular anisotropy of the cross sections in Fig. 4.2 continues to change even for $\mu_0 H_0 < 70\,\mathrm{mT}$. For the aged sample, $\mathrm{d}\Sigma_M/\mathrm{d}\Omega$ increases with decreasing field down to $\sim 55\,\mathrm{mT}$, and then begins decreasing with a concomitant shifting of the shoulder in the SANS curves to larger q-values. Spin-misalignment scattering on a scale above $q \gtrsim 0.5\,\mathrm{nm}^{-1}$ becomes essentially field-independent for all samples. The comparison of the $\mathrm{d}\Sigma_M/\mathrm{d}\Omega$ for all three samples is shown in Fig. 4.6. The as-cast and deformed samples show qualitatively a similar behavior, with the

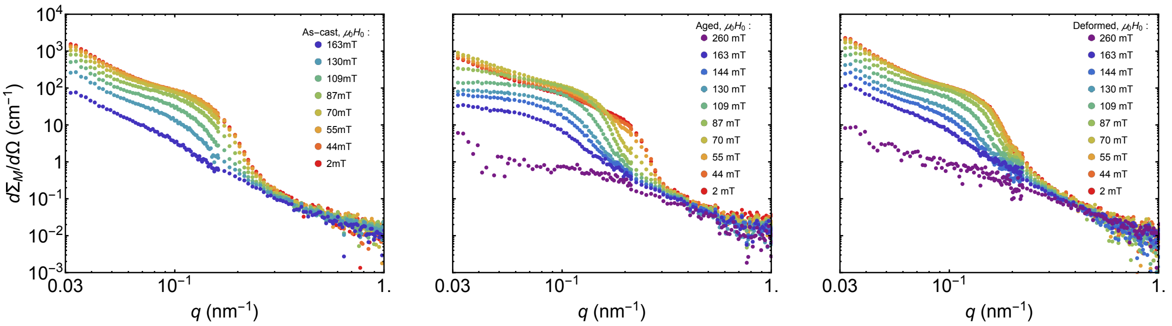

Fig. 4.5 Azimuthally-averaged spin-misalignment SANS cross sections $\mathrm{d}\Sigma_M/\mathrm{d}\Omega$ of as-cast, aged, and deformed $\mathrm{Fe_{70}Mo_5Ni_5P_{12.5}B_{2.5}C_5}$ at selected applied magnetic fields (see insets, log-log scale). The respective scattering at saturation (1496 mT) has been subtracted in each data set.

deformed sample exhibiting a larger spin-misalignment scattering. It also becomes visible in Figs. 4.5 and 4.6 that with increasing field the shoulders in $\mathrm{d}\Sigma_M/\mathrm{d}\Omega$ evolve to smaller q-values and basically vanish or disappear from the accessible range of momentum transfers. As we will see in the following, this feature is related to an increase of long-wavelength spin-misalignment fluctuations.

The difference between the aged sample and the as-cast and deformed samples becomes more evident when one inspects the two-dimensional correlation functions $c(y,z)$ (see Fig. 4.7). Since the spin-misalignment SANS cross sections are highly anisotropic, this feature also transfers to the correlation functions. The $c(y,z)$ of the aged sample for fields above 44 mT are strongly elongated along the vertical direction (which is perpendicular to the field direction). At 109 mT, the $c(y,z)$ of the aged sample exhibits negative values for $20\,\mathrm{nm} \lesssim r \lesssim 50\,\mathrm{nm}$ (shown in dark-purple color), except for the values in the direction perpendicular to the field. In nuclear SANS, negative values of the distance distribution function $p(r) = r^2\gamma(r)$ are attributed to distances that connect regions with opposite sign of the scattering length density more frequently than regions with the same sign [126]. However, for magnetic SANS, such a straightforward interpretation of the correlation function of the spin-misalignment SANS cross section in terms of a specific magnetization distribution cannot be made. This is because $c(y,z)$ — being the Fourier transform of $\mathrm{d}\Sigma_M/\mathrm{d}\Omega$ (*cf.* Eq. (2.64)) — is not the autocorrelation function of the magnetization, in contrast to $\gamma(r)$, which is the autocorrelation function of the nuclear density $N(\mathbf{r})$. Nevertheless, the observation that $c(y,z)$ of the aged sample is negative at 109 mT and for $20\,\mathrm{nm} \lesssim r \lesssim 50\,\mathrm{nm}$ may indicate the existence of magnetization components that are oriented opposite to a given magnetic moment at the origin.

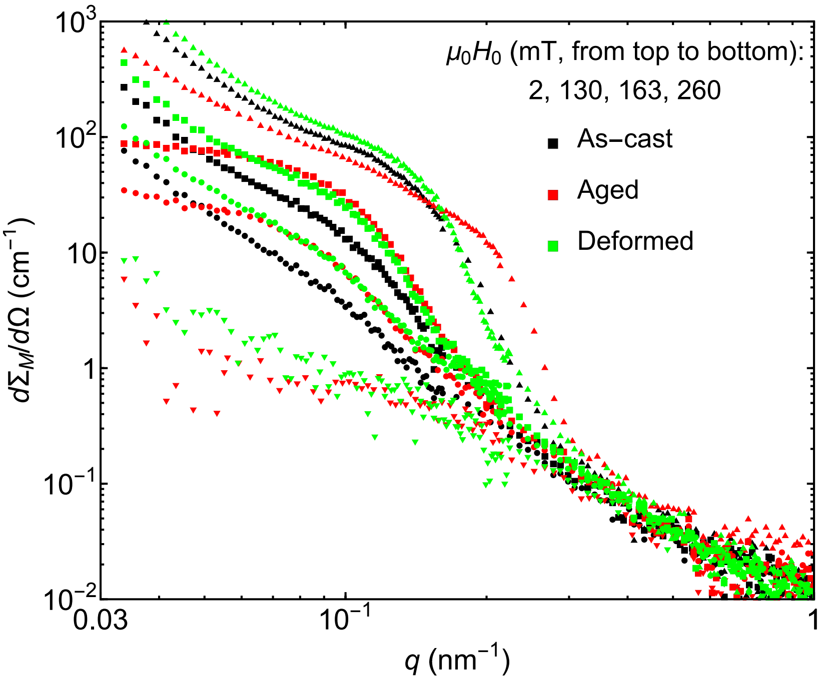

Fig. 4.6 Comparison of $\mathrm{d}\Sigma_M/\mathrm{d}\Omega$ of as-cast, aged, and deformed $\mathrm{Fe_{70}Mo_5Ni_5P_{12.5}B_{2.5}C_5}$ at selected applied magnetic fields (see insets, log-log scale).

For the as-cast and deformed samples, the $c(y,z)$ show at large r an increase of the horizontal component with decreasing field, in agreement with the two-dimensional scattering data in Fig. 4.2, which reveal an increasing vertical component at small q. Likewise, for small values of r, corresponding to large c-values ($c \gtrsim 0.8$), the anisotropy of the correlation function shows a maximum along the vertical direction for all samples, corresponding to a horizontal elongation in **q**-space. Moreover, the $c(y,z)$ of the aged sample decay faster than the $c(y,z)$ of the other two samples.

To extract a single average correlation length from the data, we have computed the field-dependent 2π-averaged SANS cross sections, and we have estimated the correlation length l_C as the $\exp(-1)$ length from the numerically computed correlation functions according to Eq. (2.101). As an example, Fig. 4.17 depicts such correlation functions $c(r)$ of the rare-earth-based BMG, which we are going to discuss in the next paragraph. The results for $l_C(H_0)$ of the soft magnetic BMG are shown in Fig. 4.8. The correlation lengths of the as-cast and deformed samples vary from about $5-25$ nm, while the l_C of the aged sample takes on values of $\sim 5-20$ nm (resembling the count rate behavior in Fig. 4.1). Regarding the absolute l_C-values, one recognizes that the aged BMG exhibits the smallest correlation lengths; this can be explained by the fact that the aging procedure (10 h at 300 °C) goes along with enthalpy and concomitant structural relaxation, which then results in a smaller

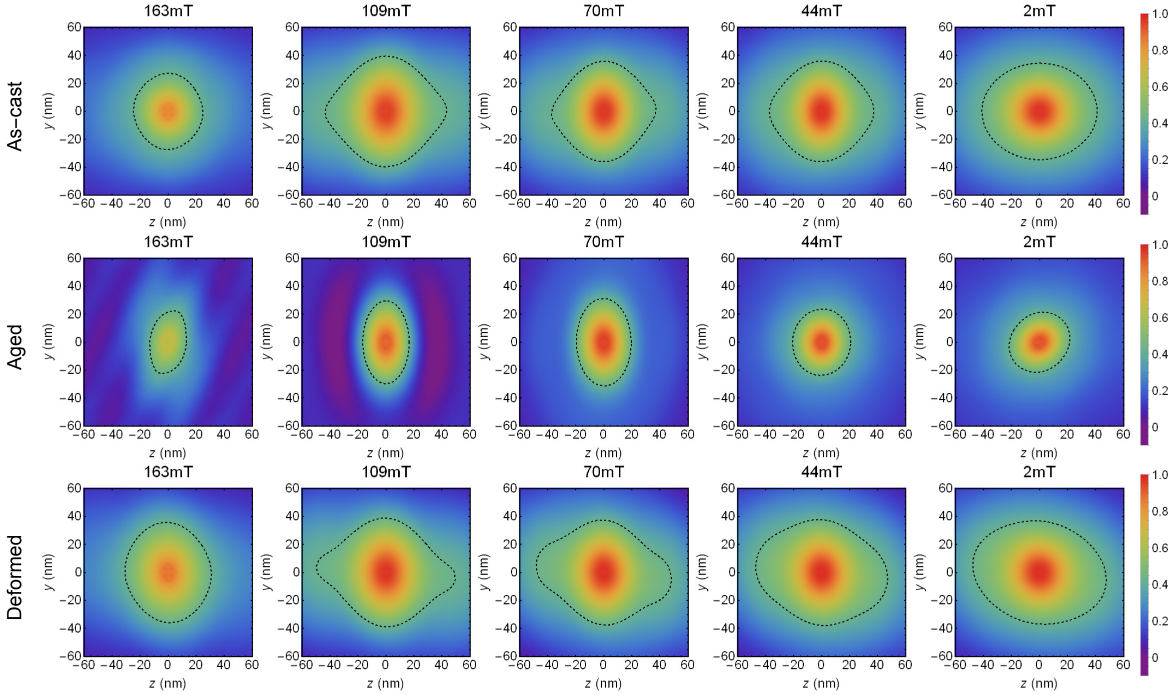

Fig. 4.7 Field dependence of the two-dimensional (normalized) correlation functions $c(y,z)$ (computed according to Eq. (2.98)) of as-cast, aged, and deformed $\mathrm{Fe_{70}Mo_5Ni_5P_{12.5}B_{2.5}C_5}$ at selected applied magnetic fields (see insets). $\mathbf{H}_0$ is horizontal in the plane. Dashed contour lines: $c(y,z) = \exp(-1)$.

size of nonuniform magnetization structures. In agreement with this assessment, we see in the magnetization data (Fig. 4.1) that the aged sample exhibits a slightly larger high-field magnetization than the other two samples; on the other hand, the deformed sample has the smallest magnetization and the largest l_C-values. The results in Figs. 4.7 and 4.8 strongly suggest that spin-misalignment correlations in the soft magnetic alloy are anisotropic and decay on a real-space length of the order of a few tens of nanometers. In this context, it is worth mentioning that an x-ray and neutron-diffraction study on stress-relieved and field-annealed amorphous magnetic $\mathrm{Fe_{78}Si_9B_{13}}$ ribbons [127] reports that modifications in the interatomic distances may greatly change the nature of the magnetic coupling, resulting in antiferromagnetic correlations that decay on an *atomic scale*.

4.1.2 Hard magnetic bulk metallic glass $\mathrm{(Nd_{60}Fe_{30}Al_{10})_{92}Ni_8}$

The results of the magnetization measurements are shown in Fig. 4.9. Although an applied field of about 8 T is sufficient to bring the samples into the approach-to-saturation regime, complete saturation is not reached. The field dependence of the count rate follows the magnetization behavior, exhibiting a maximum at the respective coercive field H_c: for the as-

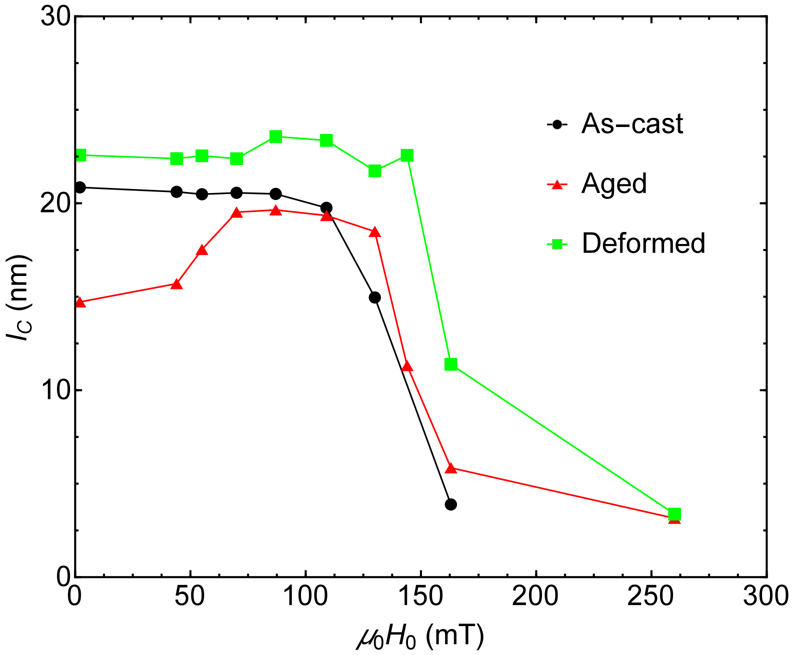

Fig. 4.8 Field dependence of the correlation length l_C of as-cast, aged, and deformed $Fe_{70}Mo_5Ni_5P_{12.5}B_{2.5}C_5$ (lines are guides to the eyes). Note that the l_C were obtained using the correlation functions computed according to Eq. (2.101).

cast, aged, and deformed samples the values of H_c are, respectively, 0.30 T, 0.34 T, and 0.30 T. We also would like to note that previous investigations on similar rare-earth-based magnetic BMG reported a strong dependency of H_c on the synthesis method and on the quenching rate [128]. The mechanism that leads to coercivity in these type of materials is generally believed to be due to the pinning of domain walls, for instance, by paramagnetic Nd-rich precipitates which are present in the x-ray amorphous samples [129]. The most remarkable observation in Fig. 4.9 is, however, the *increase* of the magnetization on mechanical deformation, which is somewhat counter intuitive: application of mechanical load usually generates defects and/or disorder in the deformed material and as a consequence one expects that the related spin misalignment in the vicinity of the defects contributes to a *reduction* of the magnetization component along the field direction (compare the $M(H_0)$ data of the soft magnetic BMG in Fig. 4.1). At 8 T, this increase of the magnetization amounts to $\sim 20\,\%$ relative to the as-prepared sample. A possible explanation might be that through the plastic deformation Nd-rich nanoclusters, which do pre-exist in the amorphous sample [129], deform into aligned and shape-anisometric (*e.g.*, platelet-shaped) nanocrystals, and that these contribute via their shape anisotropy to the magnetization. A similar increase of the magnetization was observed in plastically-deformed Ba-ferrite composites [130]. Although our electron-microscopy data reveal crystalline regions in all three rare-earth-based specimens (see Fig. 4.18), it certainly requires more work to unambiguously determine the orientation relationships of the nanocrystals.

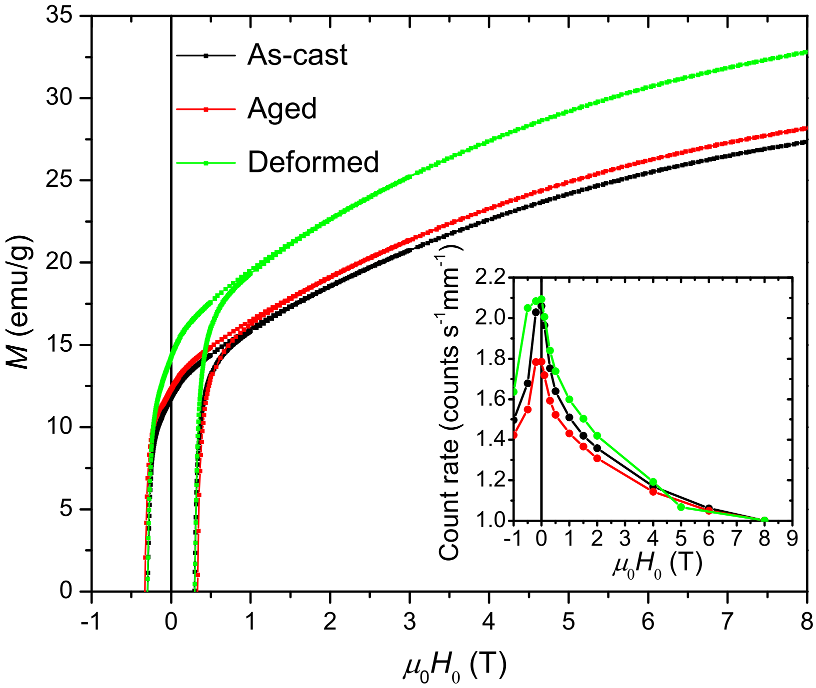

Fig. 4.9 Room-temperature magnetization curves of as-cast, aged, and deformed $(Nd_{60}Fe_{30}Al_{10})_{92}Ni_8$ (only the upper quadrants are shown). Inset shows the field dependence of the neutron count rate of the samples normalized by the respective sample thickness. Measured q-range for the count rate is $0.035\,\mathrm{nm}^{-1} \lesssim q \lesssim 0.3\,\mathrm{nm}^{-1}$.

The total unpolarized scattering cross section of the hard magnetic BMG sample was measured in the magnetic field range up to 8 T (see Figs. 4.10 and 4.12). In contrast to $Fe_{70}Mo_5Ni_5P_{12.5}B_{2.5}C_5$, where we observe a strong field dependency of $d\Sigma/d\Omega$ and of $d\Sigma_M/d\Omega$ by two orders of magnitude (see Fig. 4.5), the Nd-containing samples exhibit only a weak dependency of $d\Sigma/d\Omega$ on the applied magnetic field. The two-dimensional total scattering cross sections are isotropic for all applied field values investigated, which is likely related to the dominance of the isotropic nuclear scattering contribution, and remain visually unchanged with decreasing magnetic field. On the other hand, when the scattering at the largest field of 8 T is subtracted from the data at lower fields, the resulting spin-misalignment scattering cross section $d\Sigma_M/d\Omega$ (see Fig. 4.11) is highly anisotropic. With the field decreasing from 8 T, $d\Sigma_M/d\Omega$ exhibits an angular anisotropy which contains contributions due to a $\cos^2\theta$ term (giving rise to a horizontally-elongated pattern) and due to a $\sin^2\theta\cos^2\theta$ type term (yielding maxima roughly along the diagonals of the detector). With

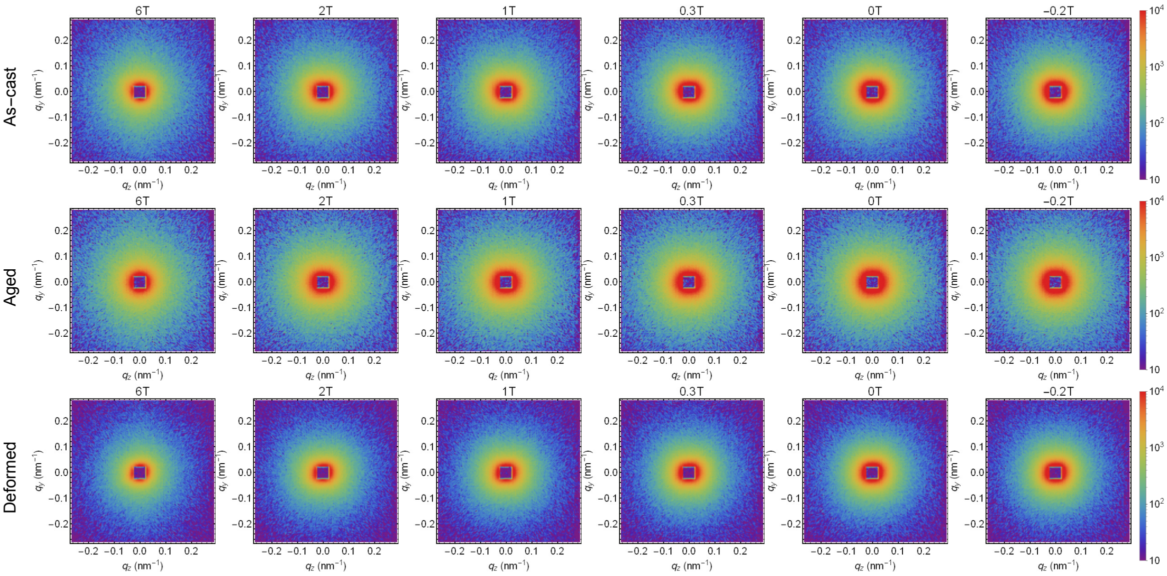

Fig. 4.10 Unpolarized total $\mathrm{d}\Sigma/\mathrm{d}\Omega$ of as-cast, aged, and deformed $(\mathrm{Nd}_{60}\mathrm{Fe}_{30}\mathrm{Al}_{10})_{92}\mathrm{Ni}_{8}$ at selected applied magnetic fields (logarithmic color scale). $\mathbf{H}_0$ is horizontal in the plane.

reference to the theoretical expressions for the spin-misalignment SANS cross section from Eqs. (2.68)−(2.72), this suggests that in the hard magnetic BMG scattering contributions due to spatially fluctuating saturation magnetization (*cf.* the angular anisotropy of the response function R_M from Eq. (2.72)) play a significant role. This is in contrast to the soft magnetic BMG, where we have found that the term $S_M R_M$ is negligible and $\mathrm{d}\Sigma_M/\mathrm{d}\Omega$ is dominated by $S_H R_H$.

The asymptotic power-law exponent n of the total measured SANS cross-section, $\mathrm{d}\Sigma/\mathrm{d}\Omega \propto q^{-n}$, is frequently discussed in the literature. For particles with sharp interfaces, both $\widetilde{H}_p^2(q)$ and $\widetilde{M}_z^2(q)$ vary asymptotically as q^{-4} [103], as does the function H_{eff}^{-2} (compare Eq. (2.23)). Taking into account that then $R_H \propto q^{-4}$ and $R_M \propto q^{-2}$, it is readily verified that the anisotropy-field contribution to $\mathrm{d}\Sigma_M/\mathrm{d}\Omega$ varies as $S_H R_H \propto q^{-8}$, whereas $S_M R_M \propto q^{-6}$. Therefore, depending on the relative magnitude of both contributions to $\mathrm{d}\Sigma_M/\mathrm{d}\Omega$, it is possible to observe different asymptotic power-law exponents of $\mathrm{d}\Sigma_M/\mathrm{d}\Omega$ and, hence, of $\mathrm{d}\Sigma/\mathrm{d}\Omega$. However, an important difference between conventional (nano)crystalline ferromagnets and magnetic BMGs relates to the characteristic length scales over which perturbations in the magnetic anisotropy field and in the saturation magnetization manifest: while in nanocrystalline systems H_p and M_s typically vary on a scale of the grain size, say, 10 nm, in magnetic BMGs this length scale is defined by the interatomic distance due to atomic-site anisotropy and randomness. As a consequence, the functions $S_H(q)$ and $S_M(q)$ are almost constant for magnetic BMGs (i.e., q-independent) over a large part of the experimentally accessible range of momentum transfers ($0.01 \lesssim q \lesssim 1.0\,\mathrm{nm}^{-1}$). Therefore, the asymptotic power-law dependence of the spin-misalignment scattering cross section $d\Sigma_M/d\Omega = S_H R_H + S_M R_M$ is determined by the asymptotic behavior of both response functions, $R_H \propto q^{-4}$ and $R_M \propto q^{-2}$, in other words, $d\Sigma_M/d\Omega \propto q^{-n}$ with $2 < n < 4$. The results for the field-dependent exponent n obtained from the fit of $d\Sigma/d\Omega$ shown in Fig. 4.13 seem to confirm this prediction. On the left in Fig. 4.13, power-law exponent n in $d\Sigma_M/d\Omega = K/q^n$ is plotted as a function of applied magnetic field, and the parts of the scattering curve $d\Sigma_M/d\Omega(q)$ used for the fit are shown on the right in Fig. 4.13.

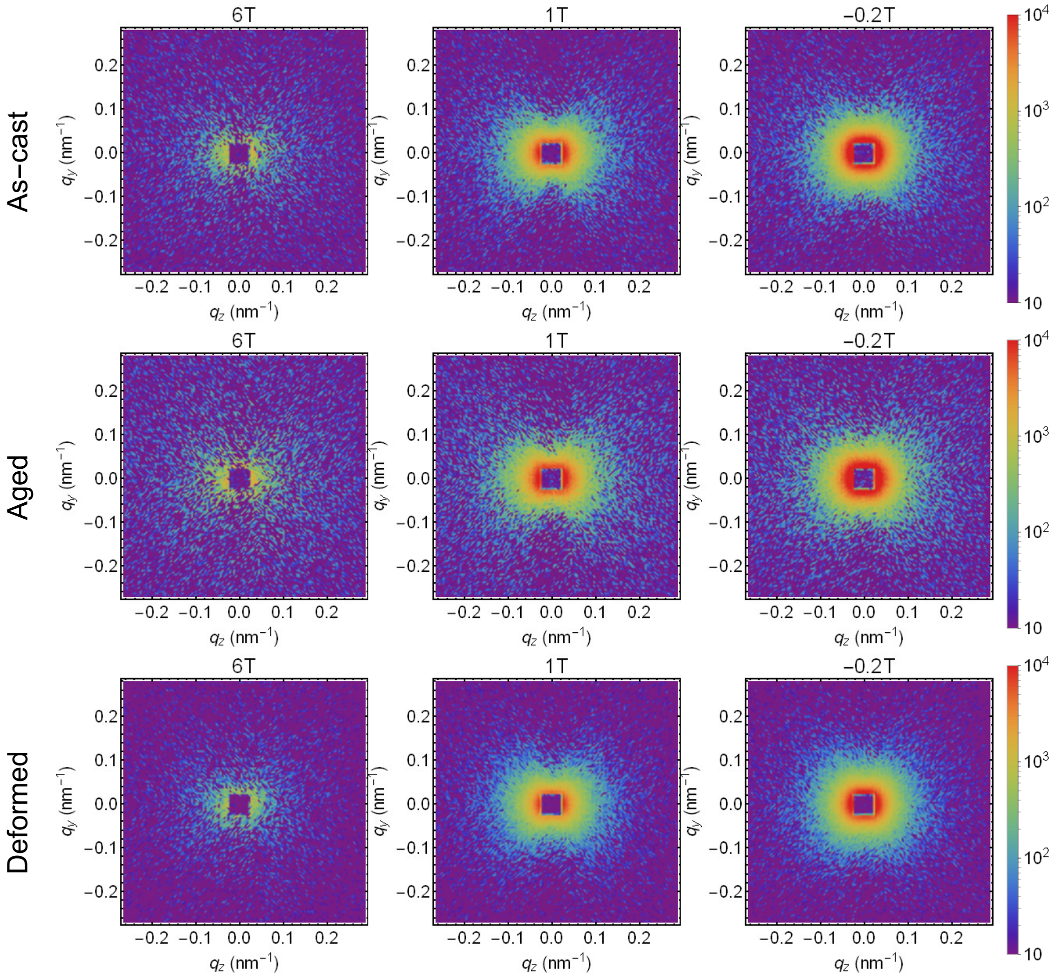

Fig. 4.11 Comparison of the two-dimensional spin-misalignment SANS cross sections $d\Sigma_M/d\Omega$ of as-cast, aged, and deformed $(Nd_{60}Fe_{30}Al_{10})_{92}Ni_8$ at selected applied magnetic fields (logarithmic color scale). $d\Sigma/d\Omega$ at 8 T has been subtracted from each data set. $\mathbf{H}_0$ is aligned horizontally.

The anisotropic $d\Sigma_M/d\Omega$ translate into predominantly vertically-aligned correlation functions $c(y,z)$ (see Fig. 4.15); this is in agreement with the notion of spin-misalignment scattering originating from spin perturbations evolving in the plane perpendicular to the applied magnetic field. As an example, we display in Fig. 4.16 the field dependence of the azimuthally-averaged correlation function of the deformed BMG sample. Increasing the field suppresses the amplitude as well as the range of gradients in the magnetic microstructure. The corresponding field-dependent correlation lengths of all hard magnetic BMG are shown in Fig. 4.17. The difference in l_C between as-cast, aged, and deformed $(\mathrm{Nd}_{60}\mathrm{Fe}_{30}\mathrm{Al}_{10})_{92}\mathrm{Ni}_8$ is only of the order of $2-3\,\mathrm{nm}$; with the field decreasing from $6\,\mathrm{T}$ to the coercive field $\mu_0 H_c \sim -0.3\,\mathrm{T}$, the l_C values increase from $\sim 20\,\mathrm{nm}$ towards a maximum of $\sim 45\,\mathrm{nm}$, respectively. The observation that the largest field dependencies of $\mathrm{d}\Sigma/\mathrm{d}\Omega$ and $\mathrm{d}\Sigma_M/\mathrm{d}\Omega$ are concentrated at the smallest q (see Figs. 4.12 and 4.14) indicates that significant magnetic scattering contributions originate from large-scale structures, which in future experiments may be probed by means of ultra small-angle neutron scattering.

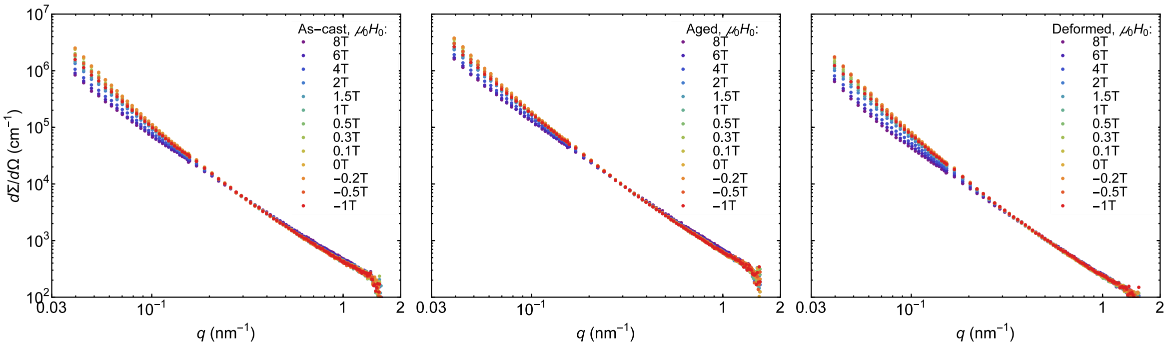

Fig. 4.12 Azimuthally-averaged total $\mathrm{d}\Sigma/\mathrm{d}\Omega$ of as-cast, aged, and deformed $(\mathrm{Nd}_{60}\mathrm{Fe}_{30}\mathrm{Al}_{10})_{92}\mathrm{Ni}_8$ at selected applied magnetic fields (see insets, log-log scale).

While the magnetization data (Fig. 4.9) show a strong dependency on the thermal and mechanical treatment, the SANS data (Figs. 4.11 and 4.17) are very similar for the as-cast, aged, and deformed states. This suggests that the microstructural changes which are responsible for $M(H_0)$ are not resolved by the SANS experiment (given the experimental q_{min} and q_{max}), which probes a real-space structure between about $1-100\,\mathrm{nm}$; however, this observation does not imply that SANS is not suitable for resolving displacement fields in magnetic BMG in the given q-range. In this context we refer to a recent SANS study which investigates the effect of the annealing conditions (heating rate and temperature) on the magnetic microstructure of sintered Nd-Fe-B magnets [131]; while the temperature treatment has a strong effect on the coercivity (reduction by about 50 % on annealing), the associated changes in the microstructure do surprisingly not show up (or at best only very weakly) in the neutron-scattering signal.

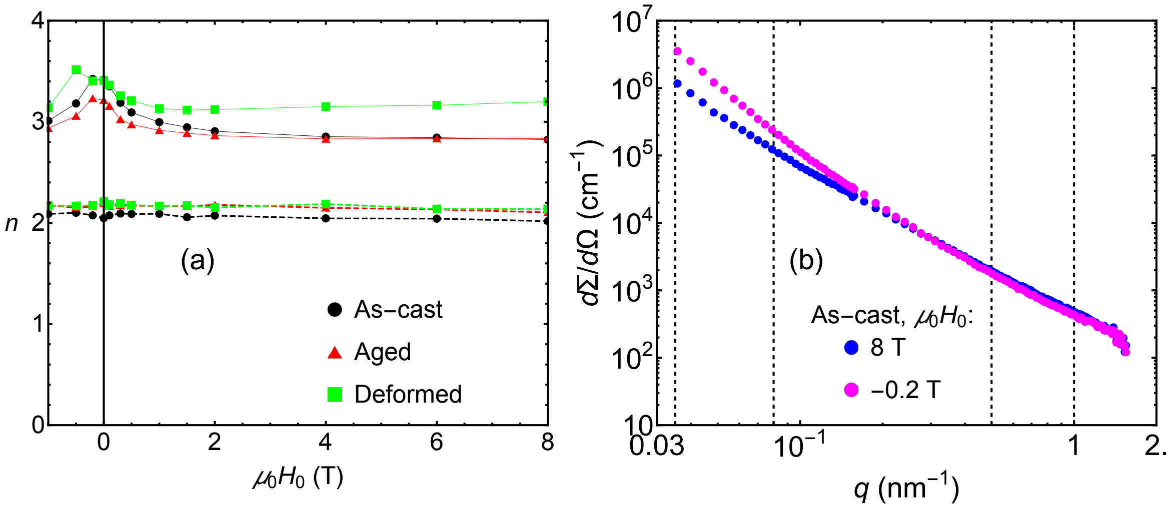

Fig. 4.13 (a) Field dependence of the power-law exponent n in $\mathrm{d}\Sigma/\mathrm{d}\Omega = K/q^n$ for the total $\mathrm{d}\Sigma/\mathrm{d}\Omega$ of as-cast, aged, and deformed $(\mathrm{Nd}_{60}\mathrm{Fe}_{30}\mathrm{Al}_{10})_{92}\mathrm{Ni}_8$. The dashed lines in (b) indicate the respective low-q and high-q ranges over which the fit was carried out. Solid (dashed) connecting lines in (a) correspond to the low-q (high-q) region.

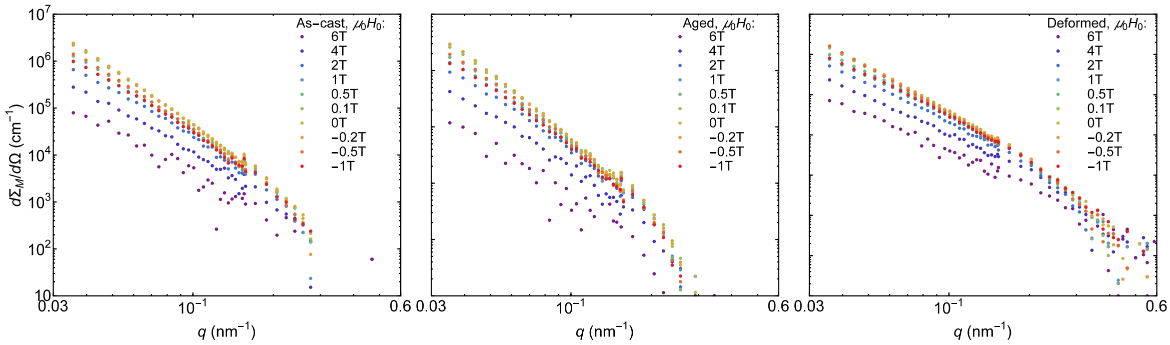

Fig. 4.14 Azimuthally-averaged spin-misalignment $\mathrm{d}\Sigma_M/\mathrm{d}\Omega$ of as-cast, aged, and deformed $(\mathrm{Nd}_{60}\mathrm{Fe}_{30}\mathrm{Al}_{10})_{92}\mathrm{Ni}_8$ at selected applied magnetic fields (see insets, log-log scale).

4.2 Dzyaloshinski-Moriya interaction in bulk textured ferromagnetic samples

Figure 4.19 demonstrates the effect of small grain size (large defect density) on the magnetization of Tb. At 14 T, the magnetization of 21 nm-sized Tb is reduced by $\sim 10\%$ relative to the coarse-grained specimen. This is a well-known effect, and for nanocrystalline Gd it could be shown that the magnetization reduction scales with the inverse grain size [116].

In order to observe the effect of DM interaction on spin-misalignment SANS, as it was suggested in Section 2.4.2, we have measured the difference between SANSPOL cross sections $\mathrm{d}\Sigma^+/\mathrm{d}\Omega$ and $\mathrm{d}\Sigma^-/\mathrm{d}\Omega$ for nanocrystalline Tb and for cold-rolled Co. Based on the

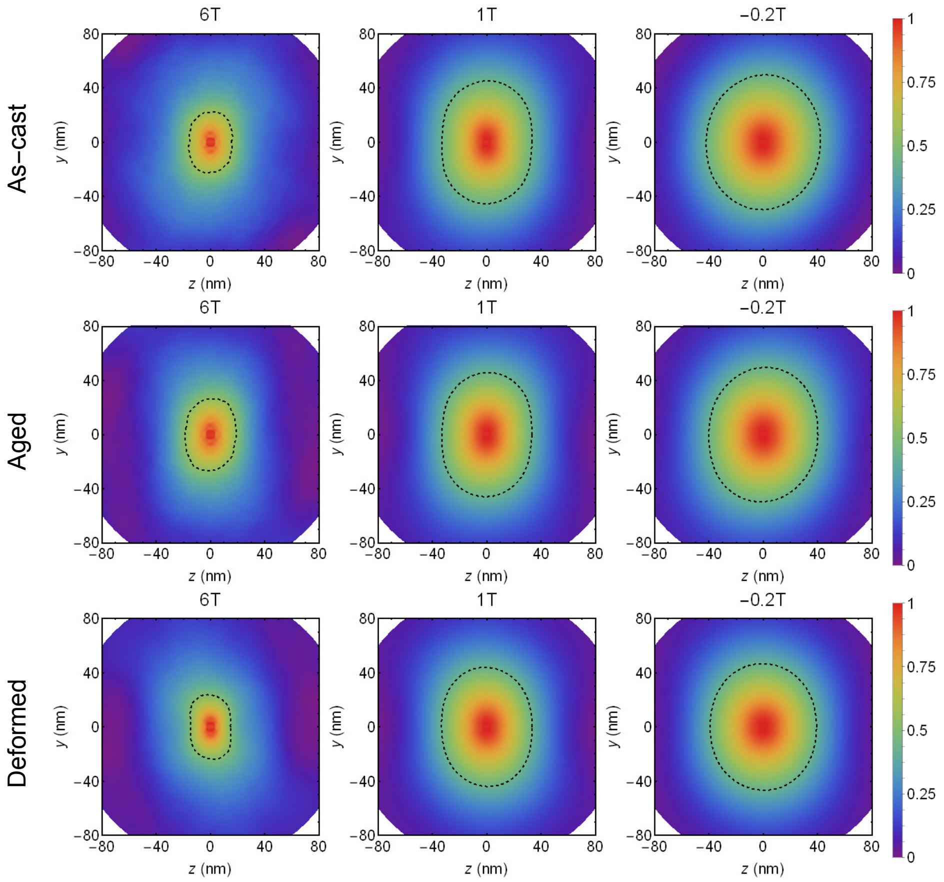

Fig. 4.15 Field dependence of the two-dimensional (normalized) correlation functions $c(y,z)$ of as-cast, aged, and deformed $(\mathrm{Nd}_{60}\mathrm{Fe}_{30}\mathrm{Al}_{10})_{92}\mathrm{Ni}_{8}$ at selected applied magnetic fields (see insets). $\mathbf{H}_0$ is horizontal in the plane. Dashed contour lines: $c(y,z) = \exp(-1)$.

expressions from Section 2.4, this difference reads:

$$\mathrm{d}\Sigma^{+}/\mathrm{d}\Omega - \mathrm{d}\Sigma^{-}/\mathrm{d}\Omega = 2\frac{8\pi^3}{V}b_H^2\left(b_H^{-1}(\widetilde{N}\widetilde{M}_z^{\star} + \widetilde{N}^{\star}\widetilde{M}_z)\sin^2\theta + i\chi(\mathbf{q})\right), \tag{4.1}$$

with the chiral function $\chi(\mathbf{q})$ given by:

$$\chi(\mathbf{q}) = (\widetilde{M}_x^{\star}\widetilde{M}_y - \widetilde{M}_x\widetilde{M}_y^{\star})\cos^2\theta - (\widetilde{M}_x^{\star}\widetilde{M}_z - \widetilde{M}_x\widetilde{M}_z^{\star})\sin\theta\cos\theta. \tag{4.2}$$

Figure 4.20 depicts the difference $\mathrm{d}\Sigma^{+}/\mathrm{d}\Omega - \mathrm{d}\Sigma^{-}/\mathrm{d}\Omega$ for the nanocrystalline Tb at field-cooled state measured in 5 T field at 100 K. The field-cooled state means that the sample was cooled in 5 T field from the room temperature (where the sample is in a paramagnetic state) down below the Curie temperature ($T_C \cong 220K$ [132]) to 100 K (where the sample is in a ferromagnetic state). Such procedure was expected to result in a kind of magnetic

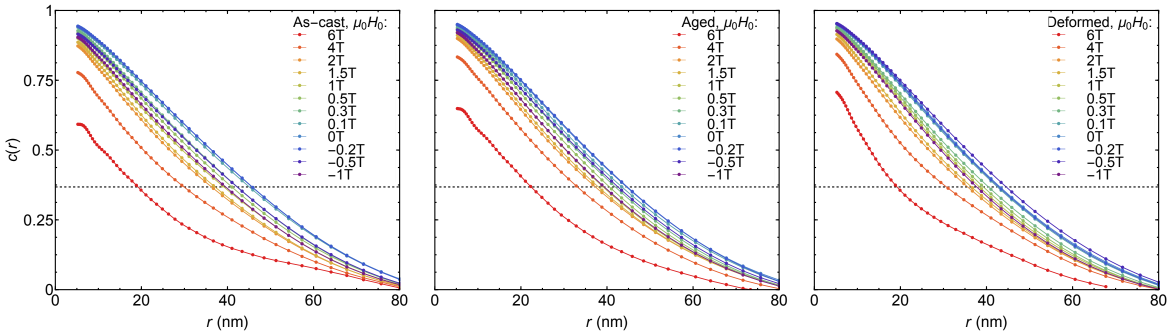

Fig. 4.16 Azimuthally-averaged correlation function $c(r)$ of as-cast, aged, and deformed $(\mathrm{Nd}_{60}\mathrm{Fe}_{30}\mathrm{Al}_{10})_{92}\mathrm{Ni}_{8}$ at selected applied magnetic fields (see insets). Dashed horizontal line: $c(r) = \exp(-1)$. Note that the $C(r)$ were obtained by azimuthally averaging the two-dimensional correlation functions (which were computed according to Eq. (2.101)).

texture of the magnetic moments in the vicinity of defects in the sample. The expression from Eq. (4.1) may be split into two terms: first has a $\sin^2\theta$ symmetry and takes positive values at any θ (we remind that $\widetilde{N}$ and $\widetilde{M}_z$ are assumed to be real and isotropic functions of q); while the second (chiral) term can take both positive and negative values depending on θ. Comparing the data shown in Fig. 4.20, we see that a $\sin^2\theta$-type anisotropy dominates at low-q, while an asymmetry is indeed clearly visible at the larger momentum transfers. The asymmetry, which is also weakly visible in low-q data, is most pronounced along the horizontal direction, which by comparison to the theoretical prediction (*cf.* Eq. (2.129)) can be attributed to the anisotropy-field term $\propto H_p^2$. This is in agreement with the expectation, since Tb is an extremely anisotropic material, with a first-order uniaxial magnetocrystalline anisotropy constant of $\sim 3.5 \cdot 10^7 \mathrm{J\,m^{-3}}$ at 100 K [133].

Figure 4.21 depicts the difference $\mathrm{d}\Sigma^+/\mathrm{d}\Omega - \mathrm{d}\Sigma^-/\mathrm{d}\Omega$ for the cold-rolled Co measured in 0.5 T (right figure) and 2 T (left figure) fields at 300 K. The data measured at 2 T show a $\sin^2\theta$-type anisotropy, which is related to the fact that transversal Fourier components of magnetization $\widetilde{M}_x$ and $\widetilde{M}_y$ vanish at magnetic saturation. Data measured at 0.5 T do indicate an anisotropy which can be attributed to the chiral term from Eq. (4.2). Note that the scattering for both fields is concentrated at very small values of momentum vector.

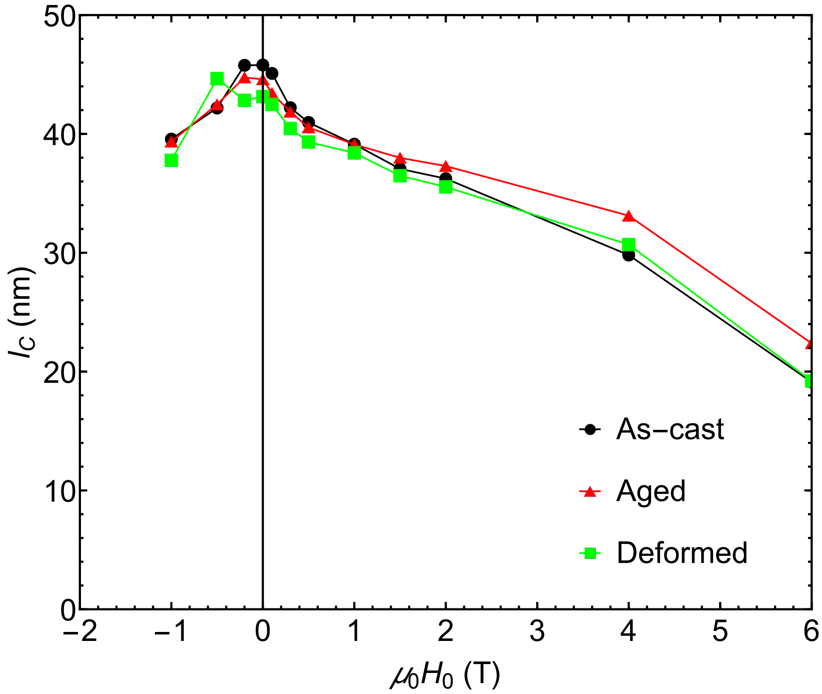

Fig. 4.17 Field dependence of the correlation length l_C of as-cast, aged, and deformed $(Nd_{60}Fe_{30}Al_{10})_{92}Ni_8$ (lines are guides to the eyes). The l_C were computed using the $C(r)$ data displayed in Fig. 4.16.

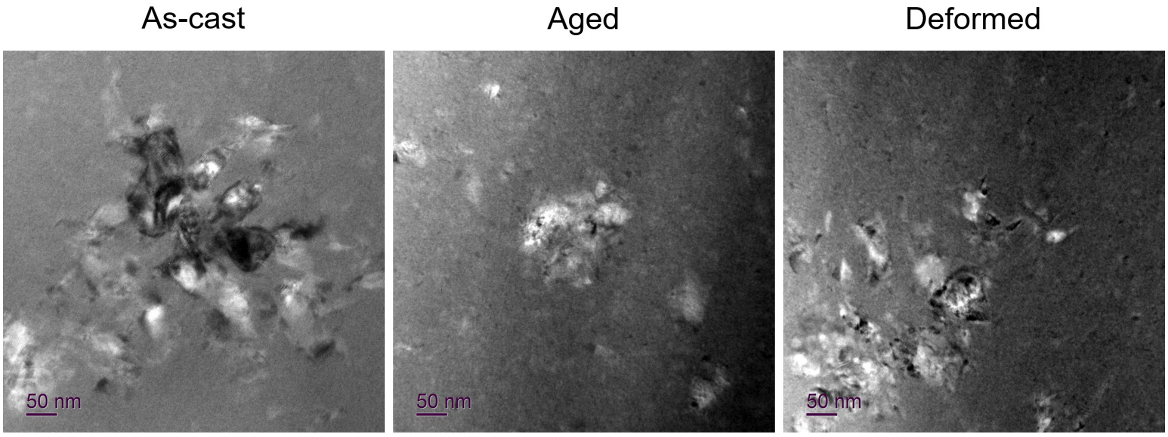

Fig. 4.18 TEM micrographs of as-cast, aged, and deformed $(Nd_{60}Fe_{30}Al_{10})_{92}Ni_8$.

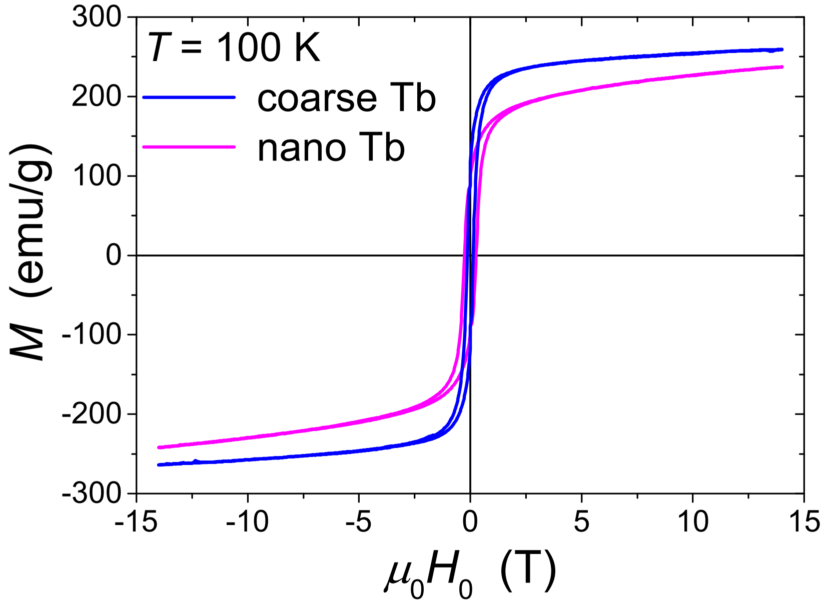

Fig. 4.19 Magnetization curves of nanocrystalline and coarse-grained terbium measured at 100 K. Both samples were initially cooled down from 300 K at zero magnetic field.

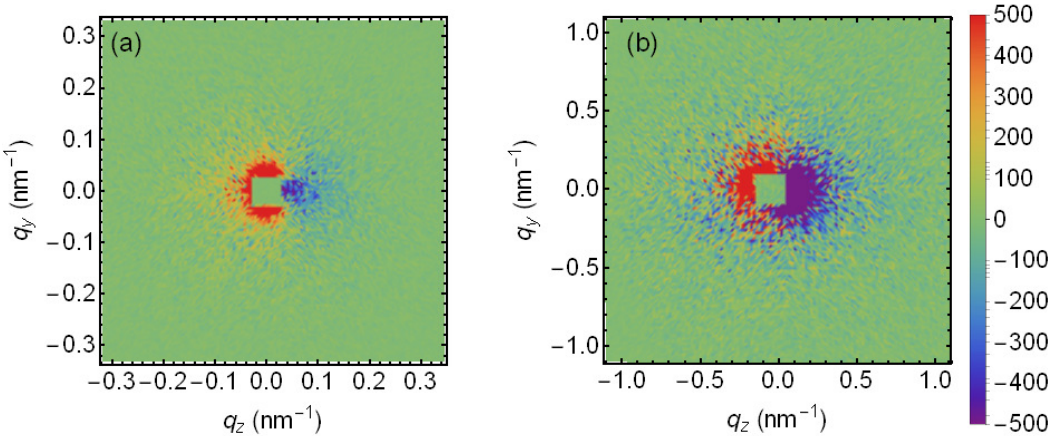

Fig. 4.20 Difference between SANSPOL cross sections $d\Sigma^+/d\Omega - d\Sigma^-/d\Omega$ of nanocrystalline Terbium at field-cooled state, measured at 100 K in the magnetic field of 5 T. $\mathbf{H}_0$ is horizontal in the plane. (a) low-q data; (b) high-q data.

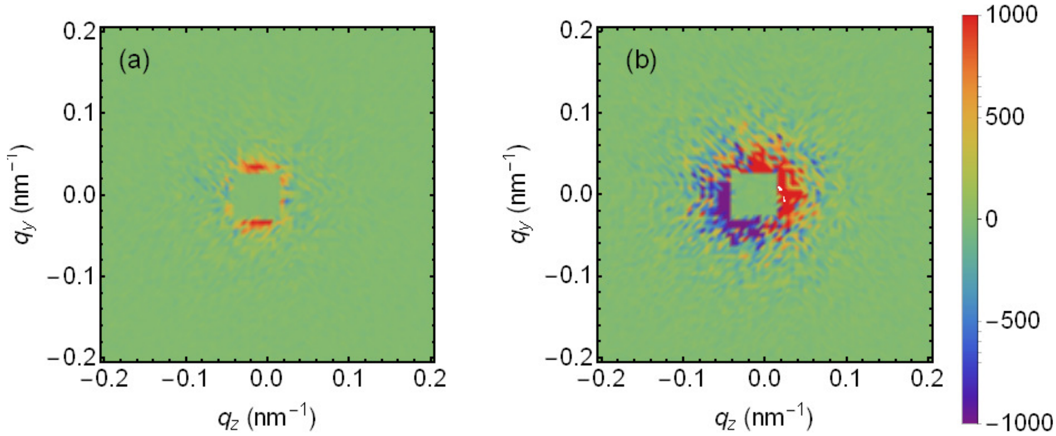

Fig. 4.21 Difference between SANSPOL cross sections $d\Sigma^+/d\Omega - d\Sigma^-/d\Omega$ of cold-rolled Co (the deformation direction is horizontal) measured at 300 K: (a) in the magnetic field 2 T (at magnetic saturation); (b) in the magnetic field 0.5 T (below magnetic saturation). $\mathbf{H}_0$ is horizontal in the plane.

Chapter 5

Summary, Conclusions, and Outlook

We would like to remind that the present thesis is devoted to the exploration of the use of the magnetic small-angle neutron scattering (SANS) technique for analyzing the magnetic microstructure of bulk magnetic materials. The main emphasis of the work is on the following: (i) effect of mechanical deformation on the magnetic microstructure of bulk metallic glasses; (ii) theoretical investigation of the predictions of a recent magnetic SANS theory into real space; (iii) study of the impact of the Dzyaloshinski-Moriya (DM) interaction on the magnetic microstructure and magnetic SANS cross section of bulk ferromagnets.

5.1 Summary and Conclusions

We have investigated the magnetic microstructure of soft magnetic $Fe_{70}Mo_5Ni_5P_{12.5}B_{2.5}C_5$ and hard magnetic $(Nd_{60}Fe_{30}Al_{10})_{92}Ni_8$ bulk metallic glasses (BMG) in the as-prepared, aged, and mechanically-deformed state by means of magnetic SANS. For both sets of samples, the results from the magnetization measurements are not in complete correspondence with the results from the SANS measurements: *e.g.* while the magnetization of soft magnetic BMG does not differ much between the samples, the field dependence of the SANS cross section is qualitatively different. Based on the analysis of the SANS cross section in terms of the correlation function of the spin misalignment, we could estimate the characteristic length scale l_C, which provides a measure for the size of nonuniformly magnetized regions. For both sets of samples, we find magnetic-field-dependent l_C-values of the order of several tens of nanometers. From the comparison of the experimentally observed angular anisotropy of the SANS cross section to theoretical predictions, we conclude that the magnetic microstructure of the soft magnetic BMG is dominated by magnetic anisotropy-field-related perturbations, while the mesoscale spin structure of the hard magnetic BMG is significantly influenced by magnetostatic fluctuations. For the rare-earth-containing deformed BMG, we observe an unusual increase of the high-field magnetization ($\sim 20\,\%$ at 8 T), which deserves further investigation.

On the basis of a recent micromagnetic theory for the magnetic SANS cross section of inhomogeneous bulk ferromagnets, we have studied the corresponding magnetic field-dependent spin-misalignment correlations in real space. The correlation function $c(r)$ of the spin-misalignment SANS cross section depends on the applied magnetic field and, for $\mathbf{k}_0 \perp \mathbf{H}_0$, on the ratio of magnetic anisotropy field strength H_p to magnetization jump ΔM at internal interfaces. Additional degrees of freedom in $c(r)$ studied in the present work relate to the particle (anisotropy-field) form factor or to the inclusion of interparticle correlations via a structure factor. It was shown that, in the non-dilute case, increasing of the particle volume fraction strongly affects the behavior of the correlation function and, correspondingly, of the correlation length. The result for $c(r)$ (for $\mathbf{k}_0 \perp \mathbf{H}_0$) from Eq. (2.96) demonstrates a strong impact of $H_p/\Delta M$ on the shape and range of the correlations: magnetostatically dominated correlations ($H_p/\Delta M \ll 1$) decay on a rather short length scale, whereas anisotropy-field-dominated correlations ($H_p/\Delta M \gg 1$) are characterized by a long-range decay, which is reasonably described by Eq. (2.104). Additionally, the difference between various definitions of the correlation function was studied. It was shown that, in the micromagnetics approach, the difference between the autocorrelation function of the spin misalignment and the correlation function of spin-misalignment SANS cross section based on Eq. (2.96) is only minor, whereas the difference between the autocorrelation function and the averaged two-dimensional correlation function based on Eq. (2.101) may not be neglected for low fields. Experimental data for the correlation function of the spin-misalignment SANS cross sections of nanocrystalline Co and Ni have been successfully analyzed using the presented theoretical expressions, and the material parameters obtained from the analysis are close to the ones from the literature.

Within the framework of the continuum theory of micromagnetics, we have investigated the influence of the Dzyaloshinski-Moriya interaction on the elastic magnetic SANS cross section of bulk ferromagnets. This effect was predicted to show up in the samples with a large density of the defects, like field-cooled nanocrystalline rare-earth magnets or heavily cold-worked magnetic materials. Due to the complex character of the magnetization Fourier components, a polarization dependence of the spin-flip SANS cross section is expected. The presence of the effect was studied on field-cooled nanocrystalline Tb and heavily cold-rolled Co. For both samples, we observed the predicted anisotropy in the polarized SANS cross section, which may indeed indicate the presence of the DM interaction-effect on the elastic magnetic SANS.

5.2 Outlook

We were not able in our feasibility study to resolve the nature of displacement fields generated by mechanical loading in magnetic BMG. Nevertheless, the way seems paved for eventually elucidating this important question by employing the spin degree of freedom of a magnetic material for decorating the displacement field. In order to solve this issue, we suggest the following approaches: (i) Future neutron work will concentrate on the *in-situ* observation of the magnetic SANS cross section as a function of shear and/or tensile stress by analyzing the difference between loaded and unloaded states; this provides a means to disentangle spin-misalignment scattering due to spatial variations in the saturation magnetization from the strain-field-related scattering, which both result in clover-leaf-type angular anisotropies with maxima along the detector diagonals. (ii) By combining conventional small-angle neutron scattering with ultra small-angle neutron scattering one will be able to access smaller momentum transfers and, hence, important missing information hidden by the beamstop in the conventional technique can be extracted. Likewise, the aid of polarized neutrons enables to separate the nuclear coherent from the relevant magnetic scattering cross section. For the rare-earth-containing deformed BMG, the observed unusual increase of the high-field magnetization deserves further investigation. We suggest studying how this effect depends on the elemental composition and the applied stress value, together with the further study of the sample microstructure.

As the correlation function is concerned, it would also be of interest to employ the present approach for studying long-range magnetic correlations, as accessible on a USANS instrument [134], or the magnetic microstructure of state-of-the-art nanocrystalline Nd-Fe-B-based permanent magnets [100, 135–137].

While the presented results may indeed indicate the presence of the DM interaction effect on the elastic magnetic SANS in the field-cooled nanocrystalline Tb and heavily cold-rolled Co samples, there is no doubt that further experimental studies are necessary. First, the presented results for nanocrystalline Tb should be compared to the results for coarse-grained Tb sample (under the same experimental conditions). The coarse-grained Tb sample is not expected to show the effect of DM interaction on the magnetic SANS, and that would support the conclusions from the presented work. Additionally, it should be studied how the effect depends on the experimental conditions such as applied magnetic field value, sample temperature, *etc*. It is possible to fit the experimental data with the theoretical expressions presented in Section 2.4.2 - that would allow extracting the material parameters such as the effective DM interaction constant D. For the Co sample, it may be advisable to go for a scattering technique with a smaller accessible momentum vector q range, such as a USANS instrument.

List of publications

[1] É.A. Périgo, I. Titov, R. Weber, D. Mettus, I. Peral, O. Vallcorba, D. Honecker, A. Feoktystov, and A. Michels. **Effect of annealing conditions on the microstructure and magnetic properties of sintered Nd-Fe-B magnets as seen by magnetic SANS**. *Mater. Res. Express*, 5:036110 2018.

[2] D. Mettus, M. Deckarm, A. Leibner, R. Birringer, M. Stolpe, R. Busch, D. Honecker, J. Kohlbrecher, P. Hautle, N. Niketic, J. Rodriguez Férnandez, L. Férnandez Barquin, and A. Michels. **Magnetic small-angle neutron scattering on bulk metallic glasses: A feasibility study for imaging displacement fields**. *Phys. Rev. Mat.*, 1:074403, 2017.

[3] A. Michels, R. Weber, I. Titov, D. Mettus, E. Périgo, I. Peral, O. Vallcorba, J. Kohlbrecher, K. Suzuki, M. Ito, A. Kato, and M. Yano. **Spin structures of textured and isotropic Nd-Fe-B-based nanocomposites: Evidence for correlated crystallographic and spin textures.** *Phys. Rev. Appl.*, 7:024009, 2017.

[4] A. Michels, D. Mettus, D. Honecker, and K. Metlov. **Effect of Dzyaloshinski-Moriya interaction on elastic small-angle neutron scattering.** *Phys. Rev. B*, 94:054424, 2016.

[5] E. Périgo, D. Mettus, E. Gilbert, P. Hautle, N. Niketic, B. van den Brandt, J. Kohlbrecher, P. McGuiness, Z. Fu, and A. Michels. **Magnetic microstructure of a textured Nd-Fe-B sintered magnet characterized by small-angle neutron scattering**. *J. Alloys Comp.*, 661:110–114, 2015.

[6] D. Mettus and A. Michels. **Small-angle neutron scattering correlation functions of bulk magnetic materials.** *J. Appl. Cryst.*, 48:1437–1450, 2015.

References

[1] C. A. Schuh, T. C. Hufnagel, and U. Ramamurty, Acta Mater. **55**, 4067 (2007).

[2] Q. Luo and W. H. Wang, J. Non-Cryst. Solids **355**, 759 (2009).

[3] C. Suryanarayana and A. Inoue, International Materials Reviews **58**, 131 (2013).

[4] T. C. Hufnagel, C. A. Schuh, and M. L. Falk, Acta Mater. **109**, 375 (2016).

[5] W. Wang, C. Dong, and C. Shek, J. MSER **44**, 45 (2004).

[6] A. R. Hinkle, C. H. Rycroft, M. D. Shields, and M. L. Falk, Phys. Rev. E **95**, 053001 (2017).

[7] R. Dasgupta, H. G. E. Hentschel, and I. Procaccia, Phys. Rev. Lett. **109**, 255502 (2012).

[8] R. Dasgupta, H. G. E. Hentschel, and I. Procaccia, Phys. Rev. E **87**, 022810 (2013).

[9] K. E. Jensen, D. A. Weitz, and F. Spaepen, Phys. Rev. E **90**, 042305 (2014).

[10] H. Kronmüller, A. Seeger, and M. Wilkens, Z. Phys. **171**, 291 (1963).

[11] G. Göltz, H. Kronmüller, A. Seeger, H. Scheuer, and W. Schmatz, Philos. Mag. A **54**, 213 (1986).

[12] W. F. Brown Jr., Phys. Rev. **58**, 736 (1940).

[13] A. Michels, J. Phys.: Condens. Matter **26**, 383201 (2014).

[14] O. Glatter, J. Appl. Crystallogr. **10**, 415 (1977).

[15] S. Hansen, J. Appl. Crystallogr. **33**, 1415 (2000).

[16] G. Fritz and O. Glatter, J. Phys.: Condens. Matter **18**, S2403 (2006).

[17] S. Hansen, (2012), *Estimation of distribution functions from small-angle scattering data*.

[18] G. Fritz-Popovski, J. Appl. Cryst. **46**, 1447 (2013).

[19] G. Fritz-Popovski, J. Appl. Cryst. **48**, 44 (2015).

[20] D. I. Svergun and M. H. J. Koch, Rep. Prog. Phys. **66**, 1735 (2003).

[21] K. Mortensen and J. S. Pedersen, Macromolecules **26**, 805 (1993).

[22] U. Lembke, A. Hoell, R. Kranold, R. Müller, W. Schüppel, G. Goerigk, R. Gilles, and A. Wiedenmann, J. Appl. Phys. **85**, 2279 (1999).

[23] B. A. Frandsen, X. Yang, and S. J. L. Billinge, Acta Cryst. A **70**, 3 (2014).

[24] D. Honecker and A. Michels, Phys. Rev. B **87**, 224426 (2013).

[25] D. Honecker, C. D. Dewhurst, K. Suzuki, S. Erokhin, and A. Michels, Phys. Rev. B **88**, 094428 (2013).

[26] W. F. Brown Jr., *Micromagnetics* (Interscience Publishers, New York, 1963).

[27] I. Dzyaloshinsky, J. Phys. Chem. Solids **4**, 241 (1958).

[28] T. Moriya, Phys. Rev. **120**, 91 (1960).

[29] A. N. Bogdanov and D. A. Yablonskii, Sov. Phys. JETP **68**, 101 (1989).

[30] A. Bogdanov and A. Hubert, J. Magn. Magn. Mater. **138**, 255 (1994).

[31] A. N. Bogdanov, U. K. Rössler, and C. Pfleiderer, Physica B **359-361**, 1162 (2005).

[32] U. K. Rößler, A. N. Bogdanov, and C. Pfleiderer, Nature **442**, 797 (2006).

[33] B. Binz, A. Vishwanath, and V. Aji, Phys. Rev. Lett. **96**, 207202 (2006).

[34] M. Bode, M. Heide, K. von Bergmann, P. Ferriani, S. Heinze, G. Bihlmayer, A. Kubetzka, O. Pietzsch, S. Blügel, and R. Wiesendanger, Nature **447**, 190 (2007).

[35] Y. Yamasaki, H. Sagayama, T. Goto, M. Matsuura, K. Hirota, T. Arima, and Y. Tokura, Phys. Rev. Lett. **98**, 147204 (2007).

[36] S. Mühlbauer, B. Binz, F. Jonietz, C. Pfleiderer, A. Rosch, A. Neubauer, R. Georgii, and P. Böni, Science **323**, 915 (2009).

[37] C. Pfleiderer, T. Adams, A. Bauer, W. Biberacher, B. Binz, F. Birkelbach, P. Böni, C. Franz, R. Georgii, M. Janoschek, F. Jonietz, T. Keller, R. Ritz, S. Mühlbauer, W. Münzer, A. Neubauer, B. Pedersen, and A. Rosch, J. Phys.: Condens. Matter **22**, 164207 (2010).

[38] S. Heinze, K. von Bergmann, M. Menzel, J. Brede, A. Kubetzka, R. Wiesendanger, G. Bihlmayer, and S. Blügel, Nat. Phys. **7**, 713 (2011).

[39] N. Kanazawa, J.-H. Kim, D. S. Inosov, J. S. White, N. Egetenmeyer, J. L. Gavilano, S. Ishiwata, Y. Onose, T. Arima, B. Keimer, and Y. Tokura, Phys. Rev. B **86**, 134425 (2012).

[40] P. Milde, D. K¨öhler, J. Seidel, L. M. Eng, A. Bauer, A. Chacon, J. Kindervater, S. Mühlbauer, C. Pfleiderer, S. Buhrandt, C. Schütte, and A. Rosch, Science **340**, 1076 (2013).

[41] A. Fert, V. Cros, and J. Sampaio, Nat. Nanotechnol. **8**, 152 (2013).

[42] S. Rohart and A. Thiaville, Phys. Rev. B **88**, 184422 (2013).

[43] M. Kostylev, J. Appl. Phys. **115**, 233902 (2014).

[44] M. N. Wilson, A. B. Butenko, A. N. Bogdanov, and T. L. Monchesky, Phys. Rev. B **89**, 094411 (2014).

[45] N. Romming, A. Kubetzka, C. Hanneken, K. von Bergmann, and R. Wiesendanger, Phys. Rev. Lett. **114**, 177203 (2015).

[46] F. N. Rybakov, A. B. Borisov, S. Blügel, and N. S. Kiselev, Phys. Rev. Lett. **115**, 117201 (2015).

[47] A. Arrott, J. Appl. Phys. **34**, 1108 (1963).

[48] A. Aharoni, *Introduction to the Theory of Ferromagnetism*, 2nd ed. (Clarendon Press, Oxford, 1996).

[49] H. Kronmüller and M. Fähnle, *Micromagnetism and the Microstructure of Ferromagnetic Solids* (Cambridge University Press, Cambridge, 2003).

[50] R. M. Moon, T. Riste, and W. C. Koehler, Phys. Rev. **181**, 920 (1969).

[51] D. Honecker, A. Ferdinand, F. Döbrich, C. D. Dewhurst, A. Wiedenmann, C. Gómez-Polo, K. Suzuki, and A. Michels, Eur. Phys. J. B **76**, 209 (2010).

[52] B. G. Ueland, J. W. Lynn, M. Laver, Y. J. Choi, and S.-W. Cheong, Phys. Rev. Lett. **104**, 147204 (2010).

[53] M. Laver, C. Mudivarthi, J. R. Cullen, A. B. Flatau, W.-C. Chen, S. M. Watson, and M. Wuttig, Phys. Rev. Lett. **105**, 027202 (2010).

[54] A. Michels, D. Honecker, F. Döbrich, C. D. Dewhurst, K. Suzuki, and A. Heinemann, Phys. Rev. B **85**, 184417 (2012).

[55] K. L. Krycka, J. A. Borchers, R. A. Booth, Y. Ijiri, K. Hasz, J. J. Rhyne, and S. A. Majetich, Phys. Rev. Lett. **113**, 147203 (2014).

[56] N. Niketic, B. van den Brandt, W. T. Wenckebach, J. Kohlbrecher, and P. Hautle, J. Appl. Cryst. **48**, 1514 (2015).

[57] W. F. Brown Jr., Rev. Mod. Phys. **17**, 15 (1945).

[58] H. Kronmüller and S. Parkin, eds., *Handbook of Magnetism and Advanced Magnetic Materials* (Wiley, Chichester, 2007) volume 2: Micromagnetism.

[59] H. Kronmüller and A. Seeger, J. Phys. Chem. Solids **18**, 93 (1961).

[60] L. Landau and E. Lifshitz, Phys. Z. Sowjetunion **8**, 153 (1935).

[61] C. Herring and C. Kittel, Phys. Rev. **81**, 869 (1951).

[62] R. Skomski, J. Phys.: Condens. Matter **15**, R841 (2003).

[63] R. Skomski and J. M. D. Coey, Phys. Rev. B **48**, 15812 (1993).

[64] J.-S. Yang and C.-R. Chang, IEEE Trans. Magn. **31**, 3602 (1995).

[65] T. Leineweber and H. Kronmüller, Phys. Status Solidi **201**, 291 (1997).

[66] C. Kittel, Rev. Mod. Phys. **21**, 541 (1949).

[67] M. S. S. Brooks and D. A. Goodings, J. Phys. C **1**, 1279 (1968).

[68] M. Colarieti-Tosti, S. I. Simak, R. Ahuja, L. Nordström, O. Eriksson, D. berg, S. Edvardsson, and M. S. S. Brooks, Phys. Rev. Lett. **91**, 157201 (2003).

[69] S. Chikazumi, *Physics of Ferromagnetism* (Clarendon Press, Oxford, 1997).

[70] K. M. Krishnan, *Fundamentals and Applications of Magnetic Materials* (Oxford University Press, Oxford, 2016).

[71] A. Aharoni, *Introduction to the Theory of Ferromagnetism*, 2nd ed. (Clarendon Press, Oxford, 1996) chapter 9.

[72] H. Kronmüller and S. Parkin, *Handbook of Magnetism and Advanced Magnetic Materials* (John Wiley & Sons, Chichester, 2007) vol.2, pp.795.

[73] E. Schlömann, J. Appl. Phys. **38**, 5027 (1967).

[74] K. L. Metlov and A. Michels, Phys. Rev. B **91**, 054404 (2015).

[75] J. Weissmüller, A. Michels, J. G. Barker, A. Wiedenmann, U. Erb, and R. D. Shull, Phys. Rev. B **63**, 214414 (2001).

[76] D. Mettus and A. Michels, Journal of Applied Crystallography **48**, 1437 (2015).

[77] J. Chadwick, Nature **129**, 312 (1932).

[78] G. L. Squires, *Introduction to the Theory of Thermal Neutron Scattering* (Dover Publications, New York, 1978).

[79] T. Brückel, G. Heger, D. Richter, G. Roth, and R. Zorn, *Neutron Scattering* (Forschungszentrum Jülich GmbH, Jülich, 2010).

[80] F. Mezei, Phys. B **137**, 295 (1986).

[81] S. V. Maleev, Phys.-Usp. **45**, 569 (2002).

[82] W. Wagner and J. Kohlbrecher, in *Modern Techniques for Characterizing Magnetic Materials*, edited by Y. Zhu (Kluwer Academic Publishers, Boston, 2005) pp. 65–105.

[83] A. Michels and J. Weissmüller, Rep. Prog. Phys. **71**, 066501 (2008).

[84] M. R. Fitzsimmons, S. D. Bader, J. A. Borchers, G. P. Felcher, J. K. Furdyna, A. Hoffmann, J. B. Kortright, I. K. Schuller, T. C. Schulthess, S. K. Sinha, M. F. Toney, D. Weller, and S. Wolf, J. Magn. Magn. Mater. **271**, 103 (2004).

[85] A. Wiedenmann, Collection de la Société Française de la Neutronique **11**, 219 (2010), http://dx.doi.org/10.1051/sfn/201011013.

[86] A. Michels, C. Vecchini, O. Moze, K. Suzuki, P. K. Pranzas, J. Kohlbrecher, and J. Weissmüller, Phys. Rev. B **74**, 134407 (2006).

[87] A. Michels, C. Vecchini, O. Moze, K. Suzuki, J. M. Cadogan, P. K. Pranzas, and J. Weissmüller, Europhys. Lett. **72**, 249 (2005).

[88] A. Michels, S. Erokhin, D. Berkov, and N. Gorn, J. Magn. Magn. Mater. **350**, 55 (2014).

[89] J. S. Pedersen, Adv. Colloid Interface Sci. **70**, 171 (1997).

[90] D. J. Kinning and E. L. Thomas, Macromolecules **17**, 1712 (1984).

[91] A. Guinier and G. Fournet, *Small-Angle Scattering of X-rays* (Wiley, New York, 1955).

[92] G. Porod, in *Small Angle X-ray Scattering*, edited by O. Glatter and O. Kratky (Academic Press, London, 1982) pp. 17–51.

[93] L. A. Feigin and D. I. Svergun, *Structure Analysis by Small-Angle X-Ray and Neutron Scattering* (Plenum Press, New York, 1987).

[94] A. Michels, R. N. Viswanath, J. G. Barker, R. Birringer, and J. Weissmüller, Phys. Rev. Lett. **91**, 267204 (2003).

[95] J. Weissmüller, A. Michels, D. Michels, A. Wiedenmann, C. E. Krill III, H. M. Sauer, and R. Birringer, Phys. Rev. B **69**, 054402 (2004).

[96] A. Michels, Phys. Rev. B **82**, 024433 (2010).

[97] S. Erokhin, D. Berkov, N. Gorn, and A. Michels, Phys. Rev. B **85**, 024410 (2012).

[98] J. Šaroun, J. Appl. Cryst. **33**, 824 (2000).

[99] G. N. Watson, *A treatise on the theory of Bessel functions*, 2nd ed. (Cambridge University Press, Cambridge, 1966).

[100] J.-P. Bick, D. Honecker, F. Döbrich, K. Suzuki, E. P. Gilbert, H. Frielinghaus, J. Kohlbrecher, J. Gavilano, E. M. Forgan, R. Schweins, P. Lindner, R. Birringer, and A. Michels, Appl. Phys. Lett. **102**, 022415 (2013).

[101] L. Zhou, M. Miller, P. Lu, L. Ke, R. Skomski, H. Dillon, Q. Xing, A. Palasyuk, M. McCartney, D. Smith, S. Constantinides, R. McCallum, I. Anderson, V. Antropov, and M. Kramer, Acta Mater. **74**, 224 (2014).

[102] E. A. Périgo, E. P. Gilbert, K. L. Metlov, and A. Michels, New. J. Phys. **16**, 123031 (2014).

[103] O. Glatter and O. Kratky (editors), *Small Angle X-ray Scattering* (Academic Press, London, 1982).

[104] A. Michels and J.-P. Bick, J. Appl. Crystallogr. **46**, 788 (2013).

[105] W. H. Press, S. A. Teukolsky, W. T. Vetterling, and B. P. Flannery, *Numerical Recipes in C* (Cambridge University Press, Cambridge, 2002).

[106] A. Michels, D. Mettus, D. Honecker, and K. Metlov, Physical Review B **94**, 054424 (2016).

[107] S. V. Maleev, V. G. Bar'yakhtar, and R. A. Suris, Sov. Phys. Solid State **4**, 2533 (1963).

[108] M. Blume, Phys. Rev. **130**, 1670 (1963).

[109] J. Kindervater, W. Häußler, M. Janoschek, C. Pfleiderer, P. Böni, and M. Garst, Phys. Rev. B **89**, 180408 (2014).

[110] S. V. Grigoriev, A. S. Sukhanov, E. V. Altynbaev, S.-A. Siegfried, A. Heinemann, P. Kizhe, and M. S. V., Phys. Rev. B **92**, 22015 (2015).

[111] A. Fedorov, V.I. andGukasov, V. Kozlov, S. Maleyev, V. Plakhty, and I. Zobkalo, Phys. Lett. A , 372 (1997).

[112] A. Michels, R. N. Viswanath, and J. Weissmüller, Europhys. Lett. **64**, 43 (2003).

[113] S. V. Grigoriev, Y. O. Chetverikov, D. Lott, and A. Schreyer, Phys. Rev. Lett. **100**, 197203 (2008).

[114] V. V. Tarnavich, D. Lott, S. Mattauch, A. Oleshkevych, V. Kapaklis, and S. V. Grigoriev, Phys. Rev. B **89**, 054406 (2014).

[115] D. Michels, C. E. Krill III, and R. Birringer, J. Magn. Magn. Mater. **250**, 203 (2002).

[116] F. Döbrich, J. Kohlbrecher, M. Sharp, H. Eckerlebe, R. Birringer, and A. Michels, Phys. Rev. B **85**, 094411 (2012).

[117] S. Foner, Rev. Sci. Instrum. **30**, 548 (1959).

[118] C. J. Glinka, J. G. Barker, B. Hammouda, S. Krueger, J. J. Moyer, and W. J. Orts, J. Appl. Cryst. **31**, 430 (1998).

[119] C. J. Glinka, J. M. Rowe, and J. G. LaRock, J. Appl. Cryst. **19**, 427 (1986).

[120] S.-M. Choi, NCNR Summer School (2000).

[121] C. Dewhurst, Institut Laue Langevin, France (2015).

[122] S. R. Kline, J.Appl.Cryst. **39**, 895–900 (2006).

[123] V. Pipich, "Qtikws," .

[124] C. D. Dewhurst, I. Grillo, D. Honecker, M. Bonnaud, M. Jacques, C. Amrouni, A. Perillo-Marcone, G. Manzin, and R. Cubitt, J. Appl. Cryst. **49**, 1 (2016).

[125] J. Kohlbrecher and W. Wagner, J. Appl. Cryst. **33**, 804 (2000).

[126] O. Glatter, in *Small-angle X-ray Scattering*, edited by O. Glatter and O. Kratky (Academic Press, London, 1982) pp. 119–196.

[127] Q. A. Pankhurst, L. Fernández Barquín, J. D. Wicks, R. L. McGreevy, and M. R. J. Gibbs, J. Phys.: Condens. Matter **9**, L375 (1997).

[128] R. S. Turtelli, D. Triyono, R. Grössinger, H. Michor, J. H. Espina, J. P. Sinnecker, H. Sassik, J. Eckert, G. Kumar, Z. G. Sun, and G. J. Fan, Phys. Rev. B **66**, 054441 (2002).

[129] A. Bracchi, K. Samwer, P. Schaaf, J. F. Löffler, and S. Schneider, Mater. Sci. Eng. A **375-377**, 1027 (2004).

[130] Y. Suzuki, M. Awano, N. Kondo, and T. Ohji, J. Am. Ceram. Soc. **83**, 1113 (2000).

[131] É. A. Périgo, I. Titov, R. Weber, D. Mettus, I. Peral, O. Vallcorba, D. Honecker, A. Feoktystov, and A. Michels, Mater. Res. Express **5**, 036110 (2018).

[132] A. Michels, J.-P. Bick, R. Birringer, A. Ferdinand, J. Baller, R. Sanctuary, S. Philippi, D. Lott, S. Balog, E. Rotenberg, G. Kaindl, and K. M. Döbrich, Phys. Rev. B **83**, 224415 (2011).

[133] J. J. Rhyne and A. E. Clark, J. Appl. Phys. **38**, 1379 (1967).

[134] E. Jericha, G. Badurek, and C. Gösselsberger, Physics Procedia **42**, 58 (2013).

[135] M. Yano, K. Ono, M. Harada, A. Manabe, T. Shoji, A. Kato, and J. Kohlbrecher, J. Appl. Phys. **115**, 17A730 (2014).

[136] E. A. Périgo, E. P. Gilbert, and A. Michels, Acta Mater. **87**, 142 (2015).

[137] K. Saito, T. Ueno, M. Yano, M. Harada, T. Shoji, N. Sakuma, A. Manabe, A. Kato, U. Keiderling, and K. Ono, J. Appl. Phys. **117**, 17B302 (2015).